UC Santa Barbara
UC Santa Barbara Electronic Theses and Dissertations

Title
Micro-LEDs with MOCVD-grown tunnel junctions and properties of efficient InGaN red Micro-LEDs

Permalink
https://escholarship.org/uc/item/4h0689jw

Author
LI, PANPAN

Publication Date
2022

Peer reviewed|Thesis/dissertation

eScholarship.org Powered by the California Digital Library
University of California

UNIVERSITY OF CALIFORNIA

Santa Barbara

Micro-LEDs with MOCVD-grown tunnel junctions and properties of efficient InGaN red Micro-LEDs

A dissertation submitted in partial satisfaction of the

requirements for the degree

Doctor of Philosophy in Materials

by

Panpan Li

Committee in charge:

Professor Steven P. DenBaars, Chair

Professor Shuji Nakamura

Professor James S. Speck

Professor Mike Gordon

September 2022

The dissertation of Panpan Li is approved.

Mike Gordon

James S. Speck

Shuji Nakamura

Steven P. DenBaars, Committee Chair

September 2022

ACKNOWLEDGEMENTS

Prof. Denbaars, it has been such an honor to work with you and learn from you and thank you for the precious opportunity and the enduring support of my work. You always encourage me to try new things, give me lots very useful ideas. Thanks for the many discussions in your office on tunnel junction and cascaded LED. Thank you for giving me precious chance to work on Micro-LEDs and long wavelength LEDs and long wavelength laser. In the lab, we have the world-class MOCVD and LED facilities. The great conditions made all of this work possible. Prof. Nakamura, thank you for your support and encouragement of my work. Also, thanks for your great ideas, they inspired me a lot. Thanks for your advice on tunnel junction-related questions and giving me the opportunity to participate in long wavelength LED research projects. Prof. Speck, thank you for your support and teaching me everything I know about x-ray diffraction, and for the discussions and the kind comments on tunnel junction, and thank you for all the excellent edits on my manuscripts. Prof. Gordon, thank you for your advice on blue peak in red LEDs, and for giving me the suggestions to test blue peak using CL. Thank you for the professional measuring systems in your lab such as temperature dependent PL and on wafer EQE test system. They are very useful for my research project.

Also, I really appreciate that I can have the wonderful opportunity to work with and learn from the talented scientists in this group. M. Iza and H. Li, thank you for teaching me how to use MOCVD and giving me a lot of growth suggestions. Haojun and Matthew, thank you for training me on all the techniques in the cleanroom. I would also like to thank Tal Margalith and Stacia Keller for their mentorship of Micro-LEDs and the encyclopedic knowledge of MOCVD. All my SSLEEC colleagues past and present, thank you for showing me by example how to be a good scientist and I learn a lot from you. I would also like to acknowledge the

support of all the staff in the Materials. Yukina, Tara, Emi, Fukiko and Alexandria, Thank you for all the great help about the massive paperwork.

I would also like to acknowledge all my friends Yifan, xinhong, Chongxin, Yunxuan, Yujie, Tanay, Stephen, Takeki, Li Wu, Yirong, Wei Yang, Ning Yang, Mohan, Yuan Guo etc… Your support and help are super important to me.

Last but not least, I would like to thank my loving family. This dissertation is dedicated to my husband and my daughter. My husband, you are the most supportive person. You encourage me to pursuit my dream and take lots of responsibility of our family. You have been incredibly encouraging and supportive throughout my time at UCSB. Thanks to my daughter. Parents and children are the best gift to each other. Thank you for letting me go through the incredible childhood again. Because of you, I can keep curiosity and passion at everything in the world. My mum, my dad, my mother-in-law and my father-in-law, thank you for teaching me lots of the wisdom of life.

ABSTRACT

Micro-LEDs with MOCVD-grown tunnel junctions and properties of efficient InGaN red Micro-LEDs

Panpan Li

Micro-size light-emitting diodes (μLEDs) have attracted huge attentions as the next-generation display technology for the wide applications, such as wearable watches, virtual/augmented reality, micro-projectors, and ultra-large televisions. InGaN LEDs or laser diodes with epitaxial tunnel junctions (TJs) are attractive due to several advantages, such as simple fabrication process, higher efficiency, and lower efficiency droop by improved current spreading, less loss. In the first part, high performance InGaN μLEDs with MOCVD-grown TJs were successfully demonstrated using selective area growth (SAG) and p^+GaN/InGaN/n^+GaN structure. SAG apertures provide paths for the out diffusion of H^+ atoms, which passivated Mg atoms in the p-type GaN during the overgrowth of TJs. The forward voltage (V_f) in the SAG TJ μLEDs is independent on the device sizes, suggesting that the H^+ atoms are effectively removed through the holes on top of the p-GaN surface. The V_f @ 20 A/cm^2 in the TJ μLEDs utilizing SAG is significantly reduced to 3.24 V. Moreover, the output power of TJ μLEDs with SAG is ~10% higher than the common μLEDs with indium tin oxide (ITO) contact. The InGaN TJs μLEDs show a significant reduction of V_f by ~0.6 V compared to the common n-GaN TJs μLEDs. The external quantum efficiency (EQE) of the packaged TJ μLEDs was improved by 6% compared to the common μLEDs with common ITO contact. These demonstrations solve the key challenges of MOCVD-grown TJs. Then,

we present fully MOCVD-grown InGaN cascaded μLEDs with independent junction control. The cascaded μLEDs consisted of a blue emitting diode, a TJ, and a green emitting diode. We can control the injection of carriers into blue, green, and blue/green junctions in the same device independently.

Finally, we present the state-of-the-art InGaN-based red μLEDs, which have become research focus now in the whole nitride community. The common AlInGaP red μLEDs show a dramatical reduction of the EQE with decreasing the devices area and poor thermal property. We demonstrated several remarkable InGaN device performances with emission wavelength greater than 600 nm. First, we reported that the EQE of InGaN red μLEDs has less influence from the size effect due to the lower surface recombination velocity, compared to conventional AlInGaP red μLEDs. Moreover, we investigated the temperature-dependent electrical luminesce characteristics of InGaN red μLEDs, and we found that InGaN red μLEDs have superior device performances even operating at high temperature up to 400 K. We realized 5×5 μm^2 InGaN devices with a peak EQE value of 2.6%. We also present red InGaN 60×60 μm^2 μLED with SAG TJ contact, which show a peak EQE of 4.5% at 623 nm. These values about InGaN red μLEDs are one of the best reported among the literatures. A 568 nm stimulated optically lasing from our InGaN red MQWs was also achieved.

Table of contents

Introduction....1

1.1 GaN basics....1

1.2 GaN-based LEDs....3

1.3 GaN-based micro-LEDs....5

1.4 Development of InGaN-based red micro-LEDs....7

References....11

2. GaN-based Tunnel junctions grown by MOCVD....14

2.1 Tunnel Junction LEDs: Physics and Challenges....15

2.2 Motivation of GaN Tunnel Junction....16

2.2.1 Improve hole injection in GaN-based LEDs....16

2.2.2 multi-junctions devices....18

2.2.3 Solution to efficiency droop using carrier regeneration in tunnel junctions....18

2.3 Review of the development of Tunnel junction....19

2.3.1 Development of Tunnel Junction grown by MBE....19

2.3.2 Development of Tunnel Junction grown by MOCVD....21

2.4 Tunnel junctions using selective area growth by metalorganic chemical vapor deposition....22

2.5 MOCVD grown n^+GaN/n-InGaN/p^+GaN tunnel junctions....28

2.6 MOCVD grown n+GaN/n-InGaN/p+GaN tunnel junctions combined SAG technology....35

References....45

3. Cascaded Blue LED and Green LEDs....49

3.1. Challenges of Cascaded LEDs....49

3.2 Cascaded blue and green micro-LEDs with independent junction control 50

3.3 Fully transparent cascaded blue and green micro-light-emitting diodes 55

References....62

4. InGaN based red micro-LEDs 65

4.1 Size-independent peak EQE of InGaN red μLEDs 65

4.2 Robust temperature property of InGaN red μLEDs....74

4.3 Ultra-small 5×5 μm2 InGaN red micro-light-emitting diodes 82

4.4 Red InGaN micro-light-emitting diodes (>620 nm) with a peak external quantum efficiency of 4.5% using an epitaxial tunnel junction contact....88

References： 96

5. Demonstration of Yellow (568 nm) Stimulated Emission from Optically Pumped InGaN/GaN Multi-Quantum Wells 99

References: 107

Appendix....110

Lateral μLED of different sizes - Process Flow 110

Introduction

1.1 GaN basics

Gallium nitride (GaN) is a binary III/V direct bandgap compound semiconductor. The common GaN has a wurtzite crystal structure, as shown in Fig. 1.1. The energy band gap is 3.4 eV. As show in Fig. 1.2, the band gap of InGaN or AlGaN alloy compound semiconductor covers the emission wavelength from ultra-violet to all visible range, making them very attractive for the optoelectronic, such as light-emitting diodes (LEDs) and laser diodes (LDs). By incorporating indium as InGaN material, the bandgap can be tuned from 0.9 eV to 3.4 eV, which covers the full range of visible light. Meanwhile, by incorporating Aluminum as InGaN material, the bandgap can be tuned from 3.4 eV to 6.2 eV, which offers the emission wavelength at ultra-violet range. [1]

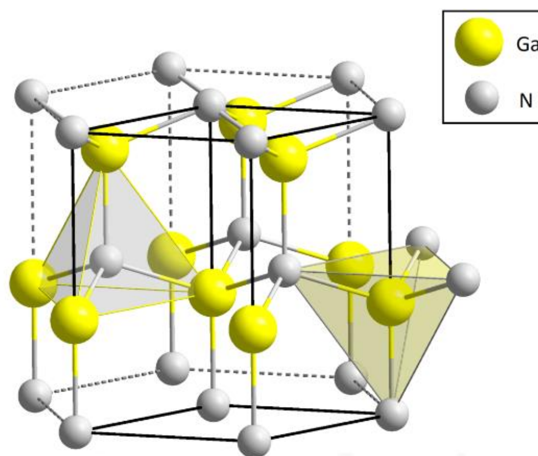

Fig 1.1 Crystal structure of wurtzite GaN.

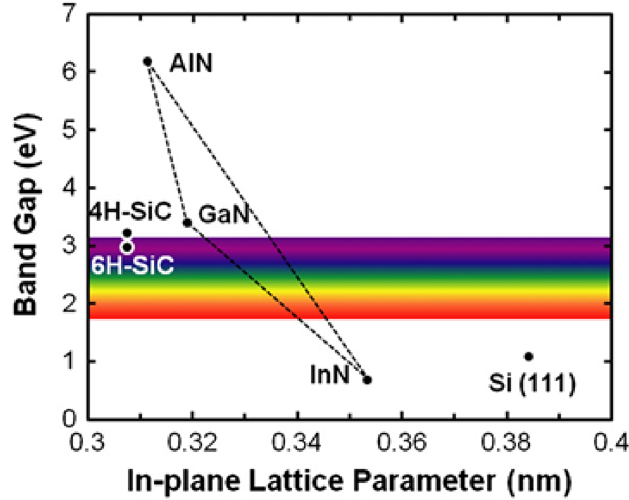

Fig 1.2 Band gap over lattice constant for AlN, GaN, and InN and its related alloy.

Another important application of GaN material is for the high-power and high-frequency devices. A comparison of commonly used semiconductor materials for high-power and high-frequency devices, such as Si, GaN and SiC is listed in Table I. GaN material show a much higher electron mobility of ~2000 $cm^2/V/s$ by forming a two-dimensional electron gas (2DEG) at the AlGaN/GaN interface, followed by a much higher bandgap as compared to the Si. In Khan et al. reported the first observation of enhanced electron mobility in AlGaN/GaN heterojunctions, resulting in the high electron mobility transistor in 1993. [2, 3] This paves the way to high- performance of high-power and high-frequency devices with a high breaking down voltage and a low on-resistance using GaN material.

Table I, Comparison of Si, GaN, 4H-SiC compound semiconductor properties

	Si	**GaN**	**4H-SiC**
Band Gap Eg(eV)	1.1	3.39	3.26
Breakdown Electric Field (MV/cm)	0.3	3.3	3.0
Electron mobility ($cm^2/V/s$)	1350	2000	700
Releative dielectric constant	11.8	9.0	10

1.2 GaN-based LEDs.

The following Fig. 1.3 shows the development of LEDs. [4] Red and green LEDs were first commercialized in 1962 and 1974 using GaAsP and GaP, respectively. But there is no report about blue LEDs since the GaN material crystal quality is very poor and there is lack of bulk GaN substrate in the nature. In 1985, H. Amano et al. from Professor Akasaki group in Nagoya University firstly achieved mirror-like GaN thin film using metal organic chemical vapor deposition (MOCVD) by introducing 2-two step growth, that is growing a low temperature AlN nucleation layer before the growth of high temperature GaN material at 1020 ˚C. [5] P-type GaN was obtained using low-energy electron beam irradiation (LEEBI) treatment. [6] But the mechanism remains unclear. Dr. Nakamura from Nichia Corporation made the breakthrough by growing GaN material using a two-flow MOCVD. [7] A low temperature GaN thin film was achieved by using a low temperature GaN nucleation. P-type GaN was realized by using a simple thermal annealing, which is using by all the LEDs manufacturer now. [8] Mg passivated by hydrogen was identified as the cause for compensation effect in the p-type GaN, which can be easily broken by activating in a high temperature over 600 ˚C. Double-heterostructure-type/quantum wells (QWs) structure InGaN blue LEDs was firstly demonstrated and successfully commercialized in 1993 and first InGaN violet LDs was reported in 1996 by Dr. Nakamura. [9-11]

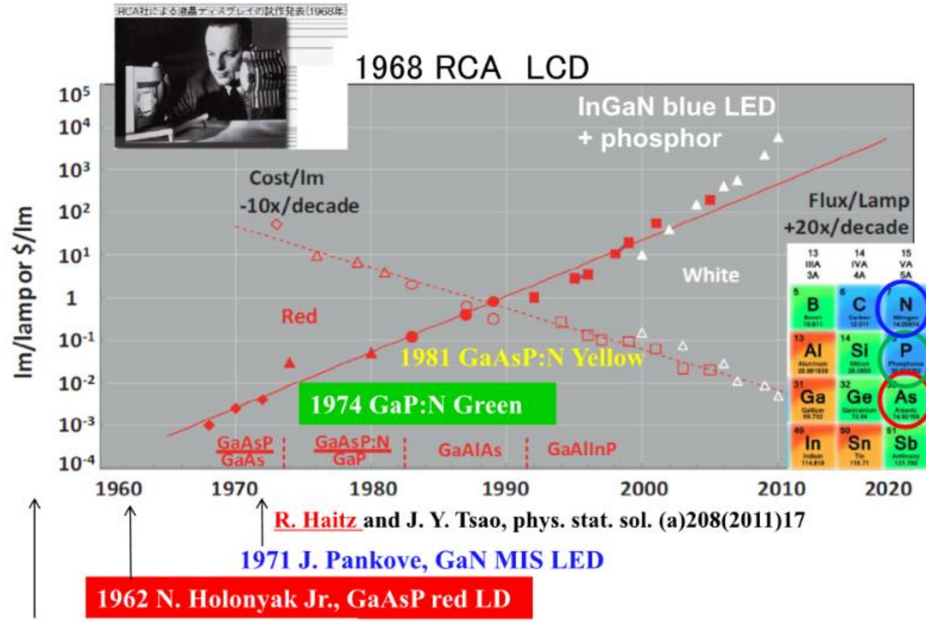

Fig 1.3 Development of LEDs (Reproduced with permission from ref. [4]).

After the decades of development, GaN-based LEDs has shown great success as the solid-state lighting source, which have a higher energy efficiency, longer lift time, and better reliability. GaN-based blue LEDs have been widely used in the back lighting, general lighting, auto headlight, traffic light and so on. The market value of GaN-based white LEDs by combining with yellow phosphor has been larger than 100 billion dollars per year. The external quantum efficiency (EQE) of InGaN blue LEDs has reached as high as 72% and the EQE of InGaN green LEDs (>520 nm) has larger than 50%. [12, 13]

The epitaxy structure of GaN-based LEDs is typically consisted with a n-type GaN (Si-doped), InGaN/GaN superlattices (SLs), InGaN/GaN multiple quantum wells (MQWs), p-type AlGaN electron blocking layer (EBL), and p-type GaN (Mg-doped). The EQE of GaN-based LEDs show an efficiency droop as the injection current increases. Fig. 1.4 shows the carrier recombination in the InGaN LEDs. In the ABC model, the EQE can be expressed by $\mathrm{EQE}=\mathrm{LEE}\times Bn^2/(An + Bn^2 + Cn^3)$, where LEE is the light extraction efficiency, A is Shockley-

Read-Hall nonradiative recombination coefficient, B is radiative recombination coefficient, C is the Auger recombination coefficient, and n is the carrier density. [14] The defect-related Shockley -Read- Hall (SRH) recombination results in a nonradiative recombination (term An), which is caused by the high dislocation density in the InGaN QWs or any sidewall damage. Auger (term Cn^3) nonradiative recombination is pronounced in the InGaN LEDs, which has been experimentally evidenced by electro-emission spectroscopy (EES) measurements. Also, electron can be escaped out of the MQWs to the p-type GaN since the mobility and concentration of electron is much higher than the hole. Growing InGaN LEDs on semipolar or nonpolar oriented GaN is proposed to alleviate the efficiency droop, although the semipolar or nonpolar GaN substrate is much costly. Another challenge of InGaN LEDs is the "green gap" issue, which will be discussed in 1.4 section.

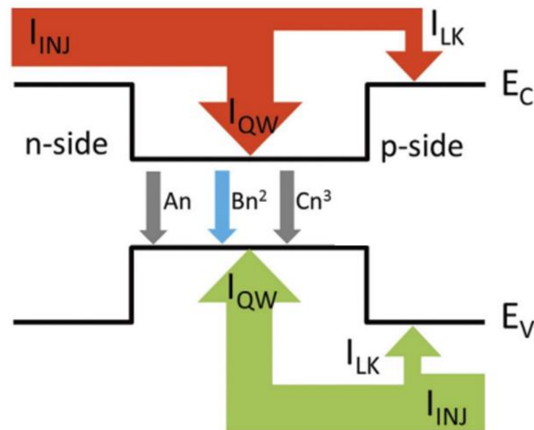

Fig 1.4 Carrier recombination schemes revealing the mechanisms of current droop effect in a GaN based LED [11].

1.3 GaN-based micro-LEDs.

Micro-size light-emitting diodes (μLEDs) are the LEDs size less than 100×100 μm^2, which were first reported in 2000 by the research group of H. Jiang and J. Lin of Texas

Tech University while they were at Kansas State University (Fig. 1.5). [15] Nowadays, μLEDs are attracting huge attention for the emissive display with a higher efficiency, longer operating lifetime and a higher pixel density compared to liquid crystal display and organic light-emitting diodes (LEDs). μLEDs. μLEDs are regarded as the next-generation display technology to meet the personalized demands of advanced applications, such as mobile phones, wearable watches, virtual reality (VR), augmented reality (AR), micro-projectors and ultrahigh-definition TVs and so on.

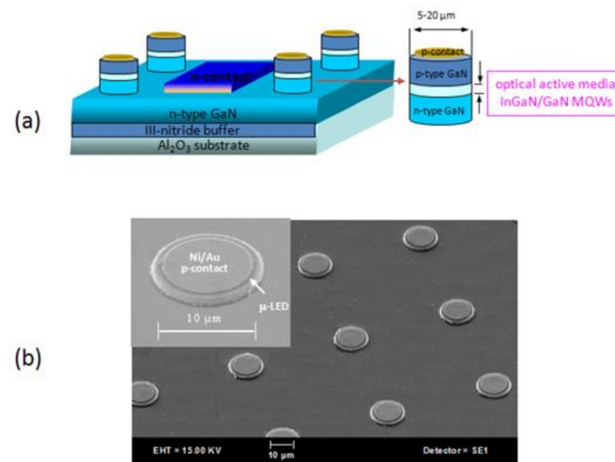

Fig 1.5 (a) Schematic layer structure diagram and (b) SEM image of InGaN/GaN quantum well micro-size LEDs (μLEDs) (after Ref. [15]).

But the EQE of μLEDs faces severe size effect, which decreases dramatically with reducing size to several micrometer scale. This is due to the SRH nonradiative recombination when the sidewall area to the device volume is very large. It is found that proper sidewall passivation by atom layer deposition (ALD) SiO_2, the EQE of ultra-small size GaN based blue μLEDs or AlInGaP red μLEDs can be significantly improved. R. Ley reported a higher EQE in 2 μm InGaN blue/green μLEDs than that 100 μm size μLEDs by chemical treatment and dielectric passivation. These results prove the importance of GaN-based μLEDs with ultra-small size, which can be implanted for the AR and VR application.

1.4 Development of InGaN-based red micro-LEDs.

For the RGB display, III-nitride materials are usually used for the blue and green LEDs and AlInGaP materials are employed for the red LEDs.[16] But red μLEDs have become an obstacle for the μLEDs display. On one hand, the EQE of AlInGaP-based red μLEDs faces severe size effect, which reduces dramatically by decreasing size to sub-micrometers scale, although AlInGaP LEDs with a regular size show a high EQE.[17-19] This is because that the surface recombination velocity of AlInGaP material is high (~10^5 cm/s), resulting in a high nonradiative recombination loss due to sidewall damage for very small size device.[6] Also, the thermal stability of AlInGaP red μLEDs is very poor.[20, 21] Lee *et al.* reported that the output power of 10-μm AlInGaP red μLEDs at 120 °C reduces dramatically to be less than 20% of the output power at room temperature.[20] Also, it is very challenging to assemble millions of InGaN blue/green μLEDs and AlInGaP red μLEDs with different materials system in one full-color display. The large difference in the operation voltage for AlInGaP red μLEDs (2.0~2.5 V) and InGaN blue/green μLEDs (>3.0 V) becomes problematic for the driven design.[22]

On the other hand, InGaN LEDs suffer from "green gap" challenge: that is the EQE of InGaN LEDs reduces dramatically as the emission wavelength goes into green or longer range (>520 nm).[23] The main causes for the low efficiency of the InGaN red μLEDs are the strong quantum-confinement Stark effect (QCSE) and the high defect density due to a low growth temperature of ~760 ˚C for the InGaN quantum wells (QWs) and a large lattice mismatch between InGaN QWs and GaN barriers. The EQE of InGaN green LEDs have been largely improved.[24~26] Development of high efficiency InGaN-based red μLEDs becomes research focus now due to several unique properties of InGaN materials. The first one is the

less significant size effect of EQE for the InGaN-based μLEDs by proper sidewall passivation and treatments.[27~28] The EQE of InGaN μLEDs can maintain a similar value even for the size down to 1 μm as compared to the 100 μm device. Also, the InGaN μLEDs exhibit a much robust thermal stability at a high operation temperature.[29] The employment of InGaN-based full color μLEDs display can largely simplify the driven design.[30] In the following section, we will discuss about the recent developments of InGaN-based LEDs/μLEDs using different technology.

In 2014, Hwang *et al.* from Toshiba reported regular size (0001) InGaN red LEDs grown on PSS. [31] A high Al composition $Al_{0.9}Ga_{0.1}N$ layer was inserted on top of InGaN red QWs, resulting in the uniform red emission from fluorescence images. From Fig. 3, the 460×460 μm^2 size InGaN red LEDs show an output power of 11 mW, an EQE of 2.9% and an emission wavelength of 629 nm at 20 mA. Another weak peak located at 430 nm was observed in the spectra, which is related to the phase-separated component in the InGaN red QWs.

In 2020, Iida *et al.* from KAUST reported InGaN red LEDs growing on PSS using 8-μm-thick nGaN underlying with a lower residual in-plane stress. The red LEDs show a peak emission wavelength of 633 nm, a light output power of 0.64 mW and an external quantum efficiency of 1.6% at 20 mA. [32] Meanwhile, they demonstrated 10×10 arrays of InGaN 17×17 μm^2 μLEDs as shown in Fig. 4. [33] The peak wavelength is blue shifted from 662 to 630 nm at 10 to 50 A/cm^2. The on-wafer EQE was 0.18% at 50 A/cm^2 and the output power density was 1.76 mW/mm^2.

In 2021, Li *et al.* from UCSB demonstrated a significant progress of InGaN red μLEDs on PSS. [27, 29, 30] The packaged 607 nm InGaN red μLEDs show a peak EQE of 2.4% to 2.6% as the size reduces from 100×100 μm^2 to 20×20 μm^2. The same team also demonstrates

InGaN red μLEDs with a peak EQE of 3.2% and a much robust thermal stability as compared to the common AlInGaP red μLEDs. Moreover, Li *et al.* from UCSB reported ultra-small 5×5 μm^2 InGaN amber μLEDs grown on PSS with a peak EQE greater than 2%. Since the AR and VR display demand μLEDs with a size smaller than 10×10 μm^2, the excellent optical and electrical performance of the 5×5 μm^2 InGaN amber μLEDs suggest the promising application for AR and VR micro-display using InGaN materials. The Light Tool simulation reveal that the light extraction efficiency (LEE) of 76% in the 5×5 μm^2 InGaN red μLEDs is higher than 64% in the 100×100 μm^2 μLEDs due to an enhanced light scatting from the sidewalls. But the EQE of 5×5 μm^2 InGaN μLEDs is lower than that of 100×100 μm^2 μLEDs (3.2%). Therefore, the impact of nonradiative recombination from the sidewalls damage can't be neglected in such small μLEDs. New less damage sidewalls etching process is believed to be a good approach improve the efficiency of ultra-small InGaN μLEDs.

In 2019, Jiang *et al.* from Nanchang University proposed "3D pn junction" from V-pits injection. [24] The V-pits can screen the dislocations and increase the hole injection into active region. In 2020, the same team reported efficient InGaN-based red LEDs grown on Si (111) substrates.[34] The voids of V-pits reduce compressive strain and benefit for the growth of high In composition InGaN QWs. The hybrid MQWs design with yellow QWs and orange QWs enables a high peak wall-plug efficiency (WPE) of 24% at 0.8 A/cm^2 with an emission wavelength of 608 nm. 621 nm InGaN red LEDs with a peak WPE of 16.8% was achieved with a very low forward voltage of 1.96 V at 0.8 A/cm^2. Theorical simulation of "3D V-pits injection" has been investigated.[35]

Even *et al*. from LETI and Soitec observed a significant enhancement of indium incorporation in full InGaN heterostructure grown on semi-relaxed InGaN pseudo-substrate (InGaNOS) due to the composition pulling effect.[36] The InGaNOS was developed by Soitec based on its Smart CutTM technology and offers a thin relaxed InGaN seed layer. The photoluminescent (PL) was red shifted by ~50 nm by growing InGaN QWs on InGaNOS compared to the common GaN template. In 2021, Dussaigne *et al.* from LETI and Soitec reported InGaN red μLEDs grown on InGaNOS with a lattice parameter of 3.210 Å. The 10 μm diameter circular 625 nm InGaN red μLEDs show an EQE of 0.14% at 8 A/cm^2, despite of the LEE estimated below 4%. Also, White *et al.* from UCSB and Soitec have greatly improved the EQE of 80×80 μm^2 609 nm InGaN μLEDs on InGaNOS to 0.83% by reducing the defect density in the InGaN/GaN buffer layer and optimizing the p-type structure (Fig. 7).[37] Noted that the growth temperature for red QWs on InGaNOS is much higher than the typical red QWs grown on GaN template (close to green InGaN QWs growth temperature).

Pasayat *et al*. from UCSB developed compliant GaN on porous GaN pseudo-substrates (PSs) for strain relaxed InGaN layer.[38] A 10×10 μm^2 pattern with a 100 nm compliant GaN cap layer was grown on top of the porous GaN layer. Doping selective electrochemical (EC) etching was used to form the nano-porous structure. The 440 nm thick InGaN layer with 3~4% indium composition grown on the PSs shows a 56% strain relaxation from x-ray diffraction reciprocal space map (RSM). The peak wavelength was red shifted by 56 nm. The 632 nm InGaN red μLEDs (6×6 μm^2) show a peak on-wafer EQE of 0.2%. The output power density was 2.1 mW/mm^2 at 100 A/cm^2. But such technology involves complicated fabrication process and materials overgrowth. The thermal conductively and reliability remains poor for the nano-porous template.

Chan *et al.* from UCSB developed a novel technology using in-situ InGaN decomposition layer (DL) to realize highly strain relaxed InGaN PSs.[39] A 3 nm thick very high indium composition InGaN DL and a 100 nm deposition stop layer were grown, and then a thermal annealing at 1000 °C was carried out. Voids were formed in the DL. The 200 nm $In_{0.04}Ga_{0.96}N$ grown on top were highly relaxed with an 85% biaxial relaxation confirmed by XRD RSM. The PL wavelength was red shifted by 75 nm from 440 nm to 515 nm. Moreover, the same team reported 100% fully strain relaxed $In_{0.04}Ga_{0.96}N$ layer. Red emission was obtained by growing the QWs at a very high temperature of 870 °C. [40] The 633 nm red LEDs show a peak on-wafer EQE of 0.05%. The operation forward voltage is as low as 2.25 V at 25 A/cm^2. This technology is much more practical without introducing any extra complicated process or overgrowth as compared to InGaNOS and nano-porous template. The surface of relaxed InGaN buffer layer is very rough from atomic force micrograph with a lot of pits. Further epitaxy optimization is needed to minimize the surface roughness and reduce the defect density.

References

1. S. Nagahama, Y. Sugimoto, T. Kozaki, and T. Mukai, Proc. SPIE, 5738, 57 (2005).
2. M. A. Khan, J. M. V. Hove, J. N. Kuznia, and D. T. Olson, App. Phys. Lett., 58, pp. 2408 (1991).
3. M. A. Khan, A. Bhattarai, J. N. Kuznia, and D. T. Olson, AppL. Phys. Lett., 63, 1214 (1993).
4. H. Amano, Progress in Crystal Growth and Characterization of Materials, 62, 126(2016)
5. H. Amano, N. Sawaki, I. Akasaki, Y. Toyoda, Appl. Phys. Lett. 48, 353 (1986).
6. H. Amano, M. Kito, K. Hiramatsu, and I. Akasaki, Jpn. J. Appl. Phys. 28, L2112(1989).
7. S. Nakamura, Jpn. J. Appl. Phys., 30, L1705(1991).

8. S. Nakamura, T. Mukai, M. Senoh, and N. Iwasa, Jpn. J. Appl. Phys. 31, L139(1992).
9. S. Nakamura, M. Senoh, T. Mukai Appl. Phys. Lett. 62, 2390(1993).
10. S. Nakamura, M. Senoh N. Iwasa, SI. Nagahama, Appl. Phys. Lett. 67, 1868(1995).
11. S. Nakamura, M. Senoh, SI.Nagahama, N. Iwasa, T, Yamada, T. Matsushita, Y. Sugimoto H. Kiyoku, Appl. Phys. Lett. 69,4056(1996).
12. B. P. Yonkee, E. C. Young, S. P. DenBaars, S. Nakamura, and J. S. Speck, Appl. Phys. Lett. 109, 191104 (2016)
13. P. Li, Y. Zhao, H. Li, J. Che, Z.Zhang, Z.Li, Y. Zhang, L. Wang, Y. Xiao, G. Wang, Optics Express 26, 33108 (2018).
14. S. Karpov, Optical and Quantum Electronics. 47,1293(2015).
15. S.X. Jin, J.Li, J.Z.Li, J.Y. Lin H. X.Jiang, Appl. Phys. Lett. 76, 631(2000).
16. J. T. Oh, S. Y. Lee, Y. T. Moon, J. H. Moon, S. Park, K. Y. Hong, K. Y. Song, C. Oh, J. I. Shim, H. H. Jeong, J. O. Song, H. Amano, and T.-Y. Seong, Opt. Express 26, 11194(2018).
17. M. S. Wong, J. A. Kearns, C. Lee, J. M. Smith, C. Lynsky, G. Lheureux, H. Choi, J. Kim, C. Kim, S. Nakamura, J. S. Speck, and S. P. DenBaars, Opt. Express 28, 5787(2020).
18. Y.-Y. Li, F.-Z. Lin, K.-L. Chi, S.-Y. Weng, G.-Y. Lee, H.-C. Kuo, C.-C. Lin, IEEE Photonics J. 14, 7007907(2022).
19. D-H Lee, S-Y Lee, J-I Shim, T-Y. Seong, and H. Amano, ECS J. Solid State Sci. Technol. 10, 095001(2021).
20. C.-H. Oh, J.-I. Shim, D.-S. Shin, Jpn. J. Appl. Phys. 58, SCCC08(2019).
21. J. J. Wierer, Jr. and N. Tansu, Laser Photonics Rev. 13, 1900141(2019).
22. H. Li, P. Li, J. Kang, Z. Li, Y. Zhang, Z. Li, J. Li, X. Yi, J. Li, G. Wang, Appl. Phys. Express 6, 052102(2013).
23. A. I. Alhassan, R. M. Farrell, B. Saifaddin, A. Mughal, F. Wu, S. P. DenBaars, S. Nakamura, and J. S. Speck, Opt. Express, 24, 17868(2016).
24. F. Jiang, J. Zhang, L. Xu, J. Ding, G. Wang, X. Wu, X. Wang, C. Mo, Z. Quan, X. Guo, C. Zheng, S. Pan, and J. Liu, Photonics Res., 7, 144(2019).
25. P. Li, H. Li, M.S. Wong, P. Chan, Y. Yang, H. Zhang, M. Iza, J.S. Speck, S. Nakamura, and S. P. DenBaars, Crystals, 12, 541(2022).
26. J. M. Smith, R. T. Ley, M. S. Wong, Y. Baek, J. Kang, C. H. Kim, M. J. Gordon, S.

Nakamura, J. S. Speck, and S. P. DenBaars, Appl. Phys. Lett., 116, 071102(2020).

27. P. Li, H. Li, H. Zhang, C. Lynsky, M. Iza, J. S. Speck, S. Nakamura, and S. P. DenBaars, Appl. Phys. Lett. 119, 081102(2021).
28. M. Sheen, Y.Ko, D. Kim, J. Kim, J.-H. Byun, Y. Choi, J. Ha, K. Y. Yeon, D. Kim, J. Jung, J. Choi, R. Kim, J. Yoo1, I. Kim, C. Joo1, N. Hong, J. Lee, Sang H. Jeon, S. Ho Oh, J. Lee, N. Ahn & C. Lee, Nature 608, 56(2022).
29. P. Li, A. David, H. Li, H. Zhang, C. Lynsky, Y. Yang, M. Iza, J.S. Speck, S. Nakamura, and S. P. DenBaars, Appl. Phys. Lett. 119, 231101(2021).
30. P. Li, H. Li, Y. Yao, H. Zhang, C. Lynsky, K. S. Qwah, J. S. Speck, S. Nakamura, and S. P. DenBaars, Appl. Phys. Lett. 118, 261104(2021).
31. J.-I. Hwang, R. Hashimoto, S. Saito, and S. Nunoue, Appl. Phys. Express 7, 071003 (2014).
32. Daisuke Iida, Z. Zhuang, P. Kirilenko, M. Velazquez-Rizo, M. A. Najmi, and K. Ohkawa, Appl. Phys. Lett. 116, 162101 (2020).
33. Z. Zhuang, D. Iida, M. Velazquez-Rizo, and K. Ohkawa, Photonics Research, 1796 (2021).
34. F. Jiang, J. Zhang, L. Xu, J. Ding, G. Wang, X. Wu, X. Wang, C. Mo, Z. Quan, X. Guo, C. Zheng, S. Pan, and J. Liu, Photonics Research 7, 144 (2019).
35. G. Lheureux, C. Lynsky, Y.-R. Wu, J. S. Speck, and C. Weisbuch, J. Appl. Phys. 128, 235703 (2020).
36. A. Even, G. Laval, O. Ledoux, P. Ferret, D. Sotta, E. Guiot, F. Levy, I. C. Robin, and A. Dussaigne, Appl. Phys. Lett. 110, 262103 (2017).
37. R.C White, H. Li, M. Khoury, C. Lynsky, M. Iza, S. Keller, D. Sotta, S. Nakamura, and S. P. DenBaars, Crystals 11, 1364(2021).
38. S. S Pasayat, C. Gupta, M. S Wong, R. Ley, M. J Gordon, S. P DenBaars, S. Nakamura, S. Keller, U. K Mishra, Appl. Phys. Express 14, 011004 (2021).
39. P. Chan, V. Rienzi, N. Lim, H.M. Chang, M. Gordon, S.P. DenBaars, S. Nakamura, Appl. Phys. Express 14, 101002(2021).
40. P. Chan, S.P. DenBaars, S. Nakamura, Appl. Phys. Lett. 119, 131106(2021).

2. GaN-based Tunnel junctions grown by MOCVD

Since the first tunnel junction (TJ) was demonstrated in 1958 by Esaki in a highly doped Ge p-n junction, [1] there has been of great interest to develop GaN-based optoelectronic devices such as light-emitting diodes (LEDs) and laser diodes (LDs) with TJs due to several advantages. [2] By operating the TJs at a reverse biased condition, an electron in the valence band of p-GaN tunnels into the conduction band of n-GaN, leading to a hole injection into p-GaN. [3-4] TJs offer an enhanced current injection and current spreading as it is much easier to form a good ohmic contact to n-GaN with a lower resistivity than p-GaN. [5] TJs also provide a reduced light absorption than the semi-transparent Ni/Au metal contacts or transparent indium tin oxide (ITO) contact, and a less loss as cladding layer for LDs. [6] Moreover, TJs can not only enable the realization of cascaded LEDs, [7-8] but also can connect multiple devices in a tandem structure such as multi-junctions solar cells, [9-11] and multi-junction lasers. [12] Furthermore, GaN-based tunnel junctions are expected to be used as a superior current confinement in GaN-based vertical-cavity surface-emitting lasers. [13-20] Efficient tunnel junctions (TJs) for GaN-based optoelectronic and electronic devices have been attractive due to the advantages of reduced absorption and loss and improved current spreading. [1-2] More importantly, cascaded LEDs could be realized through connecting by TJs, which could be a good approach to solve the efficiency droop and monolithically integrate red/green/blue LEDs in one device. [4-8]

In this chapter, we review the physics and development of tunnel junctions and the tunnel junctions we grow by MOCVD. This section will be into four different parts: tunnel junction LEDs physics and challenges, review of the development of tunnel junction, tunnel junctions

using selective area growth by metalorganic chemical vapor deposition and MOCVD grown n+GaN/n-InGaN/p+GaN tunnel junctions.

2.1 Tunnel Junction LEDs: Physics and Challenges

To obtain efficient TJs, the doping profile of donors and acceptors should be sharp enough. Therefore, the valence band in p-doped layer and the conduction band in n-doped layer are very close, resulting in quantum mechanical tunneling shown as Figure 1. The depletion width (w) of p-n diodes needs to reduce for a high tunneling probability. Under a revise bias voltage (V), the valence band in p-doped layer will move up. Meanwhile, the conduction band in n-doped layer will move down, leading to the overlap of energy level between the electrons in p-doped layer and the holes in n-doped layer. The depletion width (w) of p-n diodes needs to reduce for a high tunneling probability. The w can be obtained by $w = \sqrt{\frac{2\varepsilon(N_A+N_D)}{qN_AN_D}(V_{bi}-V)}$ (1), where ε is the permittivity of free space, N_A and N_D are the donor and acceptor concentrations, respectively, q is the electron charge, and V_{bi} is the built-in potential. V_{bi} can be expressed by $V_{bi} = \frac{k_BT}{q} In(\frac{N_AN_D}{N_CN_V \cdot \exp\left(-\frac{E_g}{kT}\right)})$ (2), where k_B is the Boltzmann constant, *T* is the temperature, N_C and N_V are the effective density of states of the conduction and valence bands, respectively, and Eg is the bandgap energy. [21] Thus, increasing the doping concentration or inserting low bandgap InGaN layer could reduce w and then increase the tunneling probability. To date, hybrid structure with metalorganic chemical vapor deposition (MOCVD)-grown LEDs and molecular beam epitaxy (MBE)-grown tunnel junctions is the common approach, which shows a low forward voltage (V_f) with a lowest penalty of 0.2~0.3 V as compared to the LEDs with common indium tin oxide (ITO) contacts. [1-2] However, the output and scalability of MBE are limited. Full MOCVD-grown tunnel junctions LEDs

have been of great interest for industry mass production, but they face fundamental materials growth issue: Mg-doped p-type GaN will be re-passivated by the formation of Mg-H complex during the growth of n-type GaN tunnel junctions due to the crack of NH3 as precursor, which is unavoidable during MOCVD growth. The top n-GaN layers of TJs also prevent the out diffusion of H atoms during the p-GaN activation anneal, resulting in the p-GaN activation issue for the MOCVD-grown tunnel junctions. [26-27] In the conventional mesa-structure LEDs, p-GaN can be only re-activated by removing H atoms through sidewalls, which is not enough and evidenced by the brighter intensity at the edge area and darker intensity at the center area in the electrical luminous image of the tunnel junctions LEDs. Therefore, new growth strategy is required to realize efficient MOCVD grown tunnel junctions.

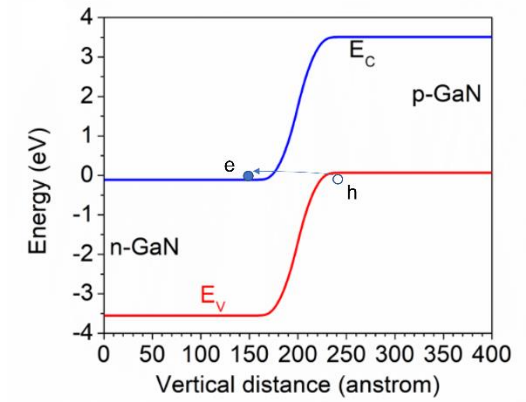

Figure 1 A band diagram for a tunnel junction with a reverse bias of 0.6 V is shown. The acceptor density used is 2.5×10^{20} cm^{-3} and the donor density is 1×10^{20} cm^{-3}.

2.2 Motivation of GaN Tunnel Junction

2.2.1 Improve hole injection in GaN-based LEDs

By operating the Tunnel junctions at a reverse biased condition, an electron in the valence band of p-type material tunnels into the empty states in the conduction band of the n-type

layer, leaving behind a hole in the p-type material, which results in hole injection into the p-type layer. Tunnel junctions offer an enhanced current injection and current spreading as it is much easier to form a good ohmic contact to n-GaN with a lower resistivity than p-GaN. [15-16] This is very important for AlGaN-based DUV LEDs. Because p-AlGaN is large bandgap materials, which is very hard to form ohmic contact with metals. In the case of deep UV LEDs, tunnel junction formed by n-AlGaN/p-AlGaN can overcome the poor ohmic contact problems since it is much easier to form ohmic contact to n-AlGaN. Also, n-AlGaN materials show lower sheet resistance and better current spreading. Besides that, Thick p-GaN cap used for hole injection layer is not required due to tunnel junctions, which can reduce the light adsorption loss. The non-equilibrium tunnel-injected holes could also be used to substitute thermally ionized holes completely, enabling bipolar devices without any p-type doping. [22] Figure 2 shows a top emitting LED structure with a tunnel junction to enable a n-type top contact. This device structure enables the replace of the relatively more challenging p-contact with low resistance n-type, which could be very important for larger bandgap AlGaN. In particular, the DUV LEDs show poor external quantum efficiency, which is about 10%. [23] Hole injection efficiency and light extraction become major bottlenecks. Therefore, UV tunnel junctions could be very promising for high efficiency UV LEDs.

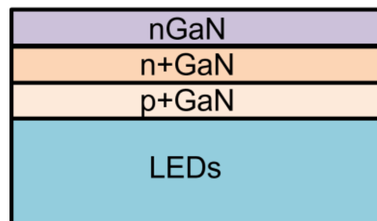

Figure 2 Epitaxial structure and schematic band diagram showing hole injection in p-GaN using a reverse biased tunnel junction

2.2.2 multi-junctions devices

Tunnel junctions play an important role in multi-junction devices (Figure 3), such as in multi-color cascaded LEDs, [24] and multi- junction solar cells[19-20] This is very attractive in the III- nitride materials system, which enables monolithic integration for applications such

as full color white LEDs in one device. For example, we can grow blue, green and red InGaN-based LEDs on one wafer, connecting by tunnel junctions. Thus, full color LEDs can be achieved by independently controlling injection current through multiple electrodes. This technology is especially important for Micro-LEDs display application by saving huge effort about mass transfer and assemble millions of RGB Micro-LEDs.

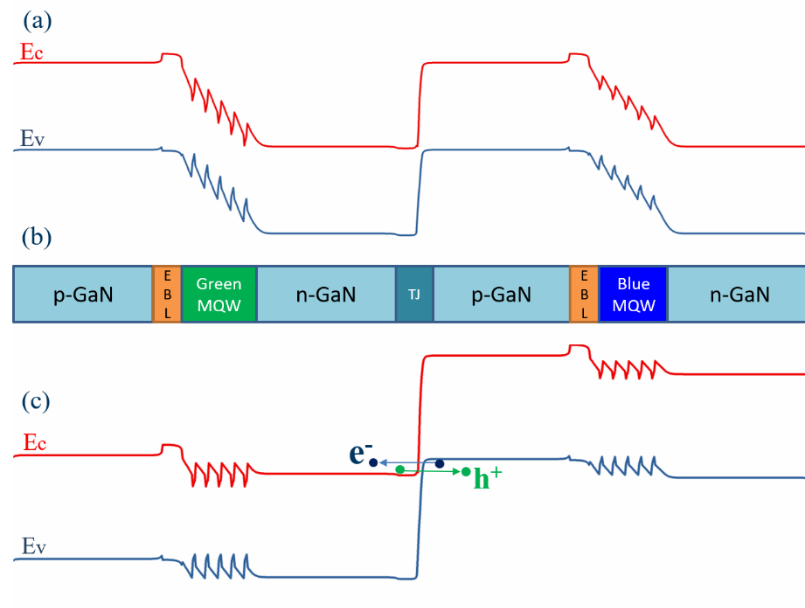

Figure 3 Schematic band diagram and epitaxial structure of multiple active regions connected in series with interband tunnel junctions.

2.2.3 Solution to efficiency droop using carrier regeneration in tunnel junctions

GaN-based LEDs have been widely commercialized, and the efficiency of LEDs is very crucial for application. LEDs would need to be operated at very high output power density

while maintaining high efficiency during application. Typically, the peak efficiency values of GaN-based LEDs at low current density are high, but the efficiency decreases dramatically when the injection current increases. This is efficiency droop effect. For the multiple cascaded LEDs connected in series using tunnel junction interconnects, the devices can be operated at low current density with a higher operating voltage as compared to a single LED worked at high current density for high output power. The cascaded LEDs structure enables a high light output power while still operating each LED at a low current density. [25] Therefore, the efficiency droop effect can be alleviated. This results in an overall high wall plug efficiency. Also, the epitaxial cascading of active regions leads to a reduction of semiconductor material cost.

2.3 Review of the development of Tunnel junction

2.3.1 Development of Tunnel Junction grown by MBE

In 2013, Krishnamoorthy et al. in the Ohio State University reported enhanced interband tunnel injection of holes into a p-n junction by using p-GaN/InGaN/n-GaN tunnel junctions grown by MBE. [8] The tunnel junctions show a specific resistivity of $1.2\times 10^{-4}\ \Omega cm^2$. The structure consists of a GaN p-n junction on top of a p-GaN/4nm $In_{0.25}Ga_{0.75}N$/n-GaN tunnel junction, so that tunneling is used to inject holes into the p-type layer of the p-n junction. Ti (20 nm)/Au (200 nm) ohmic contacts were deposited for the top n-contact, followed by mesa isolation, and then evaporation of the bottom n-type contact. No p-type contact formation is necessary since the holes are injected by the tunnel junction. This p-contact less p-n junction device ($50\mu m \times 50\mu m$) shows very excellent electrical characteristics and shows p-n junction behavior with rectification. The total series resistance

of the device in forward bias was found by fitting the linear region of the forward bias characteristics to be $4.7\times 10^{-4}\Omega cm^2$. The specific resistivity of the tunnel junction is lower than $1.2\times 10^{-4}\Omega cm^2$. At a forward current density of 100A/cm^2, the voltage drop across the p-n junction is 3.05V, and the voltage drop across the tunnel junction is 12mV. Then in 2014, Krishnamoorthy et al. reported the InGaN/GaN tunnel junction contacts grown using plasma assisted MBE on top of a 450 nm-InGaN/GaN blue LED. In this tunnel junction LED, a voltage drop of 5.3V at 100mA and forward resistance of $2\times 10^{-2}\Omega cm^2$ were measured. Compared with the reference LEDs with semi-transparent p-contacts, the tunnel junction LED shows higher light output power.

In 2016, Yong et al. in the UCSB demonstrated very low forward voltage semi-polar LEDs with highly doped GaN p–n tunnel junction contacts.[11] The n-GaN tunnel junction layer was grown by NH_3 MBE on LED where the active region and the top p-GaN layers were grown by MOCVD. Although the growth of GaN by NH_3 MBE which is a hydrogen-rich growth environment, the hydrogen levels are several orders of magnitude less than those existed during the growth process in MOVCD. The NH_3 MBE growth can not only lead to high-quality, active p-GaN, but also result in a n-GaN layer with excellent transport properties and high Si doping level. In their work, for a (20-21) n-GaN layer, the carrier concentration was 1.1×10^{20}/cm^3 and the mobility was found to be 126 cm^{2}V^{-1}S^{-1} with a resistivity of 4.3×10^{-4} Ωcm. LEDs with tunnel junction were fabricated as compared to LEDs with common ITO contact. The tunnel junction LEDs show a lower forward voltage. The voltage of tunnel junction LEDs at 20mA was 5.2V, which was lower than the ITO LEDs (5.87V).

In 2016, Yonkee et al. in the UCSB grew a GaN tunnel junction on standard industrial patterned sapphire substrate blue LED (455nm) epitaxial wafers by MBE regrowth

technique.[12] Several acid treatments before regrowth was tried and they show different effects. The forward voltage at 20A/cm^2 on small area devices was reduced from 4.33 to 3.30V when the surface was treated with HCl. An aqua regia treatment gave a voltage of 3.1V, and a 49% HF treatment gave the best voltage of 3.08V. Furthermore, the flip chip LED shown a very high peak external quantum efficiency (EQE) of 78% at 5 A/cm^2, and wall plug efficiency (WPE) of 73% at 1.5 A/cm^2. This is one of the highest EQE reported among InGaN-based LEDs. Because tunnel junction can increase light extraction by reducing optical loss from transparent conducting oxide (TCO) designs such as indium doped Tin oxide (ITO), tunnel junction shows huge potential in improving EQE of GaN-based LEDs.

2.3.2 Development of Tunnel Junction grown by MOCVD

The challenge of MOCVD grown tunnel junction is the activation of p-GaN. The Mg acceptors are passivated with hydrogen atoms in the ammonia ambient during the tunnel junction growth by MOCVD, resulting in Mg-H bond formation. Several groups have reported that hydrogen atoms exist in Mg-doped GaN, but not in undoped or Si-doped GaN even after thermal annealing with hydrogen ambient. It has been explained that hydrogen atoms can only migrate in p-type materials, but not in n-typed materials. Further elucidated, hydrogen atoms in the p-type layers could not pass through the n-typed layers. In 2013, Kuwano et al. from Meijo University demonstrated lateral Mg activation along p-GaN layers.[28] At first, a LED with epitaxy tunnel junction was grown by MOCVD. The thermal annealing was carried out after the etching of LED mesa. Therefore, a portion of the p-GaN layer as an etched sidewall was exposed and the hydrogen can diffuse through the sidewall. It was found that the emission at edge area is brighter than the center area, which is caused by nonuniformity of current

injections at the tunnel junctions. This can be explained by nonuniform p-GaN activation: Mg acceptors are activated first at the sidewalls of the LEDs where p-GaN layers are directly exposed and then extend from the edge to the center.

MOCVD is the standard for the commercialization of GaN-based devices. But the tunnel junctions grown by MOCVD suffers the challenge of p-type GaN re-passivation as mentioned above. In 2018, Hwang et al. from UCSB reported micro-light-emitting diodes (μLEDs) with tunnel junction (TJ) contacts grown entirely by MOCVD. [29] It was found that the forward voltage reduces linearly with the size of the μLEDs, which proves that sidewalls are the only path for the out diffusion of hydrogen. The voltage penalty of the TJ for the smallest μLED at 20A/cm^2 was 0.60 V compared to a standard LED with ITO contact. The peak EQE of the TJ LED was 34%. Overall, the forward voltage of the μLEDs with MOCVD-grown tunnel junctions was higher than 4.0 V.

2.4 Tunnel junctions using selective area growth by metalorganic chemical vapor deposition

We proposal selective area growth (SAG) for the TJs growth using MOCVD. Standard industry blue InGaN LEDs epitaxial wafers grown on patterned sapphire substrate (PSS) with an emission wavelength at ~440 nm were used for the TJs regrowth. The concept of GaN TJs LEDs grown using SAG is schematically illustrated in Fig. 4(a). Patterned n+GaN/n-GaN were grown on top of p-GaN to form TJs by SAG. In this design, hydrogen can be vertically out diffused from the holes on top of the p-GaN surface as well as the sidewall. 210 nm thick SiO_2 pillars with a diameter of 1.5 μm and a space of 3.5 μm were formed on top of the p-GaN as hard mask. 20 nm/400 nm thick n+GaN/n-GaN TJ layers with Si concentration of

1.5×10^{20} and 3×10^{18} cm^{-3} were grown on top of the p-GaN using SAG by MOCVD. In the reference TJ μLEDs, the n+GaN/n-GaN layers were grown directly on top of the standard LEDs without using SAG. μLEDs with squared sizes ranging from 10×10 to 100×100 μm^2 were fabricated. Silicon tetrachloride ($SiCl_4$) was used to expose the n-GaN mesa in a reactive-ion etching (RIE) chamber. The SiO_2 pillars were removed by buffered hydrofluoric acid. The μLEDs were annealed at 700 °C for 30 minutes under N_2 ambient in order to remove the hydrogen and activate the p-GaN. An omnidirectional reflector (ODR) consists of silicon dioxide and tantalum pentoxide was deposited by ion beam deposition. SiO_2 was blanket deposited by atomic layer deposition (ALD) to passivate the mesa sidewall. [30, 31] Al/Ni/Au (600/100/600 nm) were deposited as metal contact and pads. The fabricated 80×80 μm^2 TJ μLEDs with pinholes formed by SAG can be clearly observed from the microscope image in Fig. 4(b) and the scanning electron microscopy (SEM) image in Fig. 4(c). These small holes regularly distributed on top of the p-GaN surface, act as an additional diffusion path for hydrogen during p-GaN activation. Finally, the μLEDs were diced, mounted onto silver headers, encapsulated using silicone, and measured in a calibrated integrating sphere.

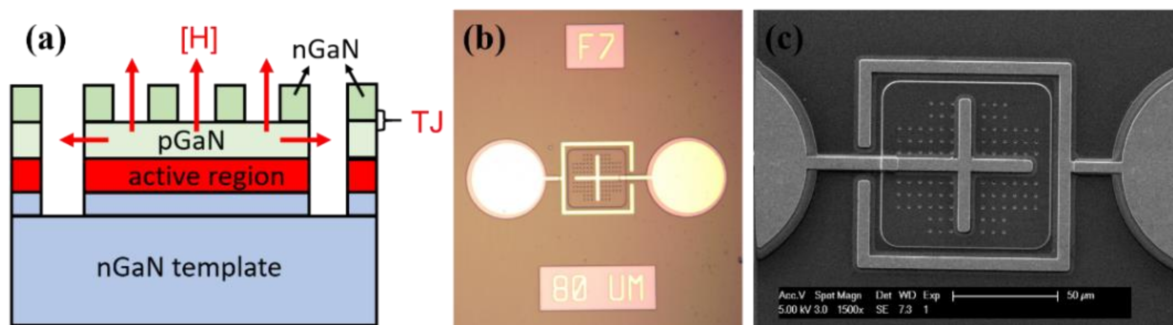

Figs. 4(a) Schematic structure of GaN TJ μLEDs grown by SAG; (b) Microscope image and (c) SEM image of the fabricated 80×80 μm^2 SAG TJ μLEDs.

Optical luminous images of the reference TJ μLEDs and the SAG TJ μLEDs under a forward current density of 1 A/cm^2 by microscopy are presented in Figs. 5. The luminous images of the reference TJ μLEDs are nonuniform. The luminous intensity at the edge is brighter than the center area in the reference TJ μLEDs with sizes from 60×60 to 100×100 μm^2, likely caused by the nonuniformity of current injections at the TJ and the re-passivated p-GaN. [26] Therefore, the p-GaN was not fully activated by removing the hydrogen laterally through sidewall in the reference TJ μLEDs. By contrast, the luminous images of the SAG TJ μLEDs exhibit excellent uniformity for all sizes. In SAG TJ μLEDs, the hydrogen can be removed through the holes on top of the p-GaN surface in addition to the sidewall, resulting in a significant improvement of the p-GaN activation efficiency.

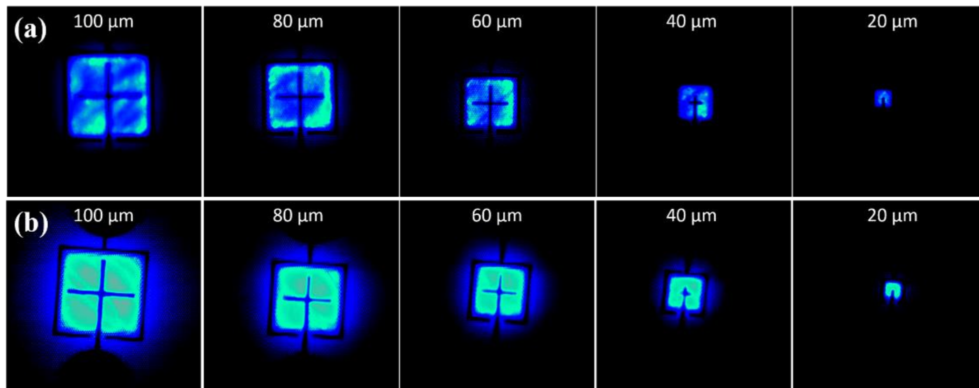

Figs. 5. Luminous microscope images of (a) reference TJ μLEDs without SAG and (b) TJ μLEDs using SAG. The devices' sizes were varied from 100×100 to 20×20 μm^2.

The current density-forward voltage (J-V) characteristics of the reference TJ μLEDs and the SAG TJ μLEDs with different sizes were plotted in Figs. 6(a) and 6(b), respectively. The reference TJ μLEDs show much higher forward voltage overall, and an increase in forward voltage with mesa size. [29] In our other samples of the reference TJ μLEDs, the forward

voltage is even much higher, which indicates that the uniformity and the repeatability of TJs directly grown by MOCVD was not good. It is worth noting that the TJ μLEDs with SAG show very similar J-V curves for the sizes from 100×100 μm^2 down to 10×10 μm^2 as shown in Fig. 6(b). The forward voltage is significantly reduced in the SAG TJ μLEDs due to an improvement of the p-GaN activation efficiency.

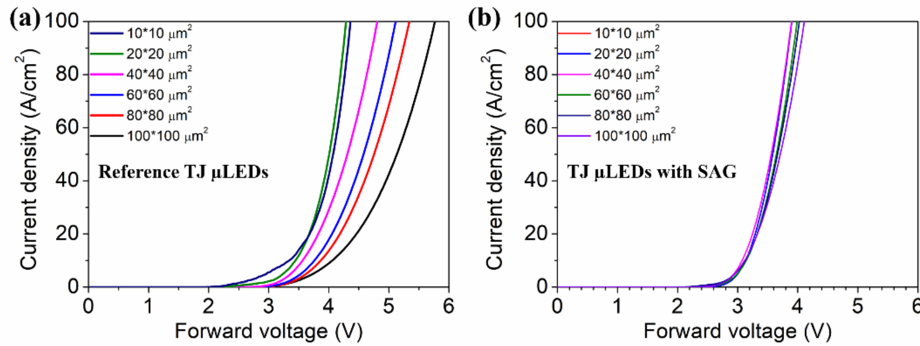

Figs. 6. Current density-forward voltage curves of (a) reference TJ μLEDs and (b) TJ μLEDs using SAG with device sizes varied from 100 to 10000 μm^2.

Furthermore, the forward voltage (V_f) at 20 A/cm^2 of the reference μLEDs and the SAG TJ μLEDs are plotted in Fig. 7. The V_f in the reference TJ μLEDs decreases linearly with the area. As the size reduces from 10000 to 100 μm^2, the V_f at 20 A/cm^2 decreases from 4.6 to 3.7 V. In the reference TJ μLEDs, the hydrogen can only be laterally out diffused from the sidewall to active the p-GaN, leading to a decrease of the V_f with reducing size. [26, 29] It is obvious that the removal of hydrogen through sidewall is inefficient to fully activate the p-GaN since the V_f is much higher than that of the common InGaN LEDs ITO contacts (~3.0 V, not shown here and will present in our other submission). By contrast, the V_f at 20 A/cm^2 of TJ μLEDs with SAG is significantly reduced to 3.24 to 3.31 V, which is much lower than that in the reference TJ μLEDs. It is worth noting that the V_f in the TJ μLEDs with SAG is

independent on the sizes. In the SAG TJ µLEDs, the hydrogen can be vertically driven out through the holes on top of the p-GaN surface, which plays a dominant role over the lateral diffusion from the sidewall. Such size-independence V_f is caused by the hole created by the oxide pillars, since thermally activated hydrogen can diffuse a shorter distance to a hole as opposed to having to diffuse to a sidewall. For the smallest 10×10 and 20×20 µm^2 µLEDs, the V_f at 20 A/cm^2 of TJ µLEDs reduction is less pronounced. This agrees well with the reduction of the forward voltage in reference TJ µLEDs with small sizes caused by the lateral out diffusion of hydrogen. It is worth to point out that the V_f in our SAG TJ LEDs is only 0.2 to 0.3 V higher than the LEDs with ITO contact. To the best of our knowledge, these forward voltages are the lowest for the GaN LEDs with TJs grown by MOCVD, [26, 29] and comparable to the lowest for GaN LEDs with TJs grown by MBE. [32, 2] These results clearly suggest that the hydrogen can be effectively removed through the holes on top of the p-GaN surface, leading to a successful realization of GaN-based LEDs with epitaxial TJs grown by MOCVD.

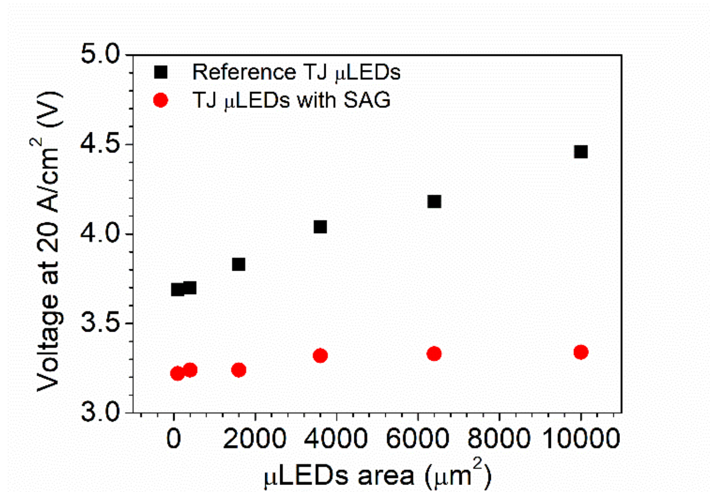

FIG. 7. Forward voltage at 20 A/cm^2 versus µLEDs area for the reference TJ µLEDs and GaN TJ µLEDs with SAG.

Finally, the output power measured at 20 mA for the SAG TJ μLEDs and the conventional μLEDs with ITO contact from the same epitaxy wafer are shown in Fig. 8(a). For the different mesa sizes, the output power in the SAG TJ μLEDs is obviously higher than the common ITO μLEDs at a same current density. The average increase of the output power was measured to be around 10% for all the sizes. Fig. 8(b) shows the external quantum efficiency (EQE) versus current for the packaged conventional ITO μLEDs and the SAG TJ μLEDs with a same size of 40×40 μm^2. The EQE was increased from 35% of the ITO μLEDs to 40% of the SAG TJ μLEDs at 100 A/cm^2. Such enhanced efficiency is attributed to the improvement of the light extraction efficient due to the small holes on top of the p-GaN. The improved current spreading and reduced light absorption of the TJs could be other factors for the efficiency enhancement.

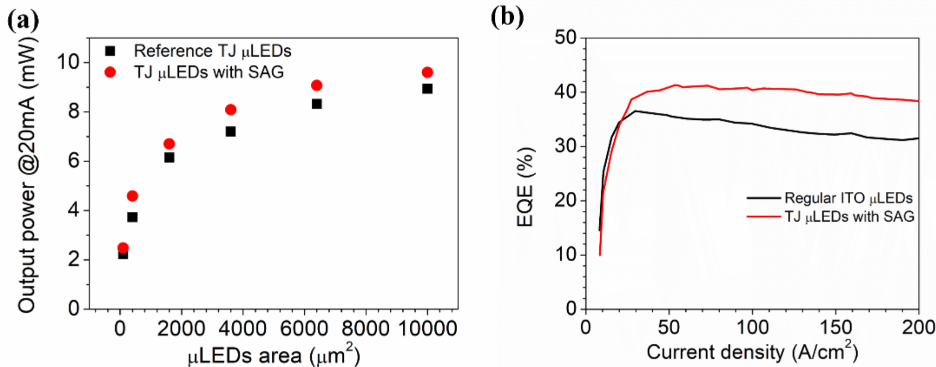

FIG. 8. (a) Output power at 20 mA versus various sizes in the TJ μLEDs with SAG and the common ITO μLEDs; (b) EQE versus current density in TJ μLEDs with SAG and common ITO μLEDs with a size of 40×40 μm^2.

2.5 MOCVD grown $n^+GaN/n\text{-}InGaN/p^+GaN$ tunnel junctions

In the following chapters, we will go through polarization engineering TJs by inserting n-InGaN before n-GaN to increase the tunneling probability. In order to obtain a high p-GaN activation efficiency, we utilize selective area growth (SAG) to regrow the InGaN TJs. [33, 34] Finally, we demonstrate MOCVD grown InGaN TJs μLEDs exhibiting lowest forward voltage among TJ LEDs. Details of the materials growth, devices fabrication and devices performance are discussed.

The TJs were epitaxially grown by MOCVD on commercial 440 nm blue LEDs on patterned sapphire substrate (PSS). Three sets of samples were grown in our experiments. Surface treatment by solvent clean and aqua regia was carried out before the regrowth of TJs.[2] In the reference TJ μLEDs, conventional n^+-GaN/n-GaN (20 nm/350 nm) TJs were grown directly on top of blue LEDs with a Si doping concentration of 1.7×10^{20} and 3×10^{18} cm^{-3}, respectively. A 15 nm n-GaN cap layer with a Si doping concentration of 2×10^{19} cm^{-3} were grown on top for a good ohmic contact. For the second set of TJ μLEDs, a 3 nm n-$In_{0.15}Ga_{0.85}N$ with a Si doping concentration of 1.5×10^{20} cm^{-3} was grown before n^+-GaN, which is referred as InGaN TJ μLEDs. For the last set of samples, the InGaN/GaN TJs were grown utilizing SAG, which is referred as SAG InGaN TJ μLEDs. Details of the TJs grown by SAG can be found in our other report.[33] The schematic structure of the InGaN TJ μLEDs is shown in Figure 9, with squared sizes ranging from 10×10 to 100×100 μm^2 were fabricated. To re-activate the p-GaN, the devices were annealed at 700 °C for 30 minutes using rapid thermal annealing (RTA). For the SAG InGaN TJ μLEDs, the SiO_2 pillars as hard mask were removed by buffered hydrofluoric acid before annealing. Silicon tetrachloride ($SiCl_4$) was used to expose the n-GaN mesa in RIE chamber. An omnidirectional reflector (ODR)

consisted of silicon dioxide and tantalum pentoxide was deposited by ion beam deposition. 25 nm SiO_2 was deposited as sidewall passivation layer by ALD. [31] Al/Ni/Au (600/100/600 nm) were deposited on the opening window for ohmic contact and contact pads. Finally, the µLEDs were diced, mounted on silver headers, encapsulated with silicone, and measured in a calibrated integrating sphere.

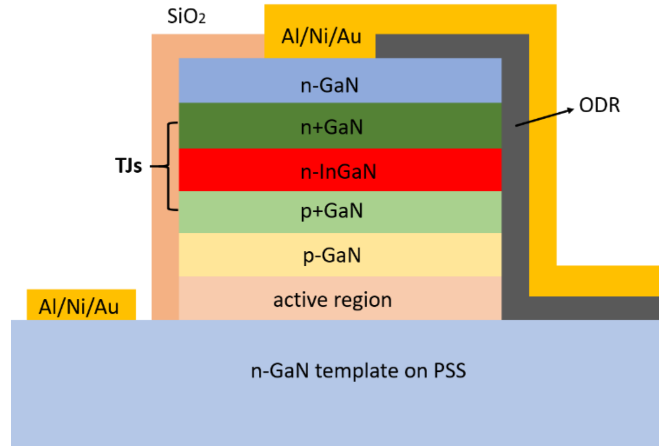

Fig. 9. Schematic structure of the InGaN TJ µLEDs.

Figures 10(a) and 10(b) are the scanning electron microscopy (SEM) images of the fabricated 60×60 μm^2 InGaN TJ µLED and SAG InGaN TJ µLED. The TJs layer can be clearly observed with a same contrast as the etched n-GaN. In Figure 10(b), small 1.5 µm diameter apertures with 3.5 µm spacing were regularly distributed on the top of p-GaN surface after removing the SiO_2 pillars.[33] These apertures provide a pathway, that circumvents the pn junction (and natural internal barrier for H+ diffusion) to remove hydrogen from the sample and thus realize a high activation efficiency.

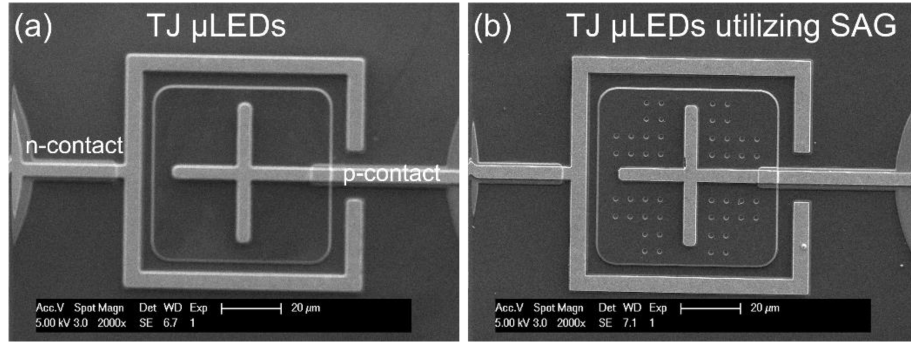

Figs. 10. SEM images of the fabricated 60×60 μm^2 size of (b) InGaN TJ μLEDs and (c) SAG InGaN TJ μLEDs.

Figure 11 show the optical luminous images of the InGaN TJ μLEDs and the SAG InGaN TJ μLEDs with various sizes under a current density of 1 A/cm^2. Both InGaN TJ μLEDs and SAG InGaN TJ μLEDs with different sizes show very uniform luminous intensity for the size varied from 20×20 μm^2 to 100×100 μm^2. We notice that the luminous images of the reference TJ μLEDs were not uniform with a brighter electrical luminous (EL) intensity at the edge and a darker EL intensity at the center area, which is shown in Ref. 33. Those uniform luminous images in the InGaN TJ μLEDs are ascribed to the improvement of the current injection efficiency due to a higher tunneling probability at the InGaN TJs.

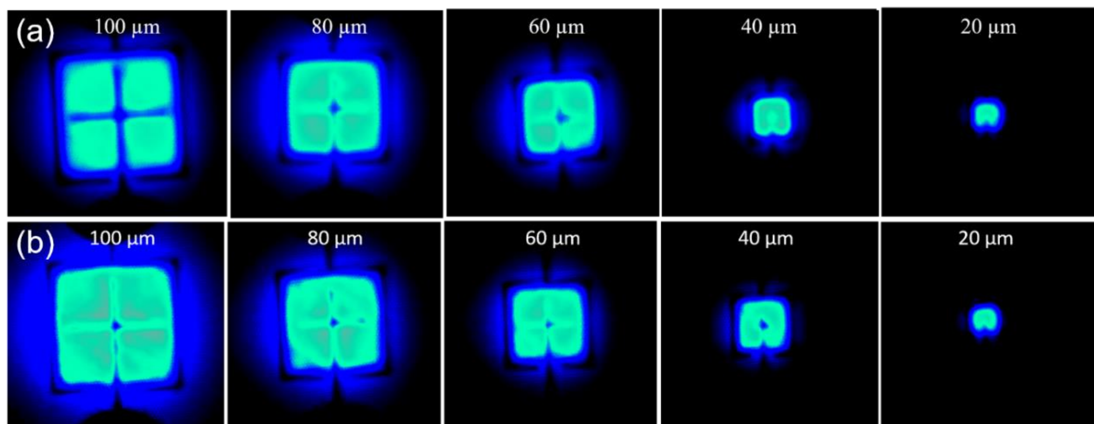

Figs. 11. Luminous microscope images of (a) InGaN TJ μLEDs and (b) SAG InGaN TJ μLEDs with size varied from 100×100 to 20×20 μm^2.

The current density-forward voltage (J-V) characteristics of the three sets of TJ μLEDs with different sizes are shown in Figure 12(a) to 12(c). The reference TJ μLEDs show much higher forward voltage from Figure 12(a), which decreases with the reduction of size. By contrast, the forward voltage is significantly reduced in the InGaN TJ μLEDs as shown Figure 12(b). It is clear to see that the voltage is still dependent on the size, which decreases as the size reduces. It is worth noting that the SAG InGaN TJ μLEDs exhibit very uniform and similar J-V curves from Figure 12(c). More specifically, the V_f at 20 A/cm^2 of these three sets of TJ μLEDs are plotted in Figure 12(d). The V_f in the reference TJ μLEDs remain high and decreases linearly from 4.6 to 3.7 V with reducing sizes from 100×100 to 10×10 μm^2. This can be explained by laterally out diffused of hydrogen through the sidewall, which is the only path to remove the hydrogen in order to re-active the p-GaN. In the InGaN TJ μLEDs, the V_f is significantly reduced by ~0.6 V for all sizes compared to the reference TJ μLEDs, which is caused by the enhanced tunneling probability as shown from the energy band diagram above. As the devices size decreases from 100×100 to 10×10 μm^2, the V_f reduces from 3.86 to 3.16 V, which is caused by the same reason in the reference TJ μLEDs. For the very small size InGaN TJ μLEDs from 10×10 to 40×40 μm^2, the V_f is varied from 3.15 to 3.19 V, which are very low as compared to the values reported of the TJ LEDs from other groups. [1, 2, 29,35-36] For the 60×60 μm^2 μLEDs, the V_f increases to 3.39 V and then dramatically raises to 3.86 V for the 100×100 μm^2 size. Therefore, very low forward voltage can only be achieved in small size μLEDs using InGaN TJs as the removal of hydrogen through sidewall is insufficient for larger LEDs. It is worth noting that the SAG InGaN TJ μLEDs show very uniform and low V_f of 3.08 to 3.25 V for the sizes varied from 10×10 to 100×100 μm^2. For the 20×20 μm^2

and 40×40 μm^2 size devices, the InGaN TJ μLEDs and SAG InGaN TJ μLEDs show the same low V_f. The lowest V_f of 3.08 V is obtained in the smallest 10×10 μm^2 SAG InGaN TJ μLEDs. The apertures on the p-GaN surface by SAG create additional vertical out diffusion paths for the hydrogen with a much shorter diffused distance than that to sidewall. Such design overcomes the size limitation in the InGaN TJs μLEDs with low voltage, which is very important for the large size μLEDs even the regular size LEDs. It is well known that decomposing the Mg-H complex in the p-GaN by thermal annealing and removing hydrogen atoms are the key points to active the p-GaN. SAG is a promising technology to remove the hydrogen atoms from the apertures on top surface to fully re-active the p-GaN without bringing any damage to the materials crystal quality or devices performance. We note that the V_f of the μLEDs with ITO contact from the same epitaxy wafer is varied from 2.93 to 2.97 V and independent on the sizes. In general, the V_f of the SAG InGaN TJ μLEDs are only 0.1 to 0.2 V higher than the ITO μLEDs, which are the lowest forward voltages reported among the GaN-based LEDs with TJs contact grown by MOCVD [28, 33~36] and comparable to that grown by MBE. [1, 2]

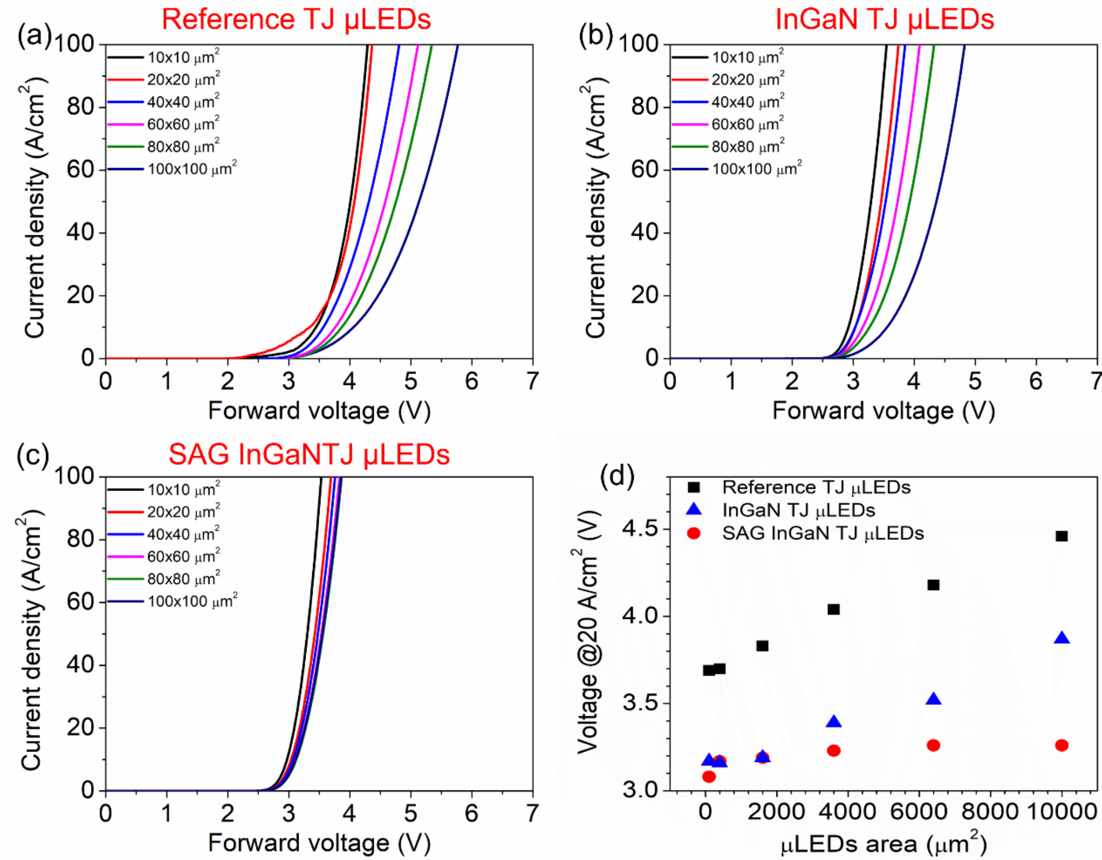

Figs. 12. (a) to (c) Current density-forward voltage curves of the three sets of µLEDs with sizes ranging from 10×10 to 100×100 µm^2; (d) Plot of V_f at 20 A/cm^2 of the three sets of µLEDs as a function of size.

The external quantum efficiency (EQE) of the packaged µLEDs with size of 40×40 µm^2 and 100×100 µm^2 at various current densities was presented in Figure 13. For a fair comparison, µLEDs with ITO contact were fabricated on the same epitaxy wafer. For the 100×100 µm^2 µLEDs, the EQE at 20 A/cm^2 was increased by 6% from 48% of the ITO µLEDs to 54% of the InGaN TJ µLEDs with SAG. For the InGaN TJ µLEDs, the EQE shows a slight increase by ~2%, which is limited to the insufficient p-GaN activation by the lateral out diffusion of hydrogen through sidewall. In the small 40×40 µm^2 µLEDs, the InGaN TJ µLEDs

and the SAG InGaN TJ μLEDs show a similar EQE, which is also 6% higher than the ITO μLEDs. The same EQE of the InGaN TJ μLEDs with and SAG InGaN TJ μLEDs indicates that the small apertures on top of the p-GaN surface can't further increase the light extraction efficiency (LEE) for the LEDs grown on PSS. Therefore, the improvement of the EQE is most likely resulted from the TJs with a higher transparency and a better current spreading. [1, 2]

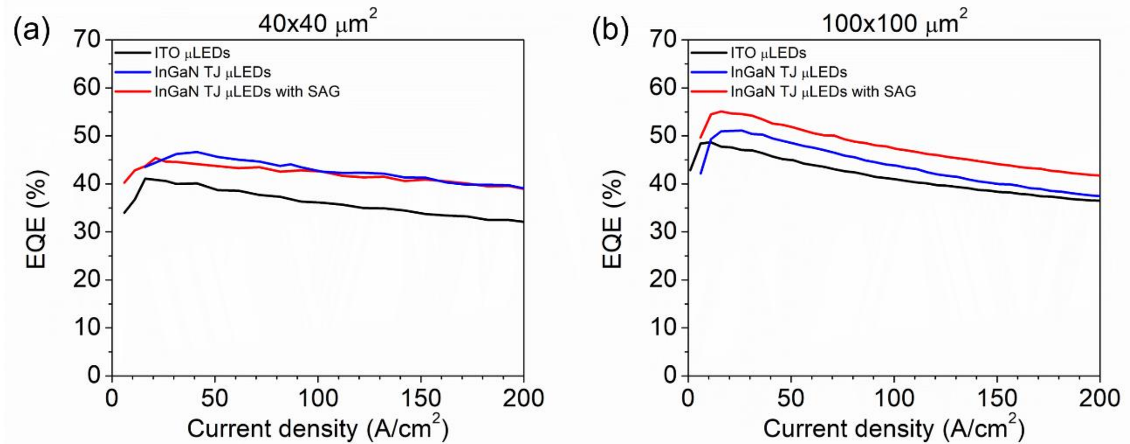

Figs. 13. EQE versus current density of the three sets of the packaged μLEDs with a size of (a) 40×40 μm^2 and (b) 100×100 μm^2.

In conclusion, we achieved highest performance of MOCVD grown TJ μLEDs with very low forward voltages utilizing n-InGaN/n+GaN structure and SAG technology. For μLEDs with a size smaller less than 40×40 μm^2, low forward voltage can be obtained by directly growing InGaN TJs by MOCVD without additional SAG process, which will expedite the development of future optoelectronic III-nitride devices with TJs such as cascaded LEDs with multiple color emissions and TJs LDs and vertical cavity surface emitting laser (VCSEL).

2.6 MOCVD grown n+GaN/n-InGaN/p+GaN tunnel junctions combined SAG technology.

In the following chapters， we demonstrate the comprehensive study about the optimization of efficient MOCVD-grown TJs by selective area growth (SAG), which is a promising technology to active p-GaN for the MOCVD-grown TJs, through exposing small apertures on top of the p-type GaN that allow for hydrogen escape during the activation anneal.[37~38]. The effect of the Si-doped level in the n^+GaN TJs, SAG aperture spacing and insertion of n-type/p-type InGaN layer on the forward voltage of the TJs LEDs and µLEDs were investigated. Simulations of light extraction efficiency (LEE) and far-field radiation through light-tools and finite-difference time-domain (FDTD) on these novel structures were carried out. Finally, we demonstrate efficient MOCVD-grown TJs LEDs with a low V_f.

The TJs were epitaxially grown on commercial MOCVD-grown blue LEDs on PSS. In order to reduce the oxygen concentration at the interface, the samples were dipped into aqua regia for 5 minutes before the overgrowth of n^+GaN/n-GaN TJs, which has also been shown to reduce the incorporation of Mg atoms in the n^+GaN layer due to the residual Mg atoms as compared to one step direct growth.[36, 27, 38] As shown in Figure 14(a), TJs consisted of n^+GaN/n-GaN (20 nm/400 nm) were grown at 1100 °C utilizing SAG, which is referred as SAG TJs. A detailed description of the growth process of the SAG TJs LEDs can be found in our recent report.[33] The n^+GaN TJ was doped with a Si concentration of 1.2×10^{20} and 1.7×10^{20} cm^{-3}, while the Si-doped concentration in the n-GaN layer was fixed at 3×10^{18} cm^{-3}. The diameter of SAG aperture (circus shape) was fixed at 2 µm, and the space was varied from 3 and 8 µm. TJs with InGaN insertion layer were grown as well, as shown in Figure 14(b). A 3 nm Si-doped n-InGaN and a 3 nm Mg-doped p-InGaN with the same indium composition of

15% were grown before the n^+GaN layer, referred to InGaN SAG TJs.[25, 39] The samples were annealed at 700 °C for 30 minutes after removing SiO_2 hard mask and etching mesa. Regular 0.1 mm^2 size LEDs and micro-size LEDs (µLEDs) ranged from 20×20 to 100×100 μm^2 were fabricated. The fabrication process was given in our previous reports.[31, 37] LEDs with indium tin oxide (ITO) contact were fabricated as a reference. Finally, the LEDs were diced, mounted on silver headers, encapsulated with silicone, and measured in a calibrated integrating sphere.

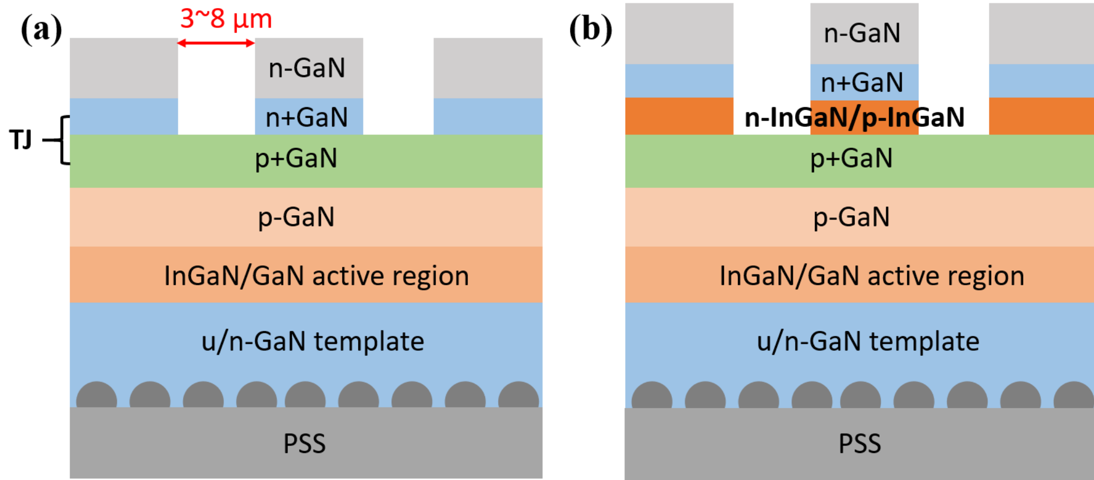

Figures 14 Schematic structure of (a) SAG TJ LEDs and (b) SAG TJ LEDs with n-InGaN or p-InGaN insertion layer.

Raytracing simulation by LightTools was carried out to simulate the LEE for the reference ITO LEDs and SAG TJ LEDs.[40] The SAG aperture space is 3 µm and the diameter is 2 µm. The LEE simulation results for the two LEDs are shown in Figures 15(a) and 15(b), respectively. Simulation results show a slight increase of the LEE by 3% in the SAG TJ LEDs (85%) compared to ITO LEDs (82%). The high LEE in the ITO LEDs is attributed to the scattering effect by the PSS (2.7-µm width, 0.3-µm space, and 1.7-µm height) and we believe that the SAG apertures could lead to a more significant improvement of LEE for the LEDs grown on a planar substrate. Moreover, FDTD by Lumerical software was also used to

simulate the far-field emission of SAG TJs LEDs and ITO LEDs.[41] For this simulation, we assume that the blue light was emitted from dipoles inside the QWs region. The excited dipoles have polarizations along the x, y, and z directions to represent the arbitrary directions of the dipole. By combining the Near-to-Far-Field transformation method with the LEE and the far-field pattern of LEDs in air can be obtained. Following the FDTD simulation, the far-field radiation pattern in air can be processed by Fourier transform and simulated through Fraunhofer diffraction relations. Lastly, far-field radiation patterns of the reference ITO LEDs and the SAG TJ LEDs are shown in Figures 15(c) and 15(d), respectively. Moreover, angular dependent of far-field intensities of ITO and SAG TJ LEDs are shown in Figures 15(e) and 15(f), respectively. There are ripples in ITO LEDs grown on PSS caused by Fabry-Pérot (F-P) interference.[42, 43] Based on this analysis, the SAG patterned surface leads to a significant increase of the output power in the normal direction, which agrees well with the LEE from the raytracing simulation. The more concentrated far-field patterned in the SAG TJ LEDs indicates a highly directional emission pattern, which could be related to the weak coupling modes and the light scatting effect caused by the SAG apertures. Similar phenomenon of more directional light pattern was reported in the nanocavity or photonic crystal InGaN LEDs, would be beneficial for the display application.[42, 43]

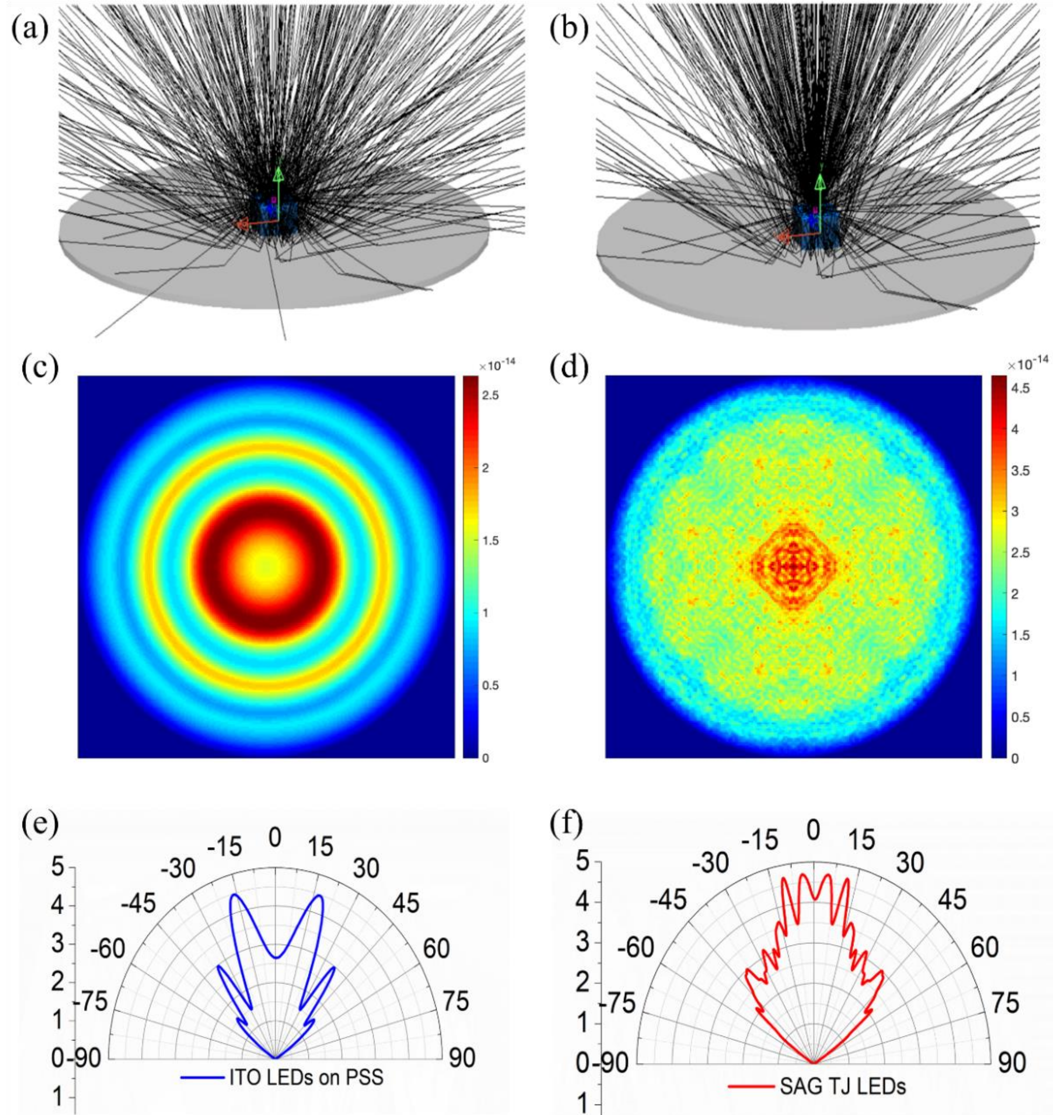

Figures 15 Emitted light distribution simulated by raytracing for (a) ITO LEDs and (b) SAG TJ LEDs; Far-field radiation patterns of (c) ITO LEDs and (d) SAG TJ LEDs; Polar plot of far-field intensities of (e) ITO LEDs and (f) SAG TJ LEDs.

Figure 16(a) shows the energy band diagram of TJs with n-InGaN insertion layer at zero bias. A polarization induced band bending at the InGaN/GaN interface is observed.[26] Band bending occurs at the InGaN/GaN heterointerfaces by those polarization charges and electric fields, resulting in a shorter tunneling distance and a higher tunneling probability.[44]

Meanwhile, the low bandgap of the InGaN layer increases the tunneling probability. Therefore, an enhanced tunneling probability is expected in the polarization enhanced InGaN TJs. The grown n-InGaN/n-GaN TJs structure is evidenced by secondary ion mass spectrometry (SIMS) as shown in Figure 16(b). It is worth noting that Si modulation doping was employed in our experiment to obtain a very high Si doping level of 1.7×10^{20} cm^{-3}, which is comparable to the highly Ge-doped GaN with a concentration of ~2×10^{20} cm^{-3}.[45] A heavily Si-doped GaN was grown for 90 s and then an undoped-GaN layer was grown for 30 s, which is repeated by 7 times for the 20 nm thick n^+GaN. This approach enables a high Si doping concentration with a good surface morphology.

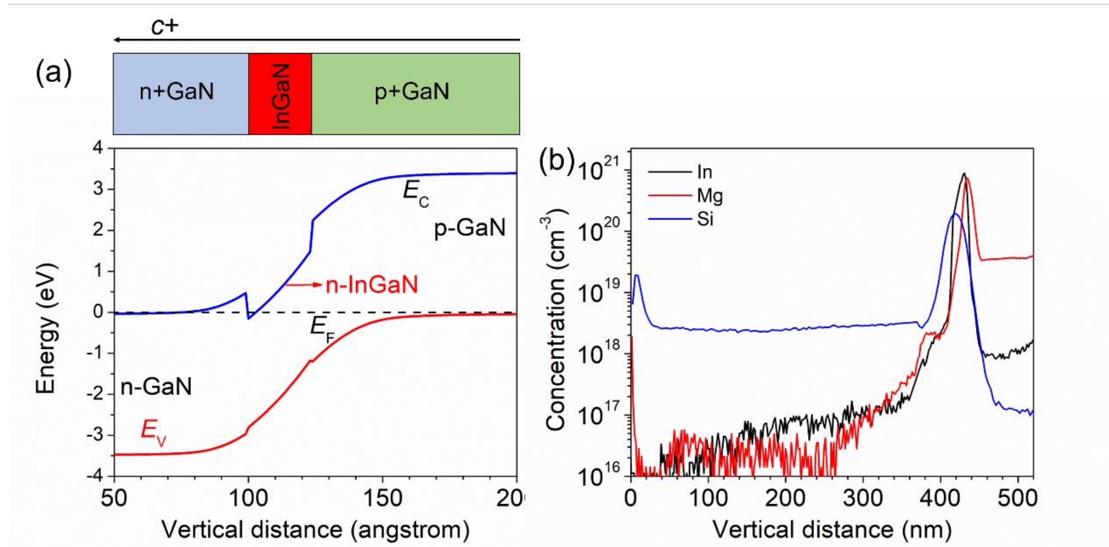

Figures 16(a) Energy band diagram of n-InGaN TJ at zero bias, and (b) SIMS of the TJ.

Figure 17(a) shows the scanning electron microscopy (SEM) image of the as-grown SAG TJ LEDs, showing clear SAG apertures. Wavy surface can be observed, indicating a good morphology. Figure 17(b) is the enlarged SEM image of the SAG apertures. Very smooth TJ surface can be seen. The diameter of the SAG aperture was measured to be ~2 µm. Figure 17(c) exhibits the fabricated SAG TJ LEDs and Figure 16(d) presents the enlarged SAG

apertures in the area labeled in Figure 17(c). Very uniform apertures were formed on the top of p-GaN surface after removing SiO_2.

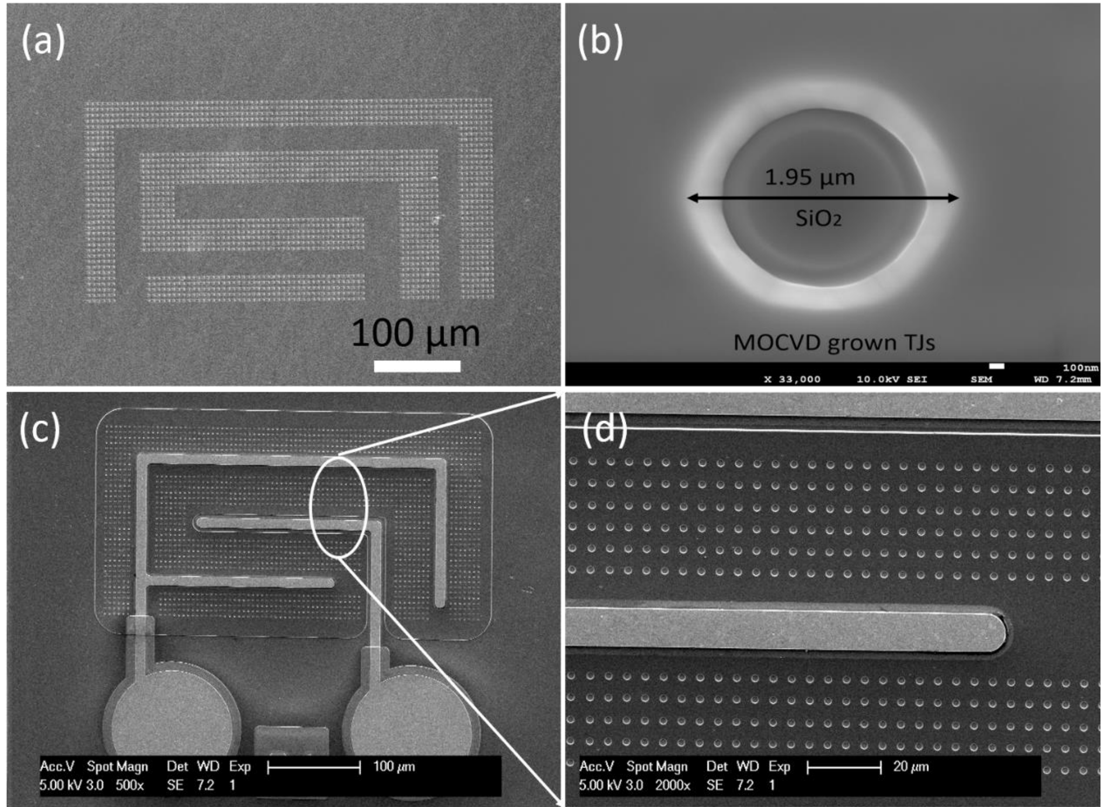

Figures 17 SEM images of (a) as-overgrown SAG TJ LEDs; (b) Enlarged aperture of the as-overgrown SAG TJ LEDs; (c) Fabricated 0.1 mm^2 SAG TJ LEDs; (d) Enlarged SAG apertures of the TJ LEDs after removing SiO_2.

Figures 18(a) and 18(b) show the EL images of the reference TJ LEDs and SAG TJs LEDs with a size of 0.1 mm^2 at 1 mA under microscope, respectively. In the reference TJ LEDs, the EL intensity at the center area is much darker than the edge area, which is usually observed in the MOCVD-grown TJs LEDs caused by a nonuniform p-GaN activation. Such phenomenon can be well explained by the insufficient hydrogen removal through lateral out diffusion through sidewalls while the top n-type layer prevent the natural vertical out diffusion of

hydrogen.[26, 27] The SAG TJ LEDs in contrast show a uniform EL intensity at the both center and edge areas, indicating a uniform p-GaN activation anneal. This is because that the SAG apertures on the top p-GaN surface shown in Figure 17(d) create shorter paths for the hydrogen thermal out diffusion through the p-GaN surface during the post activation anneal.[33, 37]

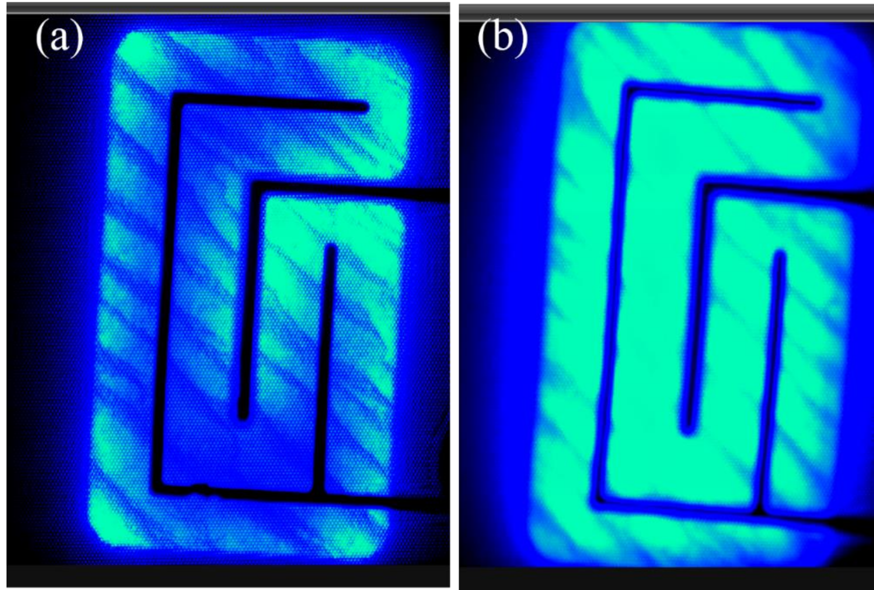

Figures 18 EL images of (a) reference TJ LEDs (0.1 mm^2) and (b) SAG TJ LEDs under microscope.

Figure 19(a) shows the current density-forward voltage (J-V) curves of the 0.1 mm^2 SAG TJ LEDs with different aperture spacing and Si-doped concentrations. The J-V curve of the reference TJ LEDs without SAG is shown for a comparison. For the samples with a Si-doped concentration of 1.2×10^{20} cm^{-3} in n^+GaN, the V_f at 20 A/cm^2, was decreased from 4.8 V in reference TJ LEDs to 3.7 V and 4.0 V in the SAG TJ LEDs with apertures spacing of 3 and 8 µm, respectively. As the Si-doped concentration increases to 1.7×10^{20} cm^{-3}, the V_f is significantly reduced to 3.45 V for both SAG TJ LEDs with the apertures space of 3 and 8 µm. The highly Si-doped SAG TJ LEDs with different apertures spaces of 3 and 8 µm show

a same J-V curve, indicating a SAG aperture space-independent voltage. As hydrogen can diffuse from the SAG apertures on top of p-GaN surface, the p-GaN activation efficiency is significantly improved. The narrow aperture space is beneficial for direct escape of hydrogen. The same J-V curves in the SAG TJ LEDs with different aperture spaces indicate that the re-activation efficiency of the p-GaN is high enough by increasing the Si-doped concentration of n⁺GaN. The V_f at a current density of 20 A/cm² of the different Si doped SAG µLEDs TJs with area varied from 10×10 to 100×100 µm² is plotted in Figure 19(b). For SAG TJ µLEDs

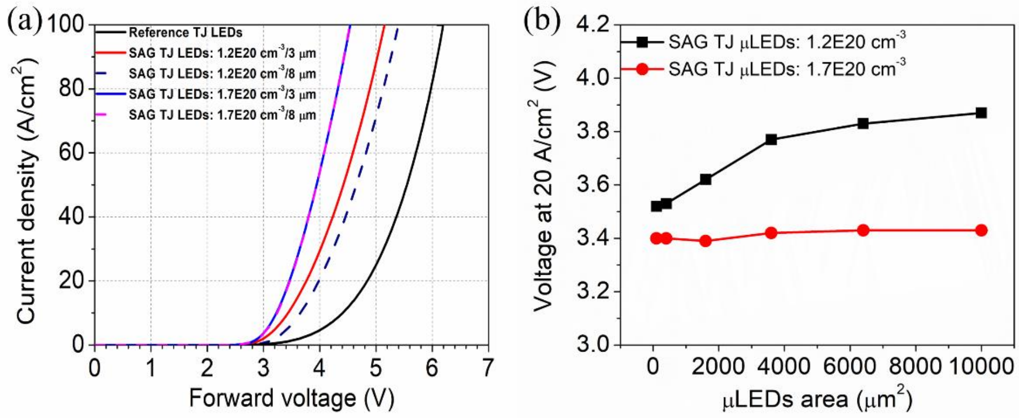

Figures 19(a) J-V curves of SAG TJ regular LEDs with different n⁺GaN Si doping concentration and aperture space; (b) V_f at 20 A/cm² versus SAG µLEDs area varied from 10×10 to 100×100 µm².

with a n⁺GaN Si doping concentration of 1×10^{20} cm^{-3}, the V_f is reduced from 3.86 V to 3.51 V with decreasing devices area from 100×100 to 10×10 µm², indicating that the tunneling probability remains insufficient. It is worth noting that the V_f is independent on the devices area by increasing the Si-doped concentration in the n⁺GaN to 1.7×10^{20} cm^{-3}, which is slightly reduced to 3.4 V. Consequently, these results clearly point out that the Si doping concentration of n⁺GaN is an important parameter for the efficient TJs, which can be understood by the reduction of depletion width and the increase of tunneling probability from Eq. (2).

Figure 20(a) plots the J-V curves of the SAG TJs LEDs with n-InGaN or p-InGaN insertion layers and ITO regular size LEDs. The SAG n-InGaN TJ LEDs show very similar J-V curves as compared to the SAG TJ LEDs, with a very small V_f difference of 0.02 V. A significant reduction of forward voltage was not observed for the SAG n-InGaN TJ LEDs in this study since the Si doping concentration in the n^+GaN has been optimized and the TJs were grown utilizing SAG. On other hand, the SAG TJ p-InGaN LEDs exhibit a voltage of 0.25 V higher than the SAG TJ LEDs, which is possibly related to the incorporation of residual Mg atoms in the n^+GaN TJs after the growth of p-InGaN. It is worth to point out that the V_f at 20 A/cm^2 in SAG TJ LEDs or SAG n-InGaN TJ LEDs is 3.45 V, which is only ~0.2 V higher than the ITO LEDs of 3.26 V. On other hand, the effect of the n-InGaN or p-InGaN SAG TJs on the J-V curve of the 20 μm ×20 μm μLEDs was shown in Figure 20(b). The p-InGaN SAG TJ LEDs show a similar forward voltage. In the n-InGaN SAG TJ μLEDs, the V_f was reduced to 3.17 V from 3.42 V of SAG TJ μLEDs.

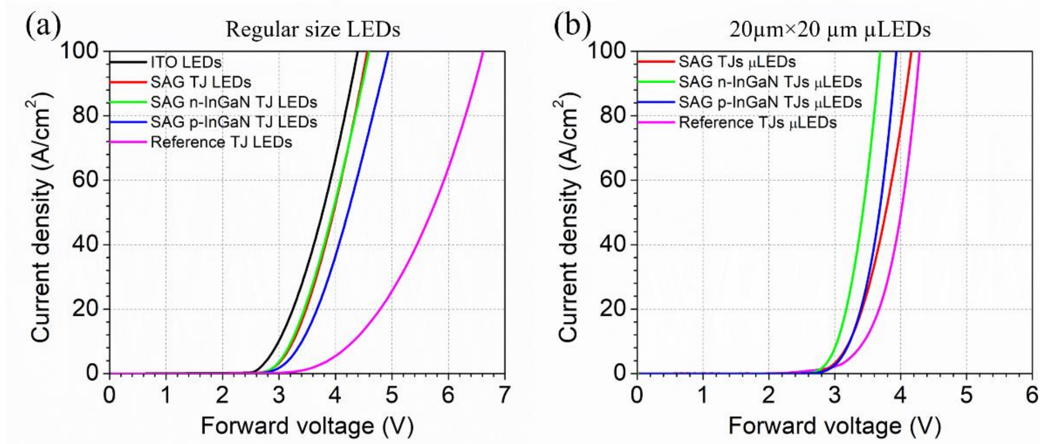

Figures 20(a) J-V curves of SAG TJ LEDs with n-InGaN and p-InGaN insertion layer. ITO LEDs and reference TJ LEDs were plotted for comparison; (b) J-V curves of SAG TJ μLEDs (20×20 μm^2) with n-InGaN and p-InGaN insertion layer.

Differential resistance can be obtained by $\Delta V/\Delta J$ from the J-V curves. Figure 21(a) shows the comparison of the differential resistance as a function of current density for the ITO LEDs and SAG TJ LEDs with regular size. The differential resistance reduces with the injection current for both samples. At 20 A/cm^2, the differential resistance was 2.1×10^{-2} and 3.3×10^{-2} $\Omega\ cm^2$ for the ITO LEDs and SAG TJ LEDs, respectively. The SAG TJ LEDs show a differential resistance smaller than that of the ITO LEDs when the current is larger than 80 A/cm^2. It is worth noting that the differential resistance at 100 A/cm^2 in SAG TJ LEDs was $1.0\times10^{-2}\ \Omega\ cm^2$, which is slightly lower than the ITO LEDs ($1.1\times10^{-2}\ \Omega\ cm^2$). According to Eq. (1), the depletion width reduces with increasing voltage. Therefore, the higher turn on voltage in the TJ LEDs can be understood in this way: the voltage drop at the TJs reduces the depletion width of the TJs to allow for tunneling. Further optimization of the depletion width of the TJs would be a good remedy to reduce the voltage penalty. The output power and the external quantum efficiency (EQE) as a function of the current density of the packaged SAG TJ LEDs and ITO LEDs measured in the integrating sphere are shown in Figure 21(b). At 20 A/cm^2, the output power is improved by 14% from 27 mW of the ITO LEDs to 31 mW of the SAG TJ LEDs. Moreover, the EQE at 20 A/cm^2 is enhanced by 8% from 46% of the ITO LEDs to 54% of the SAG TJ LEDs. Two factors result in the enhanced light output. First, a higher transparency and a lower optical loss is expected in the TJs compared to the ITO contacts. Second, the SAG apertures result in an improvement of LEE, as shown from the simulation results.

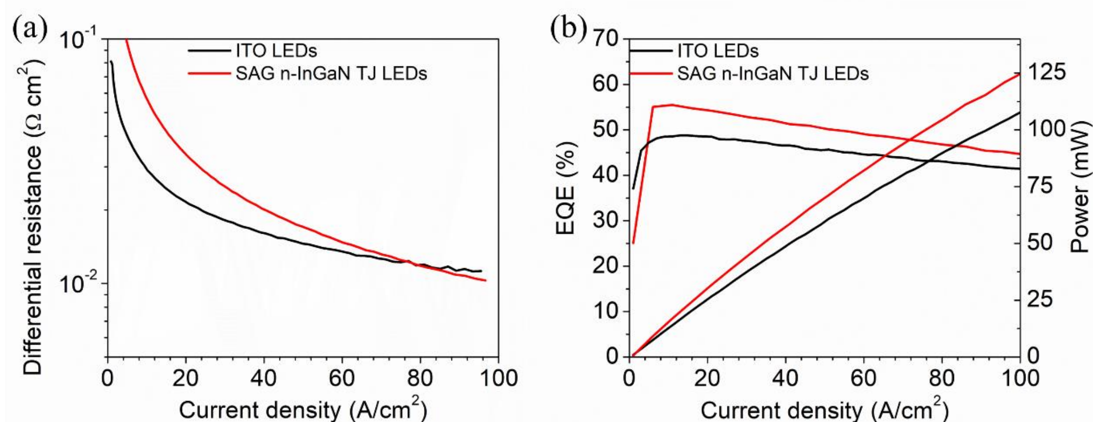

Figures 21 (a) Differential resistance versus current density of ITO LEDs and SAG TJ LEDs; (b) Comparison of EQE and outpour power of ITO LEDs and SAG TJ LEDs.

In summary, we demonstrate the key steps to realize efficient MOCVD-grown TJs. The optimized TJ LEDs and µLEDs show an improved EQE and similar differential resistance compared to the ITO LEDs, followed by a low voltage penalty of around 0.2~0.3 V. Moreover, the TJ LEDs with SAG apertures show a more directional far-field emission accompanied by a slight enhancement of LEE. This work paves the way for the further development of MOCVD-grown TJs and their application such as multiple emission wavelength cascaded µLEDs, AlGaN DUV LEDs, and laser diodes such as TJs buried vertical cavity surface emitting laser.

References

1. Young, E.C., Yonkee, B.P., Wu, F., Oh, S.H., DenBaars, S.P., Nakamura, S. and Speck, J.S., Applied Physics Express, 9, p.022102 (2016).
2. Yonkee, B.P., Young, E.C., DenBaars, S.P., Nakamura, S. and Speck, J.S., Appl. Phys.

Lett., 109, p.191104, 2016.

3. Krishnamoorthy, S., Akyol, F., Park, P.S. and Rajan, S., Appl. Phys. Lett., 102, 113503 (2013).
4. Wernicke, T., Sulmoni, L., Kuhn, C., Tränkle, G., Weyers, M. and Kneissl, M., Group III-Nitride-Based UV Laser Diodes. In Semiconductor Nanophotonics (pp. 505-548). Springer, Cham (2020).
5. Lee, S., Forman, C.A., Lee, C., Kearns, J., Young, E.C., Leonard, J.T., Cohen, D.A., Speck, J.S., Nakamura, S. and DenBaars, S.P., Appl. Phys. Express, 11, 062703 (2018).
6. Yonkee, B.P., Young, E.C., Lee, C., Leonard, J.T., DenBaars, S.P., Speck, J.S. and Nakamura, S., Optics express, 24, 7816 (2016).
7. Ozden, I. and Makarona, E., a. V. Nurmikko, T. Takeuchi, and M. Krames. Appl. Phys. Lett., 79, 2532 (2001).
8. Krishnamoorthy, S., Akyol, F., Park, P.S. and Rajan, S., Appl. Phys. Lett., 102, 113503 (2013).
9. R. King, D. Law, K. Edmondson, C. Fetzer, G. S. Kinsey, H. Yoon, R. Sherif and N. H. Karam, Appl. Phys. Lett., 90, 183516, 2007.
10. K. Boucart and A.-M. Ionescu, Electron Devices, IEEE Transactions on, 54, 1725 (2007).
11. D. Miller, S. Zehr and J. J. Harris, J. Appl. Phys., 53, 744 (1982).
12. S. Okawara, Y. Aoki, M. Kuwabara, Y. Takagi, J. Maeda, and H. Yoshida, Appl. Phys. Express 11, 012701 (2018).
13. M. Diagne, Y. He, H. Zhou, E. Makarona, A. V. Nurmikko, J. Han, K. E. Waldrip, J. J. Figiel, T. Takeuchi, and M. Krames, Appl. Phys. Lett. 79, 3720 (2001).
14. J. T. Leonard, E. C. Young, B. P. Yonkee, D. A. Cohen, T. Margalith, S. P. DenBaars, J. S. Speck, and S. Nakamura, Appl. Phys. Lett. 107, 091105 (2015).
15. A. Forman, S. G. Lee, E. C. Young, J. A. Kearns, D. A. Cohen, J. T. Leonard, T. Margalith, S. P. DenBaars, and S. Nakamura, Appl. Phys. Lett. 112, 111106 (2018).
16. S. G. Lee, C. A. Forman, C. Lee, J. Kearns, E. C. Young, J. T. Leonard, D. A. Cohen, J. S. Speck, S. Nakamura, and S. P. DenBaars, Appl. Phys. Express 11, 062703 (2018).
17. T. Furuta et al., Jpn. J. Appl. Phys. 55, 05FJ11 (2016).
18. K. Matsui, Y. Kozuka, K. Ikeyama1, K. Horikawa, T. Furuta, T. Akagi, T. Takeuchi, S. Kamiyama, M. Iwaya, and I. Akasaki, Jpn. J. Appl. Phys. 55, 05FJ08 (2016).

19. K. Ikeyama et al., Appl. Phys. Express 9, 102101 (2016).
20. T. Takeuchi, S. Kamiyama, M. Iwaya, and I. Akasaki, Rep. Prog. Phys. 82, 012502 (2019).
21. A. I. Alhassan, E. C. Young, A. Y. Alyamani, A. Albadri, S. Nakamura, S. P. DenBaars, and J. S. Speck, Appl. Phys. Express (2018), 11, 042101.
22. M. J. Grundmann, "Polarization-induced tunnel junctions in III-nitrides for optoelectronic applications," PhD Dissertation, University of California, Santa Barbara, 2007.
23. M. Shatalov, J. Yang, Y. Bilenko, M. Shur and R. Gaska, in Lasers and Electro-Optics Pacific Rim (CLEO-PR), 2013 Conference on, 2013.
24. M. J. Grundmann and U. K. Mishra, Phys. Status Solidi C, 4, 2830, 2007.
25. F. Akyol, S. Krishnamoorthy, and S. Rajan, Appl. Phys. Lett. 103, 081107 (2013).
26. Y. Kuwano, M. Kaga, T. Morita, K. Yamashita, K. Yagi, M. Iwaya, T. Takeuchi, S. Kamiyama, and I. Akasaki, Jpn. J. Appl. Phys. 52, 08JK12(2013).
27. C. G. Van de Walle, J. of Appl. Phys. 95, 3851(2004).
28. Y. Kuwano, M. Kaga, T. Morita, K. Yamashita, K. Yagi, M. Iwaya, T. Takeuchi, S. Kamiyama, and I. Akasaki, Jpn. J. Appl. Phys., 52, 08JK12 (2013).
29. D. Hwang, A. J. Mughal, M. S. Wong, A. I. Alhassan, S. Nakamura, and S. P. Denbaars, Appl. Phys. Express 11, 012102 (2018).
30. M. Khoury, H. Li, P Li, Y.C. Chow, B. Bonef, H. Zhang, M.S. Wong, S. Pinna, J. Song, J. Choi, J. S Speck, S. Nakamura, S. P DenBaars, Nano Energy 67, 104236 (2020).
31. H. Li, M. S. Wong, M. Khoury, B. Bonef, H. Zhang, Y. Chow, P. Li, J. Kearns, A. A. Taylor, P. De Mierry, Z. Hassan, S. Nakamura, and S. P. DenBaars, Opt. Express, 27(17), 24154-24160 (2019).
32. S. Krishnamoorthy, F. Akyol, and S. Rajan, Appl. Phys. Lett. 105(14), 141104(2014).
33. P. Li, H. Zhang, H. Li, M. Iza, Y. Yao, M. S. Wong, N. Palmquist, J. S. Speck, S. Nakamura, and S. P. DenBaars, Opt. Express 28, 18707 (2020).
34. A. I. Alhassan, S. P. DenBaars, J. S. Speck, “MOCVD Tunnel Junction Growth in III_Nitride Devices” U.S. Patent Application, US 2019/0245112 A1, Filed Feb 7, 2019.
35. Z. H. Zhang, S. T. Tan, Z. Kyaw, Y. Ji, W. Liu, Z. Ju, N. Hasanov, X. W. Sun, and H. V. Demir, Appl. Phys. Lett., 102, 193508 (2013).
36. S. Neugebauer, M. P. Hoffmann, H. Witte, J. Blasing, A. Dadgar, A. Strittmatter, T. Niermann, M. Narodovitch, and M. Lehmann, Appl. Phys. Lett., 110, 102104 (2017).

37. P. Li, et al., “Metalorganic chemical vapor deposition grown n-InGaN/n-GaN tunnel junctions for micro-light-emitting diodes with very low forward voltage”, Semicond. Sci. Technol. 35 125023（2020）.

38. H. Xing, D. S. Green, H. Yu, T. Mates, P. Kozodoy, S. Keller, S. P. DenBaars, and U. K. Mishra, " Memory effect and redistribution of Mg into sequentially regrown GaN layer by metalorganic chemical vapor deposition", Jpn. J. Appl. Phys., 42, 50(2003).

39. D. Takasuka, Y. Akatsuka, M. Ino, N. Koide, T. Takeuchi, M. Iwaya, S. Kamiyama, and I. Akasaki, " GaInN-based tunnel junctions with graded layers", Appl. Phys. Express 9, 081005(2016).

40. C.L. Keraly, L. Kuritzky, M. Cochet, and C. Weisbuch, Light extraction efficiency part a. ray tracing for light extraction efficiency (LEE) modeling in nitride LEDs. In III-Nitride Based Light Emitting Diodes and Applications (pp. 231-269). Springer, Dordrecht, 2013.

41. P. Zhu, G. Liu, J. Zhang, and N. Tansu, "FDTD analysis on extraction efficiency of GaN light-emitting diodes with microsphere arrays", J. Display Tech., 9, 317(2013).

42. E. Rangel, E. Matioli, Y.-S. Choi, C. Weisbuch, J. S. Speck, and E. L. Hu " Directionality control through selective excitation of low-order guided modes in thin-film InGaN photonic crystal light-emitting diodes", Appl. Phys. Lett. 98, 081104 (2011).

43. Q. Jiao, Z. Chen, Y. Feng, S. Li, S. Jiang, J. Li, Y. Chen, T. Yu, X. Kang, B. Shen, and G. Zhang, "The effects of nanocavity and photonic crystal in InGaN/GaN nanorod LED arrays", Nanoscale Research Lett., 11, 1(2016).

44. A. J. Mughal, E. C. Young, A. I. Alhassan, J. Back, S. Nakamura, J. S. Speck, and S. P. DenBaars, "Polarization-enhanced InGaN/GaN-based hybrid tunnel junction contacts to GaN p–n diodes and InGaN LEDs", Appl. Phys. Express 10, 121006(2017).

45. S. Neugebauer, M. P. Hoffmann, H. Witte, J. Blasing, A. Dadgar, A. Strittmatter, T. Niermann, M. Narodovitch, and M. Lehmann, "All metalorganic chemical vapor phase epitaxy of p/n-GaN tunnel junction for blue light emitting diode applications", Appl. Phys. Lett. 110, 102104(2017).

3. Cascaded Blue LED and Green LEDs

3.1. Challenges of Cascaded LEDs

Recently, the emerging micro-light-emitting diodes (μLEDs) with an area less than 100×100 μm^2 have been causing huge attentions for the next-generation display technology, which can be largely applicated in augmented reality, virtual reality, and large-area display.[1~9] Compared to the common liquid crystal displays and organic LEDs, μLEDs show advantages such as low power consumption, ultra-high resolution, and high thermal stability.[1~4] Moreover, a fast modulation speed over 1 GHz for GaN-based μLEDs was demonstrated in visible light communications system.[5~7] Although high brightness and efficiency blue and green InGaN LEDs have be achieved, GaN-based μLEDs are facing several challenges. First, the efficiency of μLEDs reduces as the area of μLEDs decreases due to nonradiative surface recombination losses and sidewalls damage.[3, 8, 9] Particularly, μLEDs with a size less than 10×10 μm^2 show a very low external quantum efficiency (EQE).[10] Second, the EQE of red μLEDs (~620 nm) remains very poor. The conventional AlGaInP-based red LEDs show a high EQE with a regular size but as the size shrinks to μLEDs scale, the EQE decreases dramatically due to a much higher surface recombination velocity.[11] Meanwhile, the EQE in InGaN red μLEDs remains low, which is caused by quantum-confinement Stark effect (QCSE) and a high defect density in the InGaN quantum wells (QWs) with a high indium composition over 30%.[12] Moreover, it is very challenging to transfer and assemble millions of RGB μLEDs for full colors display application.[13]

Epitaxial tunnel junctions (TJs) have been attractive for GaN-based μLEDs due to a simple fabrication process and the improved performance such as a higher efficiency and a better

current spreading.[14~16] Molecular beam epitaxy (MBE) is the common approach for the overgrowth of TJs, but its scalability is limited for mass production.[14~16] For metalorganic chemical vapor deposition (MOCVD)-grown TJs, the p-type GaN layer would be re-passivated of hydrogen during the overgrowth of n^+GaN TJ layer.[17~20] GaN-based cascaded LEDs with two or three junctions have been reported, which show promising results to circumvent efficiency droop.[21, 22] Nevertheless, the TJs in the cascaded LEDs were grown by MBE and the output power of the cascaded LEDs remains low.

3.2 Cascaded blue and green micro-LEDs with independent junction control

In the following chapters, we demonstrate highly efficient fully MOCVD-grown monolithic cascaded blue/green μLEDs with independent junction control, which could be a promising solution for full color μLEDs display. The blue μLEDs, green μLEDs, and blue/green μLEDs exhibit excellent electrical luminous performance. Details of the growth process, device fabrication, and the optical and electrical properties of the monolithic cascaded blue and green μLEDs were discussed.

Initially, we conducted band diagram simulations using the 1D drift-diffusion formalism, as plotted on Figure 1. As the structure is forward-biased, the tunnel junction between the LEDs becomes reverse-biased. Due to the high level of doping in the junction, reverse-biasing the junction raises the valence band maximum above the conduction band minimum. This means electrons can tunnel from valence band of the *p*- GaN layer into the conduction band of *n*- GaN layer, which causes a hole to form in the p-GaN layer. The holes generated from this process are injected into the blue quantum well region whereas electrons generated goes

into the green quantum well region, allowing for radiative recombination to occur in both regions.

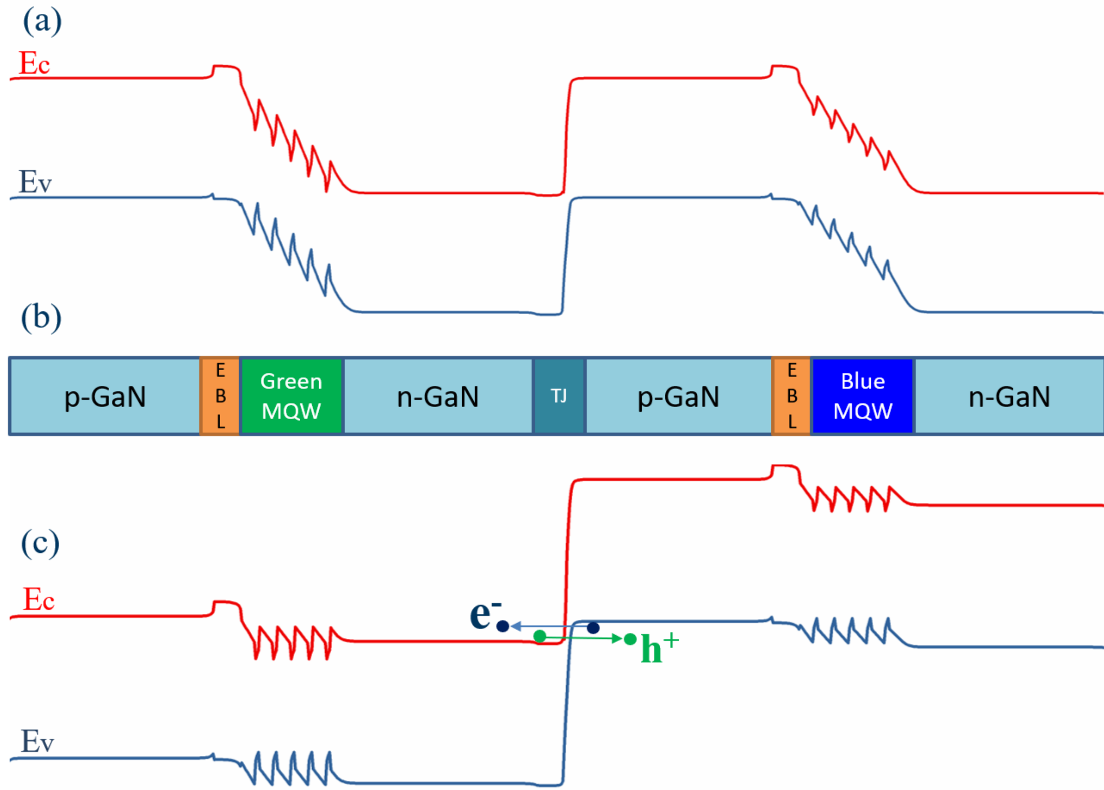

Figs. 1. (a) Band diagram at zero bias, (b) Schematic for the structure, (c) Band diagram at forward bias. The diagram shows the flow of electrons and holes within the structure.

The schematic structure of the cascaded blue/green μLEDs with triple contact pads was shown in Figure 2(a), which were consisted of blue LEDs, TJs and green LEDs. Firstly, n-GaN/n^+GaN/n-InGaN (400 nm/10 nm/2 nm) TJs were grown by MOCVD on standard blue LEDs after a chemical treatment by aqua regia for 5 minutes. Details of the MOCVD-grown TJs conditions can be found in our other reports.[19, 20, 23] Green LEDs were grown on top of the TJs, which were consisted of 1 μm n-GaN, 20 pairs low indium composition InGaN/GaN (2 nm/2 nm) superlattice (SLs), 5 pairs of InGaN/GaN (3 nm/ 9 nm) multiple quantum wells

(MQWs), 20 nm AlGaN electron blocking layer, 120 nm p-GaN and 20 nm p^{+}GaN.[24] The n-GaN mesa of the green and blue μLEDs were exposed by reactive-ion etching (RIE). The p-GaN of blue/green μLEDs were activated by rapid thermal annealing (RTA) at 700 ºC for 30 minutes.[19, 20] A 120 nm thick highly transparent indium-tin-oxide (ITO) was deposited by electron beam for ohmic contact. An omnidirectional reflector (ODR) consisted of silicon dioxide/tantalum pentoxide stacks was deposited by ion beam deposition (IBD). A 25-nm SiO_2 was deposited as sidewall passivation layer by atomic layer deposition (ALD). [4, 8, 19, 20] Al/Ni/Au (500/100/500 nm) were deposited for ohmic contact to n-GaN and contact pads. Figure 2(b) shows the scanning electron microscope (SEM) of the cascaded blue/green μLEDs. The size for the blue μLEDs and green μLEDs is 60×60 μm^2 and 40×40 μm^2, respectively. From Figure 2(b), the blue μLEDs and green μLEDs can be controlled by the top and right pads, and the bottom and right pads, respectively, while blue/green μLEDs can be operated simultaneously through injecting current from bottom and top pads.

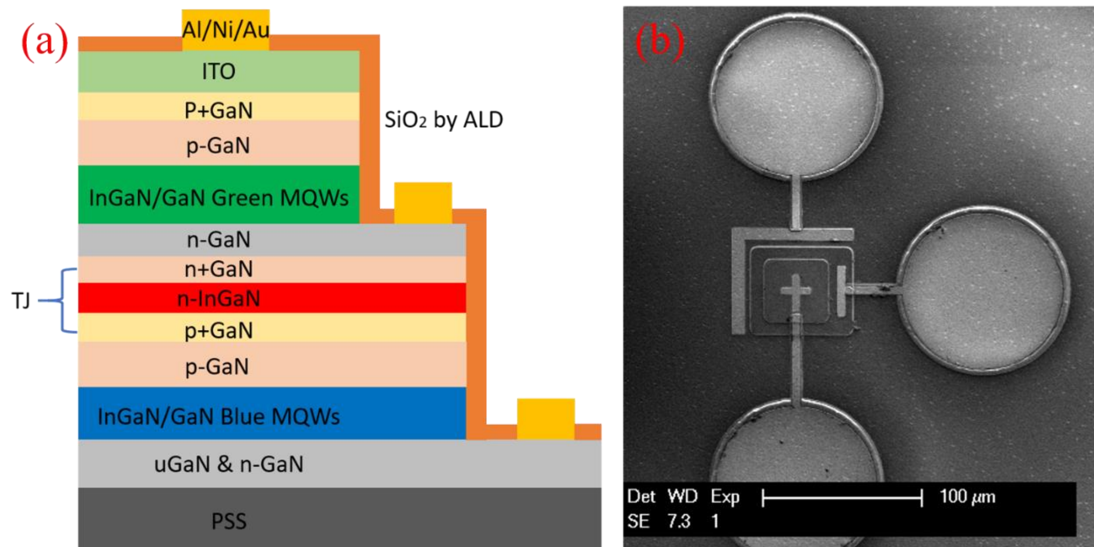

Figs. 2. (a) Schematic structure of the cascaded blue and green μLEDs and (b) SEM image of the cascaded blue and green μLEDs.

Figures 3(a) to 3(c) are the optical luminous images by microscope for the blue μLEDs, green μLEDs and blue/green μLEDs at 3 A/cm^2, which show very uniform blue, green and blue/green emission. The uniform luminous images in the TJ blue μLEDs are ascribed to the improvement of tunneling probability with InGaN insertion layer, as presented in our previous report.[20, 23] The emission spectra were plotted in Figures 3(d) to 3(f), respectively. The emission peaks for the blue μLEDs and green μLEDs are 451 nm and 518 nm, respectively, followed by a full width half maximum (FWHM) of 19 nm and 29 nm. For the operation of cascaded blue/green μLEDs, the emission shows clear two peaks located at the blue and green regions. Therefore, the design enables the realization of cascaded blue/green μLEDs in one device with independent junction control, that is, we can control the blue μLEDs, green μLEDs and blue/green μLEDs independently on the same device by injecting current through different pads.

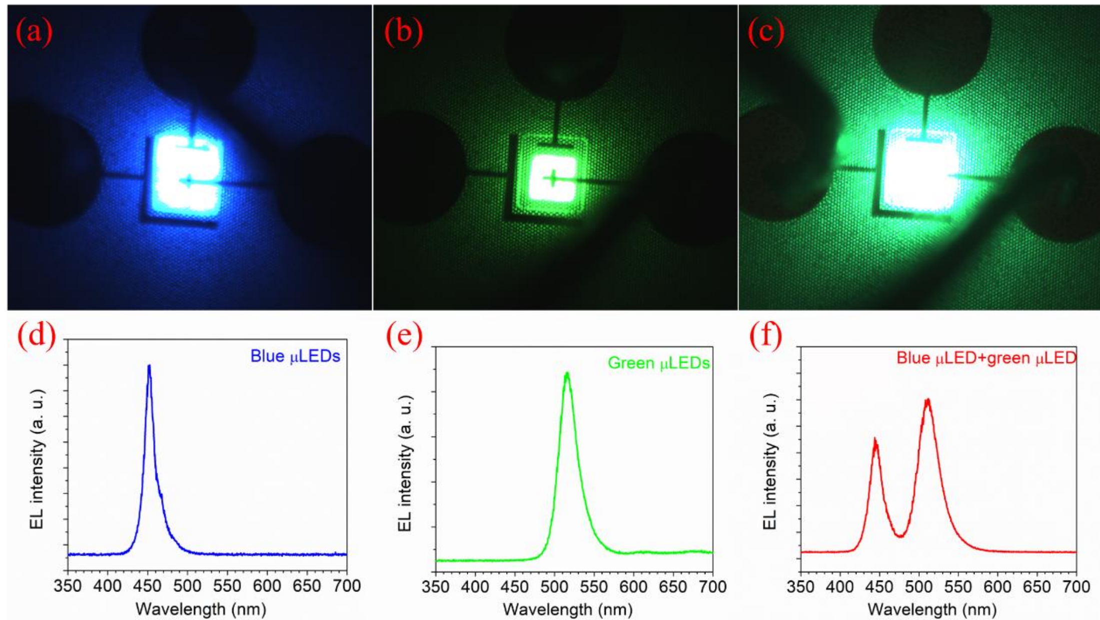

Figs. 3. Electrical luminous microscope images of (a) blue μLEDs, (b) green μLEDs and (c) blue/green μLEDs; Electrical luminous spectra of (d) blue μLEDs, (e) green μLEDs and (f) blue/green μLEDs at 3 A/cm^2.

The current-forward voltage (I-V) characteristics of the blue µLEDs, green µLEDs, and blue/green µLEDs are shown in Figure 4(a). At 20 A/cm^2, the forward voltage (V_f) in TJ blue µLEDs (0.7 mA) and green µLEDs (0.2 mA) is 4.1 V and 3.1 V, respectively. At 0.7 mA, the cascaded blue/green µLEDs is 7.4 V, which equals to the total voltage in TJ blue µLEDs (4.1 V) and green µLEDs (3.3 V). Therefore, both blue and green µLEDs successfully work at the same time. The differential resistance can be obtained by the slope of ΔV/ΔJ. Figure 4(b) shows the differential resistance versus current density for the blue µLEDs, and green µLEDs. At a low current density, the TJ blue µLEDs and green µLEDs show a comparable differential resistance. At a high current density, the differential resistance in green µLEDs is smaller than that in the TJ blue µLEDs. At 100 A/cm^2, the TJ blue µLEDs exhibit a differential resistance of 7×10^{-3} Ω cm^2, which is higher than 4×10^{-3} Ω cm^2 in green µLEDs with ITO contact.[23] This would be caused by the design of metal contact pads.[19, 20] Further optimizations of the contact pads could reduce the differential resistance in the TJ blue µLEDs.

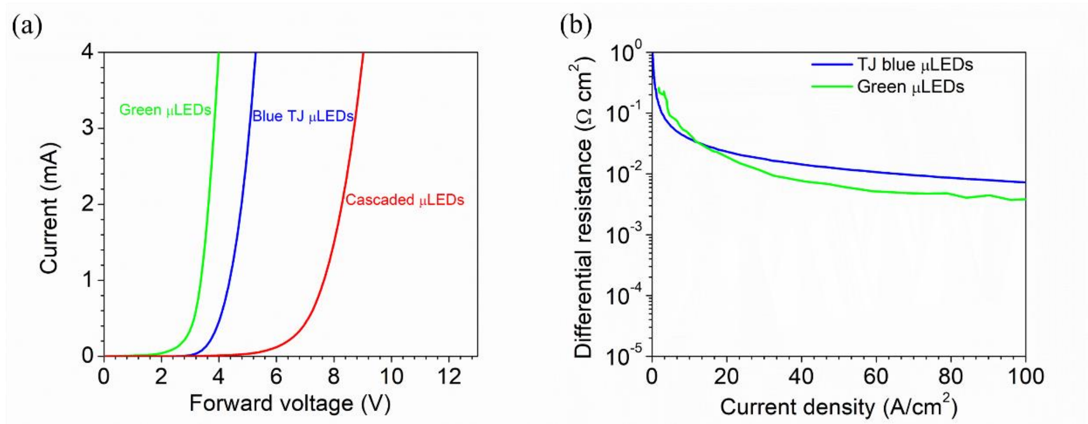

Figs. 4. (a) Current forward voltage (I-V) characteristics of the blue µLEDs, green µLEDs, and blue/green µLEDs; (b) Differential resistance versus current density for blue µLEDs and green µLEDs.

The output power and external quantum efficiency (EQE) versus current densities for the blue μLEDs and green μLEDs were presented in Figure 5(a) and 5(b), respectively. The blue μLEDs and green μLEDs show a peak EQE of 42% and 14%, respectively. The output power increases linearly with the injection current density for both TJ blue μLEDs and green μLEDs. At 200 A/cm^2, the output power for the blue μLEDs and green μLEDs is 2.5 mW and 1.9 mW, respectively. These results clearly point out that the cascaded blue and green μLEDs with independent junction control show excellent optical and electrical properties.

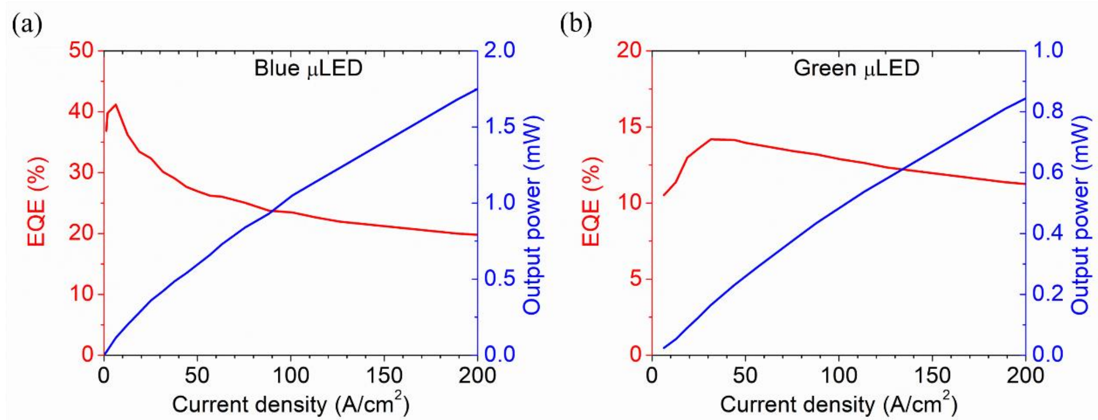

Figs. 5. Output power and EQE versus current density for (a) blue μLEDs and (b) green μLEDs.

In conclusion, we present high performance cascaded blue/green μLEDs with independent junction control utilizing TJ technology. This demonstration provides a promising technology for the realization of single-chip full colors μLEDs with arbitrarily colors mixing by controlling the independent junctions.

3.3 Fully transparent cascaded blue and green micro-light-emitting diodes

We also present fully transparent metal organic chemical vapor deposition (MOCVD)-grown InGaN cascaded micro-light-emitting diodes (μLEDs) with independent junction

control. Cascaded μLEDs consisted by blue μLEDs, tunnel junction (TJ), green μLEDs, and TJ, without using any conductive oxide layer such as indium tin oxide (ITO) or ZnO.[25] We can manipulate the injection of carriers into blue, green, and blue/green junctions in the same device manipulate independently, which show high optical and electrical performance. These results prove the efficient TJs and fully re-activated p-type GaN in the cascaded μLEDs. Such demonstration shows the important application of TJs for the integration of μLEDs with multiple color emissions.

Firstly, band diagram of the fully cascaded TJs InGaN LEDs was investigated. Figures 6 show the simulated band diagram of the cascaded InGaN LEDs consisted by blue LEDs, TJ, green LEDs, and TJ under zero bias and forward bias conditions using the 1D drift-diffusion formalism. Under a forward bias, the two TJs between blue and green LED and between green LED and top contact will be reversed-biased. Since both junctions are highly doped, the valence band maximum of the respective p-GaN will be raised above the conduction band minimum of the respective n-GaN layer. Electrons can tunnel from the valence band of the p-GaN layer to the conduction band of the n-GaN layer through band-to-band tunneling. [26,27] Meanwhile, holes created by the same process are injected to the active region under electric field and recombine with electrons transport from the other TJ, which efficiently assist the radiative recombination process in both LEDs. Therefore, this design theoretically enables the cascaded InGaN LEDs with independent junction control.

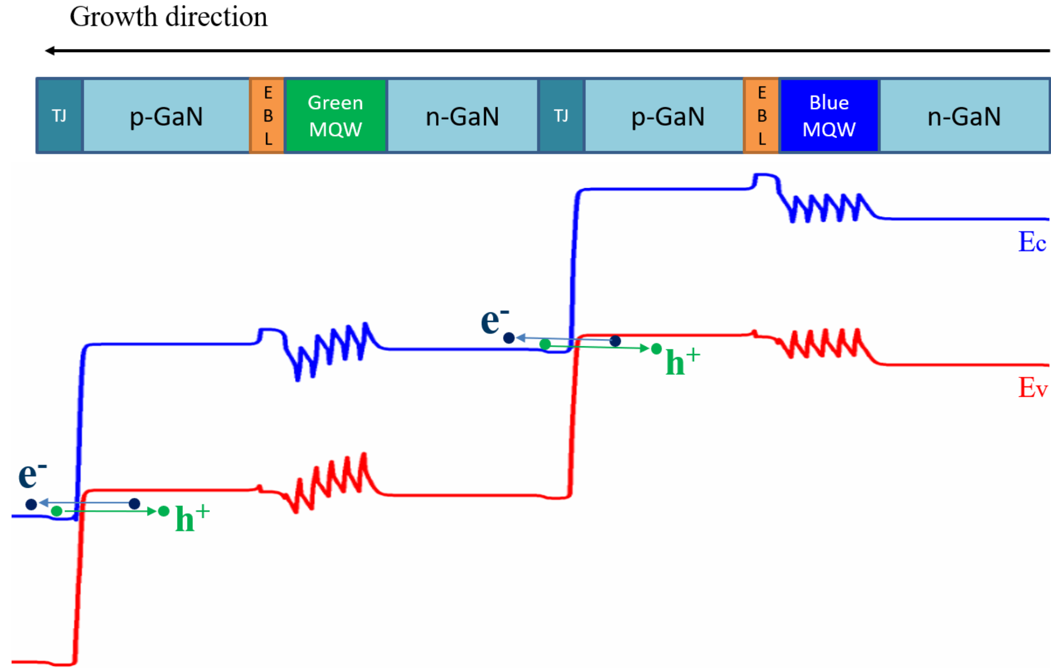

Figs. 6. Schematic structure for the cascaded LEDs with TJs on top and band diagram at forward bias of 7 V. The band diagram shows the flow of electrons and holes in the TJs.

The cross-sectional schematic structure of the cascaded blue/green μLEDs with individual contacts was shown in Figure 7(a). Standard blue LEDs were carried out with chemical treatment and loaded into MOCVD reactor for the overgrowth of TJs and green LEDs immediately. The TJs were consisted by n-InGaN/n^+GaN/n-GaN with a thickness of 2 nm/10 nm/380 nm. The Si doping concentration in the n^+GaN is 1.7×10^{21} cm^{-3}. Details about TJs growth conditions can be seen in our previous publication.[19,20~23] The green LEDs were consisted of 1 μm n-type GaN, 30 pairs $In_{0.06}Ga_{0.94}N$/GaN (3 nm/6 nm) superlattice (SLs), 5 pairs of InGaN/AlGaN/GaN (3 nm/2 nm/9 nm) multiple quantum wells (MQWs), 20 nm p-type AlGaN electron blocking layer (EBL), a 120 nm p-type GaN and a 20 nm heavily doped p^+GaN.[24] Cascaded LEDs were taken out of the MOCVD reactor, following by a similar chemical treatment and TJ was grown on top of the green LEDs. The n-type GaN of the green LEDs and blue LEDs was exposed by the reactive ion etching with a depth of 1 μm and 1.8

μm, respectively. The p-type GaN of blue and green LEDs were re-activated by rapid thermal annealing (RTA) at 700 ºC for 30 minutes to remove the hydrogen in the p-type region through sidewalls.[19~20,23,28] Thanks to the small mesa size, the p-GaN could be fully re-activated. 5 pairs of SiO_2 and Ta_2O_5 stack with 20 nm Al_2O_3 on top were deposited by ion beam deposition as sidewall insulation layer. A 25-nm SiO_2 layer was deposited as sidewall passivation layer by atomic layer deposition.[4,6, 19~20,30] Al/Ni/Au (500 nm /100 nm /500 nm) were evaporated as ohmic contact to n-type GaN and contact pads. Figure 7(b) shows the scanning electron microscope (SEM) of the fabricated cascaded μLEDs. The cross-finger metals work as ohmic contact layer for the n-type GaN layer of green μLEDs and the TJs of blue μLEDs. The cross-finger contact layer was embedded into the mesa of green μLEDs, which can enlarge the exposed sidewall areas of the green μLEDs and improve the p-GaN re-activation efficiency.[29] Also, it can improve current spreading for the blue μLEDs with more uniform current injection. Although it would introduce more sidewall damage for the green μLEDs, chemical treatment such as KOH or H_3PO_4 could be carried out to recovery the sidewall damage as shown by Wong et al. in Ref. 20.

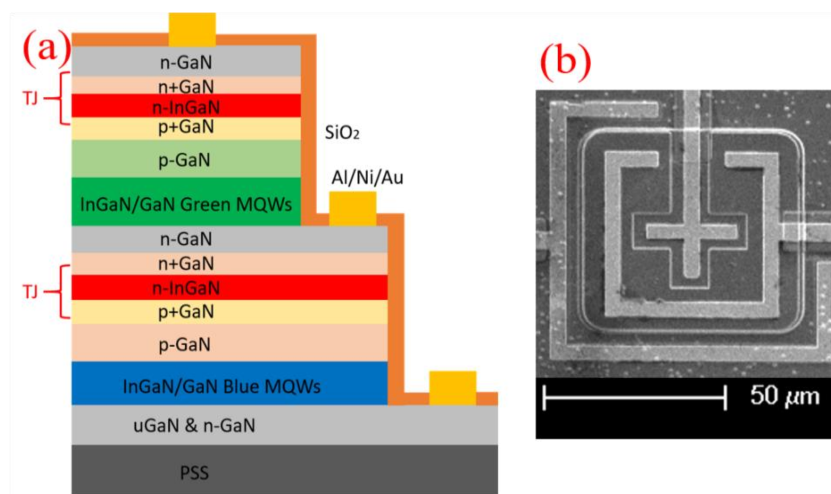

Figs. 7. (a) Detailed schematic structure of the full cascaded TJs blue and green μLEDs and (b) SEM image of the fabricated cascaded μLEDs.

Figures 8(a) to 8(c) show the emission spectra of the blue μLEDs, green μLEDs and blue/green μLEDs at an injection current of ~0.4 mA. The inset shows the individual electrical luminous images for the same device took from microscope, and we can see uniform luminous images in the TJ blue μLEDs, TJ green μLEDs, and blue/green μLEDs, proving that the TJs are efficient and p-GaN has been re-activated. The emission peak wavelength for the TJ blue μLEDs and TJ green μLEDs is 455 nm and 508 nm, respectively, followed by a full-width half maximum (FWHM) of 18 nm and 33 nm. A very weak green shallow emission appears in the spectrum of the TJ blue μLEDs, which is caused by the excitation of the green MQWs by the blue light. Since the green emission peak is so weak that it would not affect the blue emission from the bottom blue μLEDs. Another consideration for growing green μLEDs on top is that the growth temperature of green MQWs is much lower than that of blue MQWs. For the cascaded blue/green LEDs, two emission peaks located at 445 nm and 507 nm were observed. Therefore, we can realize TJ blue μLEDs, TJ green μLEDs and blue/green μLEDs in the same devices by injecting the current through different contact pads.

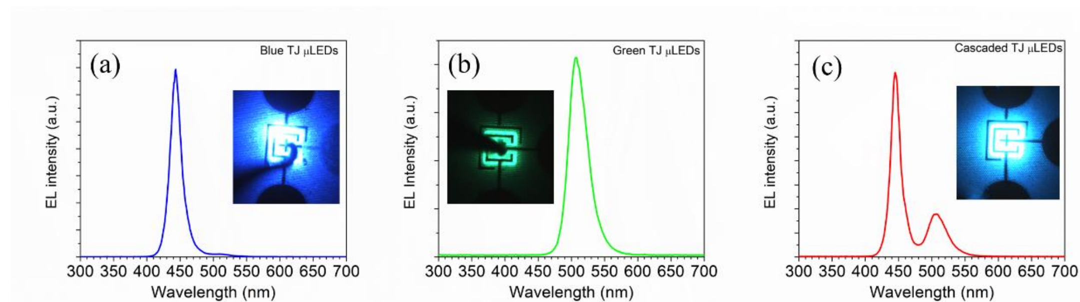

Figs. 8. Electrical luminous spectrum for (a) TJ blue μLEDs, (b) TJ green μLEDs, and (c) blue/green μLEDs. The insets show the electrical luminous microscope images of blue μLEDs, green μLEDs and blue/green μLEDs, respectively.

The emission spectra of the cascaded TJ blue/green μLEDs at various injection current from 0.3 to 3 mA is shown in Figure 9(a). Two clear emission peaks located in blue and green region appear when the current is higher than 0.3 mA. The extracted blue and green peaks wavelength versus injection current were plotted in Figure 9(b). Both emission peaks show blue shift. The blue peak decreases from 447 nm to 443 nm, and the green peak reduces form the 513 nm to 502 nm as the current increases from 0.3 to 1 mA. The wavelength blue-shift is typically observed in the c-plane InGaN LEDs, which is due to carriers filling higher energy localized states. The integrated intensity ratio of the blue and green peaks (I_{blue}/I_{green}) versus current was also plotted in Figure 9(b), which increases from 0.03 to 0.5 with increasing current from 0.3 to 1 mA. The injected carriers were firstly captured in the blue active region at a small current. As the current increases, more carriers were radiatively recombined in the green active region. Such carrier dynamic behavior in the cascaded TJ μLEDs maybe caused by the non-radiative recombination paths related to the more sidewall damage in TJ green μLEDs. Further studies would be carried out to understand the carrier recombination process, especially for the sidewall recovered treatment.[31]

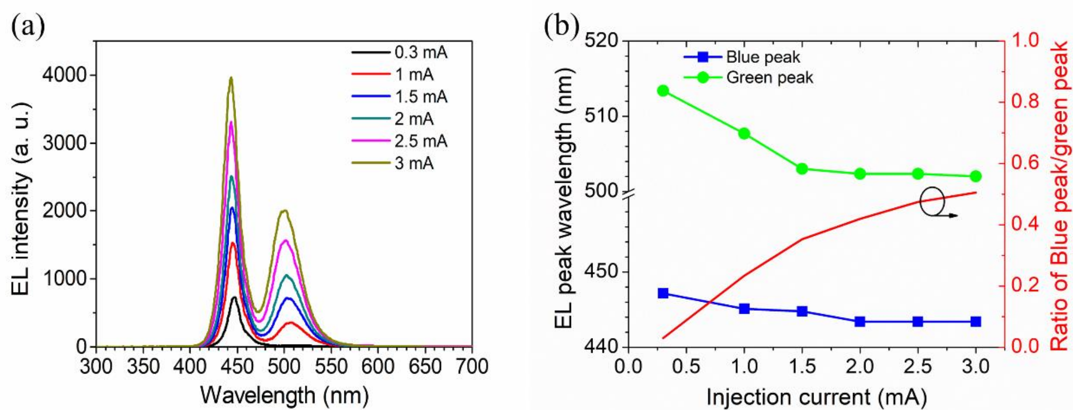

Figs. 9. (a) Electrical luminous spectra at various injection current for blue/green μLEDs and (b) The extracted blue peak, green peak, and intensity ratio of blue/green peak at various injection current.

The current-forward voltage (I-V) curves of the blue μLEDs, green μLEDs, and blue/green μLEDs are shown in Figure 10(a). At 1 mA, the forward voltage (V_f) in TJ blue μLEDs and TJ green μLEDs is 4.20 V and 3.48 V, respectively. The V_f of the cascaded blue/green μLEDs is 7.62 V at 1 mA, which is slightly smaller than the total voltage in TJ blue μLEDs and TJ green μLEDs. At a current density of 20 A/cm^2, the V_f for the TJ μLEDs (60×60 μm^2) and TJ green μLEDs (~45×45 μm^2) is 4.06 V and 3.13 V, indicating efficient TJs and a p-type GaN re-activation efficiency. The lower V_f in the TJ green μLEDs can be understood by the enlarged sidewalls areas shown in Fig. 7(b), which provide the visible paths for the out diffusion of hydrogen during RTA. The output power versus injection current for the blue μLEDs, green μLEDs and blue/green μLEDs was shown in Figure 10(b). The output power increases linearly with the injection current for the three LEDs. At 4 mA, the output power of the blue μLEDs, green μLEDs, and blue/green μLEDs is 0.89 mW, 0.43 mW and 1.41 mW, respectively. Those optical and electrical properties of the cascaded TJ μLEDs indicate that the width of the depletion region in the TJs were thin enough and the p-GaN layers were fully re-activated. Therefore, we can manipulate the injection of carriers into blue, green, and blue/green active regions independently, showing promising potentials for the integration of multiple μLEDs.

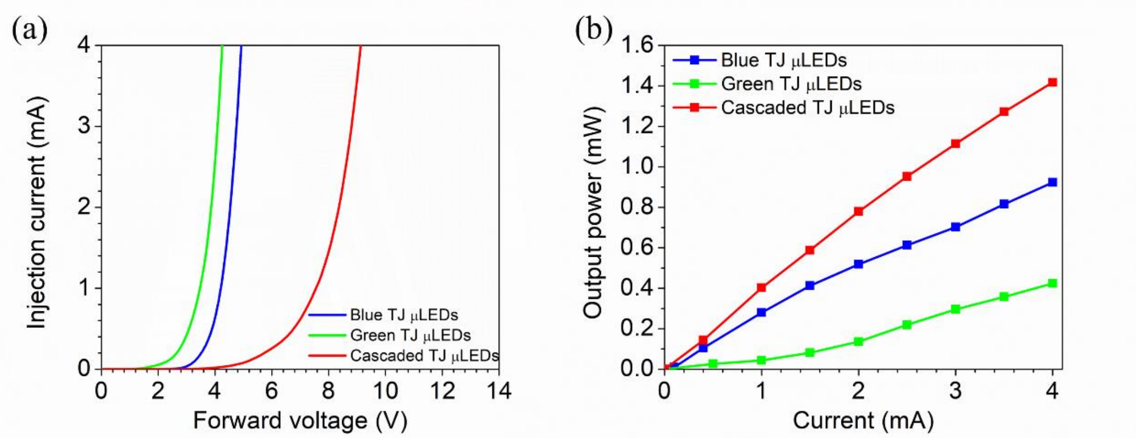

Figs. 10. (a) I-V characteristics and (b) Output power versus current curves for TJ blue μLEDs, TJ green μLEDs, and blue/green μLEDs.

In conclusion, we present high performance cascaded blue/green μLEDs with independent junction control utilizing MOCVD-grown TJ. This demonstration provides promising application of TJs for cascaded μLEDs.

References

1. J. Day, J. Li, D. Y. C. Lie, C. Bradford, J. Y. Lin, and H. X. Jiang, Appl. Phys. Lett. 99, 031116 (2011).
2. M. S. Wong, S. Nakamura, and S. P. DenBaars, ECS J. Solid State Sci. Technol. 9, 015012 (2020).
3. D. Hwang, A. J. Mughal, M. S. Wong, A. I. Alhassan, S. Nakamura, and S. P. Denbaars, Appl. Phys. Express 11, 012102 (2018).
4. H. Li, M. S. Wong, M. Khoury, B. Bonef, H. Zhang, Y. Chow, P. Li, J. Kearns, A. A. Taylor, P. De Mierry, Z. Hassan, S. Nakamura, and S. P. DenBaars, Opt. Express, 27, 24154 (2019).
5. H. Zhang, P. Li, H. Li, J. Song, S. Nakamura, S.P. DenBaars, Appl. Phys. Lett., 117, 181105 (2020).
6. M. Khoury, H. Li, P Li, Y.C. Chow, B. Bonef, H. Zhang, M.S. Wong, S. Pinna, J. Song, J. Choi, J. S Speck, S. Nakamura, S. P DenBaars, Nano Energy 67, 104236 (2020).
7. A. Rashidi, M. Monavarian, A. Aragon, A. Rishinaramangalam, and D. Feezell, IEEE Electron Dev. Lett., 39, 520 (2018).
8. M. S. Wong, D. Hwang, A. I. Alhassan, C. Lee, R. Ley, S. Nakamura, and S. P. DenBaars, Opt. Express 26, 21324 (2018).
9. F. Olivier, S. Tirano, L. Dupré, B. Aventurier, C. Largeron, and F. Templier, J. Lumin.,191, 112-116 (2017).
10. J. M. Smith, R. Ley, M. S. Wong, Y. H. Baek, J. H. Kang, C. H. Kim, M. J. Gordon, S. Nakamura, J. S. Speck, and S. P. Denbaars, Appl. Phys. Lett. 116, 071102 (2020).

11. M.S. Wong, J.A. Kearns, C. Lee, J.M. Smith, C, Lynsky, G. Lheureux, H. Choi, J. Kim, C. Kim, S. Nakamura, J.S. Speck, S.P. DenBaars. Opt. Express, 28, 5787(2020).
12. J.I. Hwang, R. Hashimoto, S. Saito, and S. Nunoue, Appl. Phys. Express, 7, 071003 (2014).
13. X. Zhou, P. Tian, C.W. Sher, J. Wu, H. Liu, R. Liu, and H.C. Kuo, Progress in Quantum Electron., 71, 100263(2020).
14. E. C., Young, B. P. Yonkee, F. Wu, S. H. Oh, S. P. DenBaars, S. Nakamura, and J. S. Speck, Appl. Phys. Express, 9, 022102 (2016).
15. B. P. Yonkee, E. C. Young, S. P. DenBaars, S. Nakamura, and J. S. Speck, Appl. Phys. Lett., 109, 191104 (2016).
16. S. Krishnamoorthy, P. S. Park, and S. Rajan, Appl. Phys. Lett. 99, 233504 (2011).
17. Y. Kuwano, M. Kaga, T. Morita, K. Yamashita, K. Yagi, M. Iwaya, T. Takeuchi, S. Kamiyama, and I. Akasaki, Jpn. J. Appl. Phys., 52, 08JK12 (2013).
18. D. Hwang, A. J. Mughal, M. S. Wong, A. I. Alhassan, S. Nakamura, and S. P. DenBaars, Appl. Phys. Express, 11, 012102 (2018).
19. P. Li, H. Zhang, H. Li, M. Iza, Y. Yao, M. S. Wong, N. Palmquist, J. S. Speck, S. Nakamura, and S. P. DenBaars, Opt. Express 28, 18707 (2020).
20. P. Li, H. Zhang, H. Li, Y. Zhang, Y. Yao, N. Palmquist, M. Iza, J. S Speck, S.Nakamura, S.P DenBaars, Semicond. Sci. Technol. 35 125023 (2020).
21. F. Akyol, S. Krishnamoorthy, and S. Rajan, Appl. Phys. Lett., 103, 081107 (2013).
22. F. Akyol, S. Krishnamoorthy, Y. Zhang, and S. Rajan, Appl. Phys. Express, 8, 082103(2015).
23. P. Li, H. Li, H. Zhang, M. Iza, J. S. Speck, S. Nakamura, and S. P. DenBaars, Semicond. Sci. Technol., 36, 035019 (2021).
24. A. I. Alhassan, R. M. Farrell, B. Saifaddin, A. Mughal, F. Wu, S. P. DenBaars, S. Nakamura, and J. S. Speck, Opt. Express 24, 17868 (2016).
25. S. Lee, C.A. Forman, C. Lee, J. Kearns, E.C. Young, J.T. Leonard, D.A. Cohen, J.S. Speck, S. Nakamura, and S.P. DenBaars, Appl. Phys. Express, 11, 062703 (2018).
26. L. Esaki, Physical Review, 109, 603 (1958).
27. S.J. Chang, W.H. Lin, W.S. Chen. IEEE J. Quantum Electronics, 51,1 (2015).
28. C. G. Van de Walle, J. Appl. Phys., 95, 3851 (2004).
29. D. Takasuka, Y. Akatsuka, M. Ino1, N. Koide, T. Takeuchi, M. Iwaya, S. Kamiyama, and

I. Akasaki, Appl. Phys. Express, 9, 081005 (2016).

30. J. J. Wierer Jr., and N. Tansu, Laser & Photonics Rev., 13, 1900141 (2019).
31. M. S. Wong, C. Lee, D. J. Myers, D. Hwang, J. A. Kearns, T. Li, J. S. Speck, S. Nakamura, and S. P. DenBaars, Appl. Phys. Express, 12, 097004 (2019).

4. InGaN based red micro-LEDs

4.1 Size-independent peak EQE of InGaN red μLEDs

Micro-light-emitting diodes (μLEDs) displays have been considered as the next generation display technology due to the higher resolution, high contrast ratio, longer lifetime and lower power consumption compared to the traditional display, such as liquid crystal display (LCD) and organic light-emitting diodes (OLEDs). μLEDs can be widely applied in wearable devices, ultra-large and very small display screen, augmented reality, virtual reality, and visible light communication.[1~6] In micro-LEDs display, each die becomes pixel, which are operated at a low current density of ~2 A/cm^2 from displays and a slightly higher current density (<30 A/cm^2) for micro-displays.[2] Among the many challenges of μLEDs display technology, red μLEDs (~620 nm) is a major area of research focus now.[7, 8] The two kinds of compound semiconductor materials system that can generate red light are AlInGaP and InGaN.[7~14] On one hand, although AlInGaP red LEDs have shown a high external quantum efficiency (EQE) for a regular die size of 0.1 mm^2, these devices exhibit a significant reduction in EQE by decreasing the size to μLEDs scale (<100×100 μm^2).[7~10] This reduction has largely been attributed to the high surface recombination velocity of AlInGaP μLEDs (~10^5 cm/s) as compared to that of InGaN μLEDs (~10^4 cm/s).[8, 10~11] Therefore, AlInGaP μLEDs suffer from a much larger Shockley-Read-Hall (SRH) nonradiative recombination induced by sidewall damage, leading to the reduction of EQE for small size devices.[7~8] On the other hand, the EQE of InGaN-based red μLEDs remains low due to the strong quantum-confinement Stark effect (QCSE) in the InGaN quantum wells (QWs) with a very high indium composition.[12~14] The large lattice mismatch in the InGaN red QWs results in a large piezoelectric field and then

reduces the electron and hole wavefunction overlap and the internal quantum efficiency. Therefore, the EQE of InGaN-based red μLEDs remains low.

There have been several reports about the performance improvement of InGaN red μLEDs.[12~18] Hwang *et al.* used $Al_{0.90}Ga_{0.10}N$ cap layer on top of the InGaN QWs to enhance the efficiency of InGaN red LEDs.[14] Zhang *et al.* shown high efficiency normal size InGaN orange/red LEDs grown on a silicon substrate using three dimensional "V-pits" injection.[15] Iida *et al.* presented low forward voltage InGaN red LEDs by combing blue and red QWs in the active region or thick underlying GaN layers to reduce in-plane residual stress.[16, 17] However, there are only a few studies on the InGaN red μLEDs with a size less than 100×100 μm^2.[18~20] The common GaN-based LEDs process would result in a decrease of EQE with reducing size, making efficient InGaN red μLEDs more challenging. Pasayat *et al.* demonstrated 632 nn InGaN red μLEDs with a size less than 10×10 μm^2 using strained relaxed porous GaN template. However, the on wafer EQE was ~0.2%.[18] Dussaigne *et al.* presented 50×50 μm^2 InGaN red μLEDs grown on InGaN pseudo-substrate bonding on sapphire with an EQE less than 0.1%.[19] Therefore, the realization of high efficiency InGaN red μLEDs with a small size remains highly desired.

In this work, we demonstrate size-independent EQE of InGaN red μLEDs with emission wavelength over 600 nm. The 611 nm InGaN red μLEDs show a peak EQE of 2.4% to 2.6%, even for the device size of 20×20 μm^2.

The InGaN red LEDs were grown on (001) patterned sapphire substrate (PSS) using atmospheric pressure metal organic chemical vapor deposition (MOCVD). Trimethylgallium (TMGa), triethylgallium (TEGa), trimethylaluminium (TMAl), trimethylindium (TMIn),

bicyclopentadienyl (Cp_2Mg), disilane (Si_2H_6), and ammonia (NH_3) sources were used as precursors and dopants. Fig. 1(a) shows the schematic epitaxial structure, which consists of a 3-μm unintentionally doped (UID) GaN, a 3-μm n-type GaN with a Si concentration of 6×10^{18} cm^{-3}, a 30 pair $In_{0.06}Ga_{0.94}N$/GaN (3 nm/6 nm) superlattices (SLs), a 6 pair InGaN red QWs/AlGaN cap layers/GaN barriers (3 nm/2 nm/9 nm), a 20 nm p-type AlGaN electron blocking layer (EBL), a 120 nm p-type GaN with Mg concentration of $\sim1\times10^{20}$ cm^{-3}, and a 20 nm heavily Mg-doped p^+GaN contact layer ($\sim10^{21}$ cm^{-3}). The advantage of incorporating an AlGaN cap layer on InGaN green QWs can be found in the previous reports from our group.[21, 22] For these devices, the indium composition in the QWs is expected to be higher than 35% for the emission wavelength over 600 nm. The epitaxial wafer shows a roughness of 0.3 nm on a 5×5 μm^2 area scanned by atomic force microscope (AFM), indicating a smooth layer. Square μLEDs with a length ranging from 20 to 100 μm were fabricated.[4~7] A110-nm indium-tin oxide (ITO) was deposited as a transparent and ohmic contact layer. Reactive-ion etching (RIE) was used to etch the mesa using $SiCl_4$. An omnidirectional reflector (ODR) consisting of SiO_2 and Ta_2O_5 with a 60 nm Al_2O_3 cap was deposited using ion beam deposition (IBD). A 25 nm SiO_2 layer was deposited by atomic-layer deposition (ALD) for sidewall passivation. Metals contact pads of Al/Ni/Au (500 nm /100 nm /500 nm) were deposited. Fig. 1(b) is the scanning electron microscope (SEM) image of the fabricated 60×60 μm^2 μLED, showing the mesa, ODR and metals contact clearly. Finally, the μLEDs were diced, and the singulation die was mounted on silver header, bonded with gold wire, encapsulated with silicone, and measured in an integrating sphere.

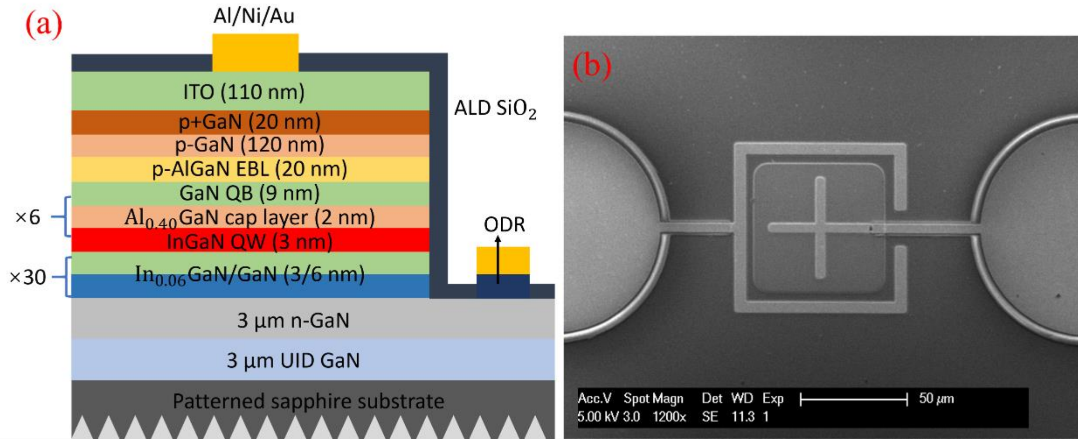

FIG. 1. (a) Schematic epitaxial structure of InGaN red µLEDs; (b) SEM of the fabricated 60×60 µm^2 µLEDs.

Fig. 2 shows the optical microscopy images of the InGaN µLEDs at a current density ~3 A/cm^2. All the µLEDs with different sizes demonstrate uniform red electroluminescence (EL). Even for the size down to 20×20 µm^2, red emission is clearly observed, indicating a uniform current injection and a minimization of sidewall damage. Also, we can see the emission reflected from the patterned sapphire from the images.

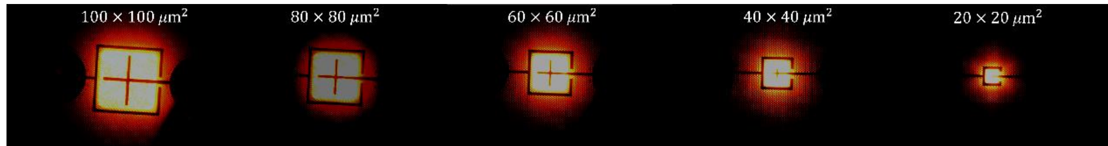

FIG. 2. Microscope EL images of InGaN red µLEDs with a size varied from 100×100 to 20×20 µm^2.

The current density-forward voltage (J-V) characteristics of the InGaN µLEDs with different sizes are plotted in Fig. 3(a). For the µLEDs from 40×40 µm^2 to 100×100 µm^2, the J-V curves are similar with a forward voltage (V_f) of 3.7 V at 20 A/cm^2. The 20×20 µm^2 µLEDs exhibit a lower forward voltage and the V_f at 20 A/cm^2 is 3.5 V, which may be caused by an improved current spreading in the very small size device. The output power-current (P_o-I) characteristics for the 100×100 µm^2, 60×60 µm^2, and 20×20 µm^2 InGaN µLEDs are shown

in Fig. 3(b). The output power was collected by an integrating sphere. All three µLEDs show a linear increase of the output power with increasing injection current. It is worth noting that the three P_o-I curves are well overlapped at low injection current, suggesting that the output power does not degrade for small size InGaN µLEDs. The output power for 100×100 μm^2 µLEDs was 0.83 mW at 20 mA. The EL spectrum at 20 A/cm^2 is shown in Fig. 3(c). The peak wavelength is 611 nm and the full-width half maximum (FWHM) is 48 nm, which is typically observed for InGaN LEDs with such long emission.[13, 16, 19] There are no additional short peak in the EL spectrum, suggesting good uniform of the InGaN red QWs and no carrier injection into the SLs.[16] Moreover, the peak emission wavelength versus injection current density was presented in Fig. 3(d). The peak wavelength decreases from 611 nm to 588 nm as the current density increases from 3 to 200 A/cm^2. At a high injection current density, carriers start filling the higher energy localized states.[23] Also, polarization-related electric field would be screened, resulting in the large blue-shift in peak wavelength.[23, 24] The large blue-shift in peak wavelength of InGaN µLEDs becomes challenging for micro-LEDs display application.

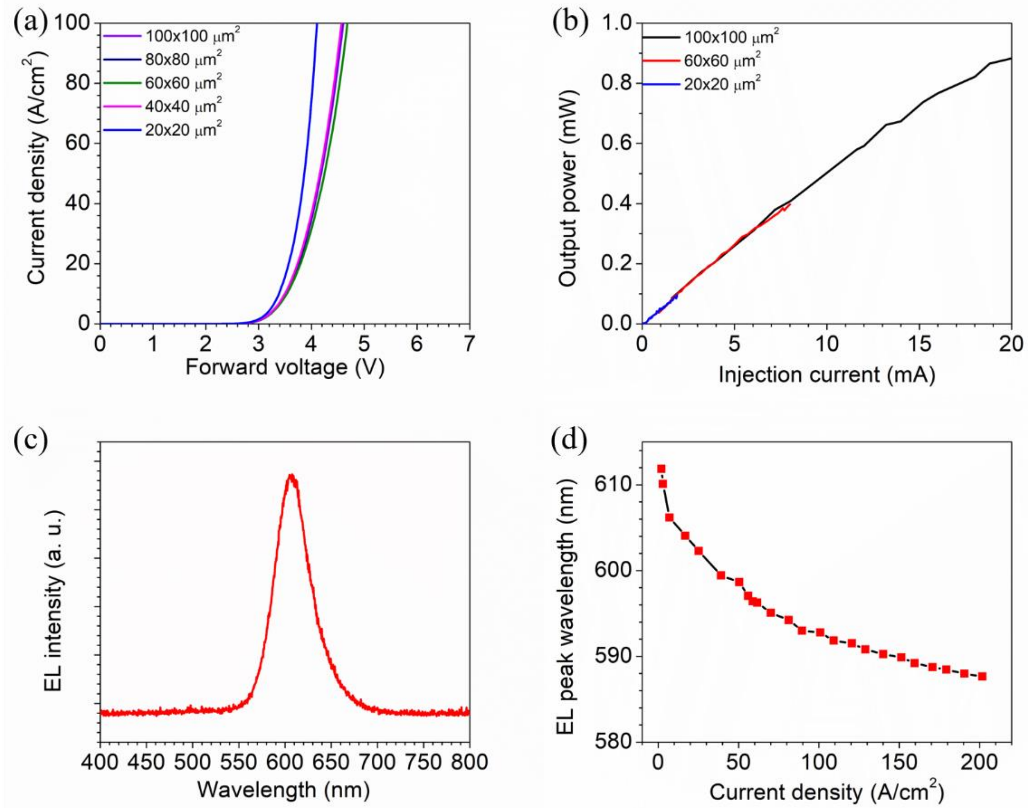

FIG. 3. (a) Current density-forward voltage curves of InGaN μLEDs with sizes varied from 100×100 to 20×20 μm^2; (b) Output power-injection current curves for 100×100, 60×60, and 20×20 μm^2 μLEDs; (c) Emission spectrum of the InGaN μLEDs at 3 A/cm^2; (d) Peak emission wavelength versus current density.

Fig. 4(a) shows the packaged μLEDs with silicon cap layer, which can improve the light extraction efficiency due to a lower refractive index around 1.5 compared to ~2.3-2.4 for GaN. Fig. 4(b) is the luminous image of the packaged μLEDs under a small current density of 2 A/cm^2, showing a clear red emission. The dependence of EQE on current density measured from the integrating sphere for all sizes μLEDs is plotted in Fig. 4(c). The peak EQE is ~2.6% for 80×80 μm^2 and 100×100 μm^2 μLEDs at 10 to 20 A/cm^2. As the sizes decreases to 20×20 μm^2, the EQE maintains as high as 2.4%. All sizes InGaN red μLEDs show similar EQE versus J curves, which suggests that there is no obvious degradation of EQE for the smaller

die area until 20×20 μm^2. At 100 A/cm^2, the EQE varies from 2.3% to 2.5% for the InGaN μLEDs ranged from 20×20 μm^2 and 100×100 μm^2.

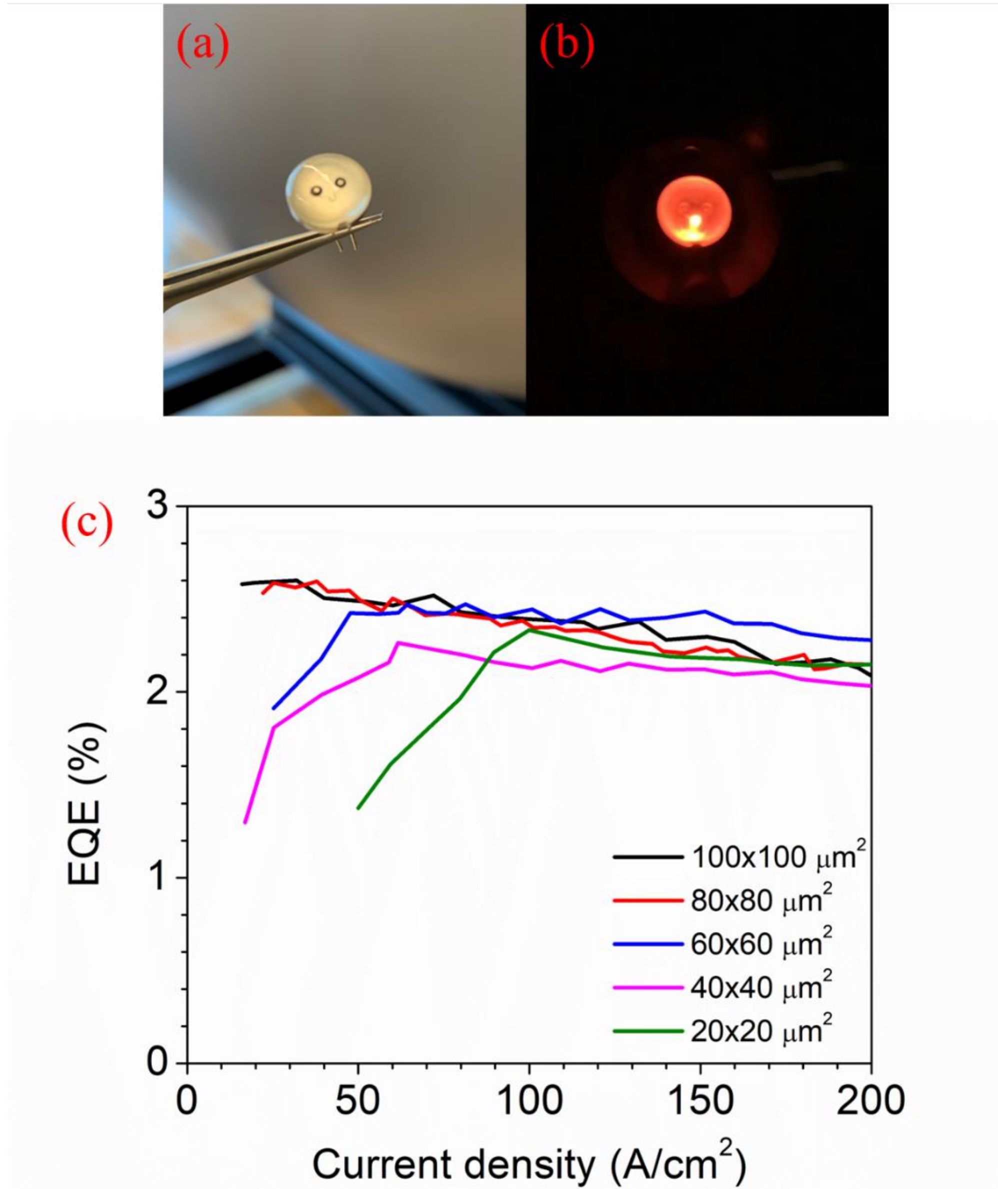

FIG. 4. Images of the packaged InGaN μLEDs (a) without and (b) with injection current; (c) EQE versus current density of the InGaN red μLEDs with sizes from 100×100 to 20×20 μm^2.

Finally, a comparison of normalized peak EQE at different lengths of square AlInGaP and InGaN red μLEDs is shown in Fig. 5. The fabrication process of the AlInGaP red μLEDs is

the same as the InGaN red μLEDs, which can be seen in Ref. 7 from our group. As the die size decreases to 20×20 μm^2, the normalized peak EQE of AlInGaP red μLEDs decreases to be only 43% of the EQE of AlInGaP red μLEDs with a die area of 100×100 μm^2. Similar phenomenon has been reported in other studies.[7, 8] This is caused by the SRH carrier injection loss due to a higher surface recombination velocity of AlInGaP, which is related to the fundamental property of the materials and difficult to overcome. In contrast, InGaN red μLEDs show a stable normalized EQE with reducing length. There is no significant EQE droop even as the size shrinks to 20×20 μm^2. This is mainly attributed to the lower surface recombination velocity of InGaN materials and the μLEDs fabrication process.[25, 26] Such comparison unambiguously points to the advantage of InGaN red μLEDs for small size efficient red μLEDs down to 20×20 μm^2, which are very promising for the μLEDs display application. Most importantly, 5×5 μm^2 red μLEDs with an EQE of 5% are targeted for μLEDs display technology and we believe that InGaN red μLEDs would have large potentials for such efficiencies.

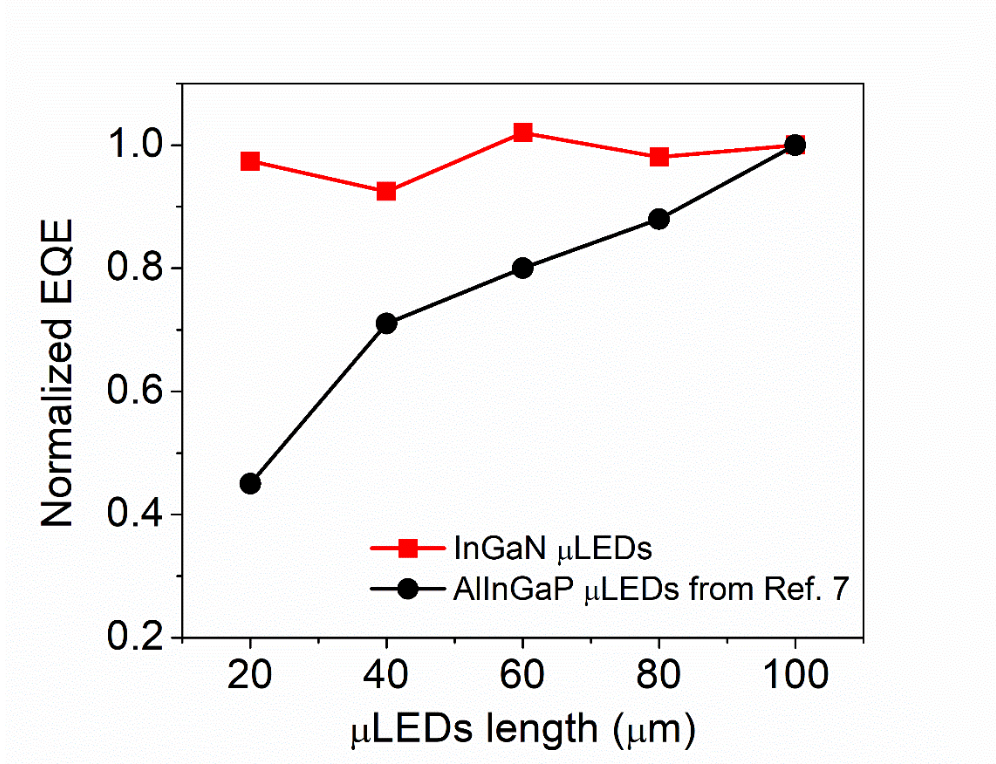

FIG. 5. Comparison of normalized peak EQE for square InGaN and AlInGaP red μLEDs with different lengths. Reprinted with permission from Wong et al. Opt. Express 28, 5787-5793 (2020).[7] © The Optical Society.

In summary, we demonstrate size-independent peak EQE InGaN red μLEDs, showing good optical and electrical properties. The InGaN red μLEDs exhibit a single emission peak at 611 nm at 3 A/cm^2 and a peak EQE around 2.4% to 2.6%. These results point out the promising potentials of achieving high EQE red μLEDs by utilizing InGaN materials.

4.2 Robust temperature property of InGaN red μLEDs

Red μLEDs are especially challenging: although conventional AlInGaP red LEDs can be efficient, the efficiency of AlInGaP μLEDs suffers from severe size-effects, due to a high surface recombination velocity of AlInGaP materials. [7, 8] AlInGaP-based red μLEDs also show a degradation in output power and external quantum efficiency (EQE) at high operation temperature, which is caused by carrier leakage over the quantum barriers and electron-drift-induced reduction in injection efficiency. [27~29]

For GaN-based μLEDs, the peak EQE can be maintained thanks to proper sidewall passivation or chemical treatments, which is essential for μLEDs devices.[25] However, the well-known "green gap", i.e., the dramatic efficiency reduction when the emission wavelength extends into green range, remains challenging for InGaN-based LEDs.[14] To achieve red emission, the indium composition of the InGaN/GaN multiple quantum wells (MQWs) should be higher than 30%, making the epitaxy of red LEDs even more challenging.[14, 16] A low growth temperature is required to increase the indium incorporation efficiency, which can deteriorate the material's crystal quality. The high indium composition InGaN quantum wells (QWs) create a large piezoelectric field, resulting in a strong quantum-confined Stark effect and a further decrease in internal quantum efficiency (IQE). Although several growth technologies have been employed such as strained relaxed nano-porous GaN,[18] InGaN pseudo-substrate[19] and thick n-type GaN layer,[30] the reported EQE of InGaN-based red

μLEDs remains very low (<1%).[16~19] Moreover, while it is known that blue and green InGaN LEDs can be efficient up to high temperature, the thermal droop behavior of InGaN red μLEDs remains unclear.

We recently achieved InGaN red μLEDs with an EQE over 2%, as discussed in Ref. 31. In this Letter, we study the high temperature electroluminescent (EL) properties of such InGaN red μLEDs (40×40 μm^2), which show a peak wavelength of 600 nm and a peak EQE of 3.2%

The InGaN epitaxial wafers were grown on polar *c*-plane patterned sapphire substrate by atmospheric pressure metal-organic chemical vapor deposition. Trimethylgallium, triethylgallium, trimethylaluminium, trimethylindium, bicyclopentadienyl, disilane, and ammonia sources were used as precursors and dopants. The MQWs consist of 5 pairs of InGaN QWs, AlGaN cap layers and GaN barriers. The detailed epitaxy structure is described in Ref. 31. 40×40 μm^2 size μLEDs were fabricated. A 110-nm thick indium-tin oxide contact was first deposited on p-type GaN. 40×40 μm^2 mesas were exposed by reactive-ion etching. An omnidirectional reflector formed by SiO_2 and Ta_2O_5 stacks was deposited. 30 nm SiO_2 was deposited by atomic layer deposition for sidewall passivation. Finally, 600-nm/100-nm/600-nm Al/Ni/Au metals were evaporated as contacts and pads. Fig. 6(a) shows a scanning electron microscope (SEM) image of the fabricated 40×40 μm^2 μLED. Fig. 6(b) shows the EL spectrum of the μLEDs at a current density J = 20 A/cm^2 at room temperature: it has a single emission peak at 600 nm with a full width half maximum (FWHM) of 48 nm, suggesting a high crystal quality of the InGaN red QWs.

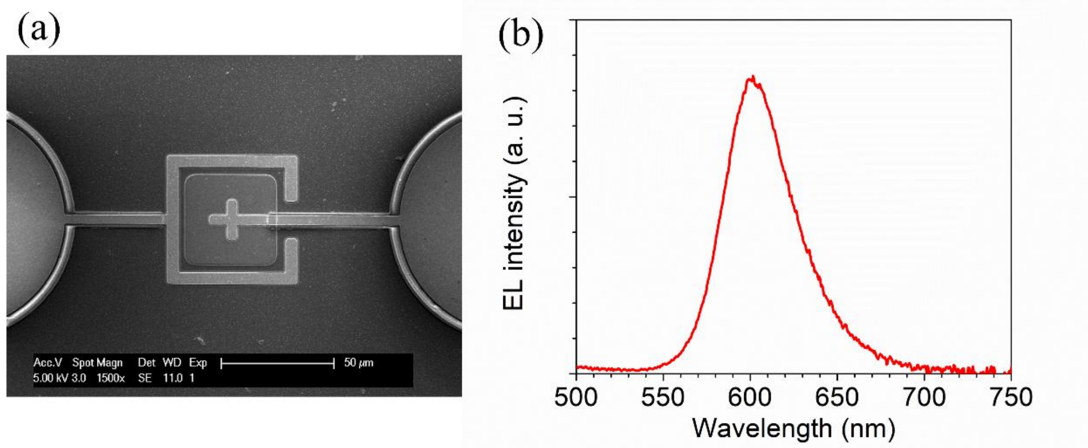

FIG. 6(a) SEM image of 40×40 μm^2 μLEDs and (b) Emission spectrum of InGaN μLEDs at 20 A/cm^2, showing a peak wavelength of 600 nm and a FWHM of 48 nm.

Fig. 7 shows the EL peak wavelength of the InGaN μLEDs at a current density of 20 A/cm^2 as the stage temperature increases from 300 K to 400 K. The peak wavelength λ shows a linear redshift with increasing the temperature *T*. The slope of the peak wavelength redshift versus temperature is 0.05 nm/K, which is lower than the 0.085 nm/K in the InGaN red LEDs grown on Ga_2O_3 substrate[29] and is much lower than the value of 0.137 nm/K in 630 nm AlInGaP red LEDs.[33] Therefore, InGaN-based red μLEDs are promising candidates for high temperature wavelength-stable lighting sources.

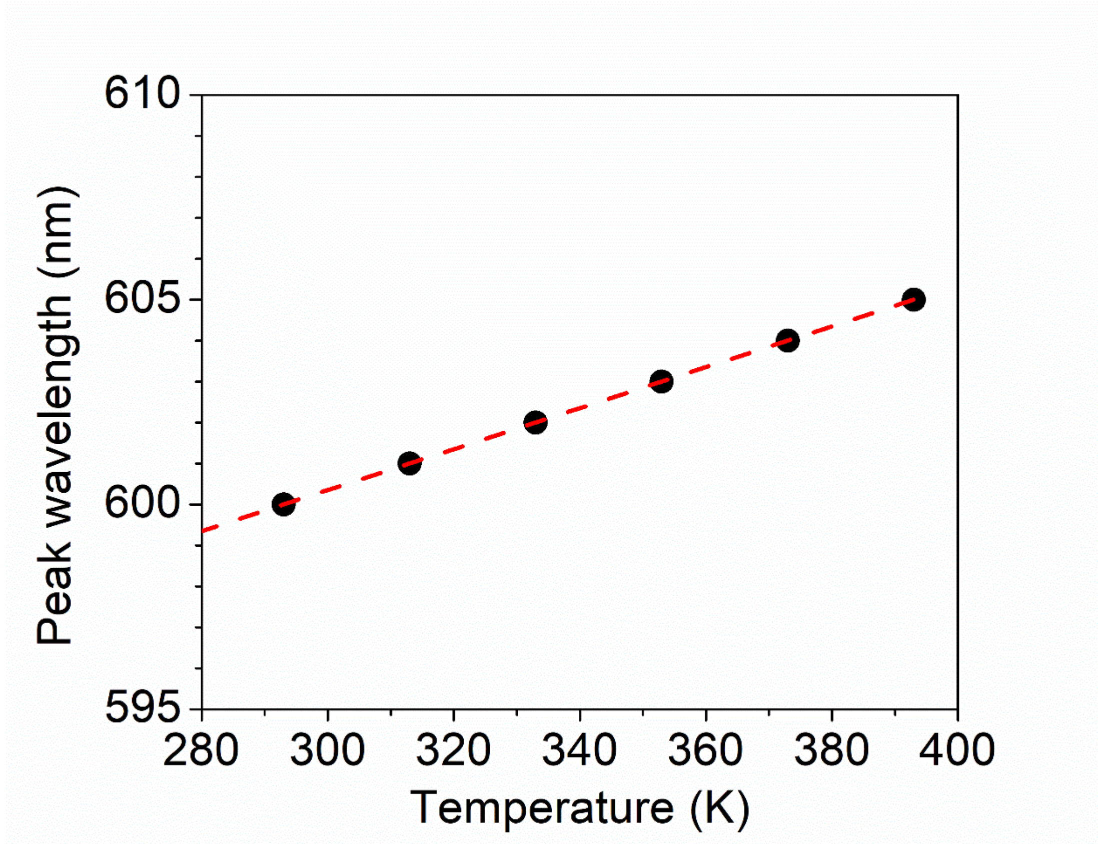

FIG. 7. EL peak wavelength versus temperature with linear fitting. The slope is 0.05 nm/K.

Fig. 8(a) shows the temperature-dependent current density-forward voltage (*J*-V) characteristics from 300 K to 400 K. Note that, at the highest temperatures (380 K and 400 K), the device becomes leaky at low current – this might be due to a leakage path induced by temperature and high-current operation. The forward voltage decreases with increasing temperature, which is usually observed in *pn* diodes. However, the voltage reduction observed here is substantial (4 mV/K), and an order of magnitude larger than what would be expected from bandgap shrinkage alone. This data can be re-cast in terms of electrical efficiency (EE), defined as EE = 1240 / (λ*V). In optimized blue InGaN LEDs with near-ideal injection, the EE can exceed unity (due to the thermocooling effect) and reaches ~1.05 at J = 10 A/cm^2.[26] In the present red μLEDs, the EE has a moderate value of 0.68 at room temperature, and rises

to 0.78 at 400 K. We interpret this data as follows: these μLEDs still suffer from imperfect injection (possibly due to trap-assisted transport and/or excess voltage barriers at heterointerfaces), causing a higher-than-ideal voltage and a reduced EE. As the temperature increases, thermal energy mitigates the injection-limiting processes, the voltage drops rapidly and the EE rises. We believe that, with future improvements in the doping and epitaxial stack, substantially-higher EE values could be achieved.

The J-V data can also be analyzed in terms of the ideality factor. In the conventional drift-diffusion model, the current I can be expressed by $I = I_0 \exp{(qV/nKT)}$, where n is the ideality factor, q is the elementary charge, and T is the absolute temperature. n can be obtained by $n = \left(\frac{q}{KT}\right)\left(\frac{dlnI}{dv}\right)^{-1}$, from the slope of the linear region of log$J$-V curves.[34] The extracted values of n at 1 A/cm^2 at various temperatures are shown in Fig. 8(b). The ideality factor n decreases from 6.7 to 5.0 from 300 K to 360 K (above this temperature, the device becomes leaky, which artificially increases the value of n). According to the Sah-Noyce-Shockley theory of *pn* junctions, the ideality factor n is between 1 and 2, and is caused by the recombination of carriers injected in the neutral regions and mediated by recombination centers located near the intrinsic Fermi level.[34, 35] This is typically observed in optimized InGaN blue LEDs grown on sapphire substrate or bulk GaN substrate.[34, 36] An ideality factor larger than 2 can be caused by trap-assisted tunneling, carrier leakage, and other sources of imperfect injection. Therefore, the high ideality factors observed here indicate non-ideal transport, possibly caused by significant defect-assisted processes. The reduction in n at high temperature indicates an improvement in injection processes. This is consistent with our previous discussion of the EE.

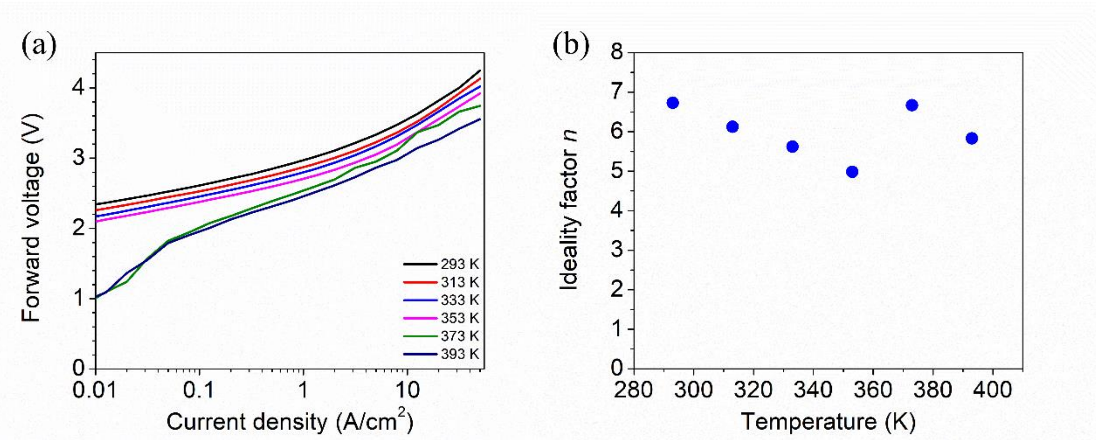

FIG. 8(a) Current density-forward voltage curves of InGaN μLEDs and (b) Ideality factor at various temperatures from 300 K to 400 K

Fig. 9(a) shows the measured EQE versus *J* (on the logarithmic scale), from room temperature to 400 K. It is worth noting that the peak EQE is as high as 3.2% at room temperature, which is much higher than the EQE of 0.2% in InGaN red μLEDs grown on nano-porous GaN substrate[18] and the EQE of 0.56% reported by Zhuang *et al.*[30] The shape of the EQE curve is very flat, especially at room temperature, and cannot be interpreted by the standard *ABC* model; we speculate that imperfect injection dominates the EQE shape at low current, causing this non-standard shape. The onset of current droop is around 3 A/cm^2. As the temperature increases, the peak EQE decreases, especially at low current density. The hot/cold factor (HC factor) i.e., the ratio of high-temperature EQE to room-temperature EQE, is used to quantify the thermal droop behavior.[37] The EQE HC factor versus *J* is shown in Fig. 4(b): the HC factor increases with current density for all temperatures. At 50 A/cm^2, the EQE HC factor is as high as 0.85 at 360 K and 0.72 at 400 K. The HC value at 360 K is similar to that of commercial blue InGaN LEDs, suggesting that this high-temperature robustness is a general property of the InGaN material system. At the highest temperatures (380 K and 400

K), the HC factor is very low at a low current density; this is because the device became leaky during the measurement. Therefore, we believe that the HC factor at these temperatures is somewhat under-estimated.

We now discuss the possible interpretation of the HC factor data. In blue LEDs, the HC factor has been studied by various teams: in defective LEDs (especially those grown on sapphire with large defect density), the low HC factor is dominated by defect-assisted tunneling;[38] in low-defect LEDs (such as those grown on bulk GaN substrates), the HC factor can be very high, and is caused by a decrease in injection efficiency at high temperature.[37] In the present LEDs, several explanations are possible. Generally, due to a large lattice match and low growth temperature, the defect density in of InGaN/GaN red MQWs is high. Therefore, defect-related processes are likely to play an important role both in the carrier recombinations and the transport of InGaN red µLEDs. This is supported by the high ideality factor in Fig. 8.[38, 39] One possible interpretation is that non-radiative Shockley-Read-Hall recombinations are increasing with temperature (however, a quantitative assessment is difficult here since the EQE shape is not well explained by the *ABC* model); another is that defect-assisted tunneling becomes more pronounced, like in blue LEDs. In addition, thermal activation of a defect-assisted droop process is possible.[40] Further studies will be necessary to clarify the nature of thermal droop in red InGaN LEDs.

Finally, the wall-plug efficiency (WPE) and WPE HC factor of the InGaN red µLEDs are shown in Fig. 9(c) and 9(d). For clarity, WPE = EQE * EE. The peak WPE at room temperature is 2.4% at ~3A/cm^2. The WPE HC factor at 400 K at 50 A/cm^2 is 0.85, again indicating a good thermal stability of InGaN red µLEDs. The higher WPE HC factor (0.85) at

50 A/cm^2 compared to the EQE factor (0.72) at 400 K is attributed to the reduction in voltage at high temperature.

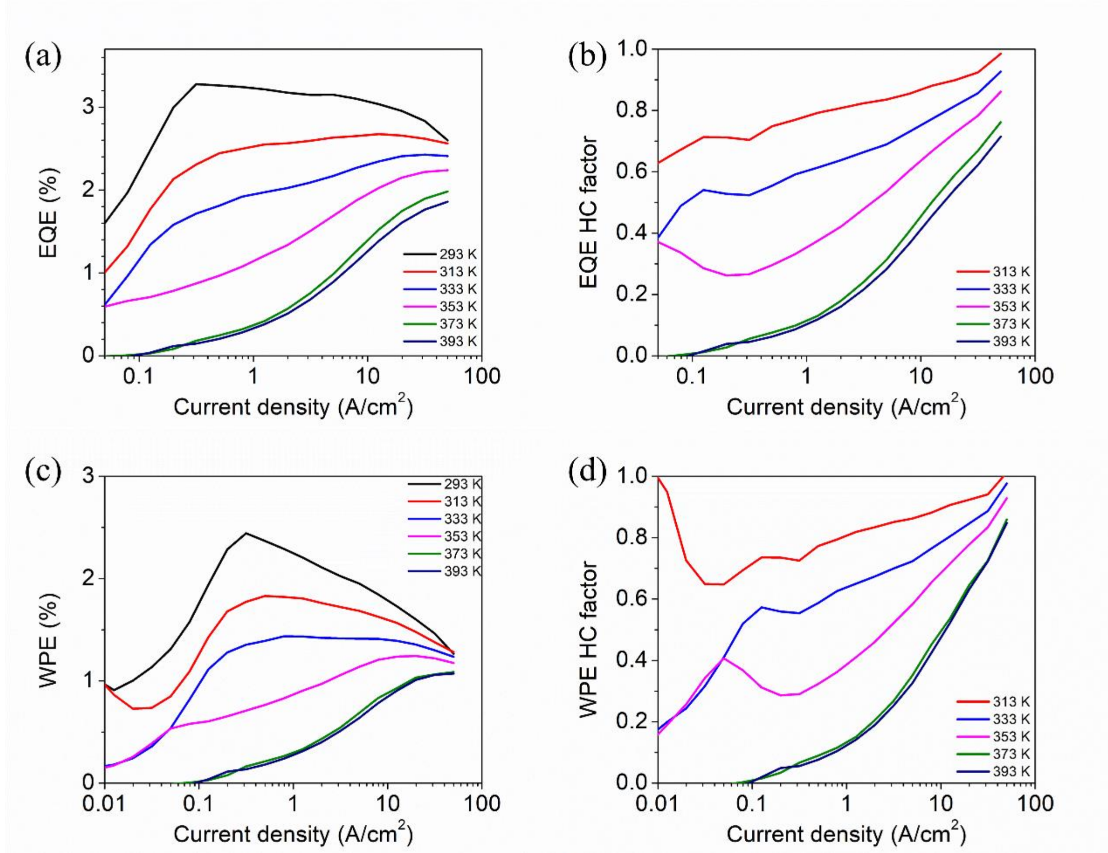

FIG. 4. Temperature-dependent (300 K to 400 K) (a) EQE versus current density; (b) EQE HC factor versus current density; (c) WPE versus current density; (d) WPE HC factor versus current density.

It is worth pointing out that thermal droop is much more pronounced for AlInGaP-based red LEDs. Oh *et al.* measured an EQE HC factor (388 K/298 K) of only 0.55 for regular size (960×960 μm^2) AlInGaP red LEDs.[27] Also, Steranka *et al.* observed a fast degradation of output power at high operation temperature of AlInGaP red LEDs with a HC factor (400 K) of 0.4.[28] It is expected that the HC factor would be even lower in AlInGaP red μLEDs, since the impact of nonradiative recombinations increases significantly for small sizes. Therefore, InGaN red μLEDs exhibit a smaller thermal droop compared to AlInGaP red μLEDs.

In conclusion, we present InGaN red μLEDs with a peak EQE of 3.2%, a peak WPE of 2.4%, and a redshift of 0.05 nm/K versus temperature. At 400 K, we obtain an EQE HC factor of 0.72 and a WPE HC factor of 0.85 at 50 A/cm^2 – both robust values, especially in comparison to AlInGaP red LEDs. The efficiency of our LEDs remains limited by imperfect injection, and further optimization should enable even-better performance. Nonetheless, these results indicate that the InGaN material system is a promising candidate for efficient and temperature-stable red μLEDs.

4.3 Ultra-small 5×5 μm2 InGaN red micro-light-emitting diodes

For AR and VR display applications, very small μLEDs less than 10×10 μm^2 are demanded.[3] The common μLEDs displays are based on AIlnGaP material for red emission and InGaN material for green and blue emission. However, such small AlInGaP red μLEDs face a severe size-effect and show a very low EQE due to a substantial SRH nonradiative recombination by the high surface recombination velocity and sidewall damage. [8,41,42]

Now researchers are pursuing InGaN materials for red emission due to two main advantages: InGaN μLEDs can maintain a high EQE by sidewall passivation or chemical treatments; InGaN μLEDs exhibit a better thermal stability up to high temperature.[18~19] However, InGaN LEDs show a dramatical reduction in EQE as the emission wavelength goes into green range, so called "green gap".[43] For InGaN red μLEDs, the EQE is much lower due to a stronger quantum-confined Stark effect (QCSE).[10] Until now, there are only a few reports about red μLEDs less than 10×10 μm^2.[18,44,] Bi *et al.* presented nano InGaN platelets for red emission, but no electroluminescence (EL) was presented.[44] S. S. Pasayat *et al.* demonstrated InGaN red μLEDs (6×6 μm^2) grown on strained relaxed nano-porous template, however, the

peak EQE is only 0.2%.[18] A. Dussaigne *et al.* utilized InGaNOS substrate to increase indium incorporation efficiency and the 10 µm diameter circular InGaN red µLEDs only show an on wafer EQE of 0.14%.[19] Those EQE values remain very low for AR and VR applications.

In this work, we demonstrate ultra-small 5×5 μm^2 InGaN red µLEDs with a peak EQE of 2.6%. Details of the EL properties are discussed.

The InGaN epitaxial wafers were grown on polar *c*-plane patterned sapphire substrate (PSS) by atmospheric pressure metal-organic chemical vapor deposition. The PSS has coned shape with a height of 1.7 µm, a diameter of 2.6 µm and a space of 0.4 µm. Trimethylgallium, triethylgallium, trimethylaluminium, trimethylindium, bicyclopentadienyl, disilane, and ammonia sources were used as precursors and dopants. The InGaN red LEDs were consisted by a 3 µm undoped GaN, a 3 µm Si-doped n-type GaN, 30 pairs InGaN/GaN superlattices (SLs), 6 pairs of InGaN quantum wells (QWs)/AlGaN cap layer/GaN barriers, Mg-doped AlGaN electron blocking layer, 100 nm Mg-doped p-type GaN and a heavily doped 20 nm p^+GaN.[21, 31] 110 nm indium-tin oxide was deposited. µLEDs with 5×5 μm^2 patterns were defined by GCA Autostep 200 lithography and the mesa was formed by reactive ion etching. 3 pairs SiO_2 and Ta_2O_5 stacks with 30 nm Al_2O_3 were deposited by Veeco NEXUS ion beam deposition. 30 nm SiO_2 was deposited by atomic layer deposition as sidewall passivation layer. Finally, 600 nm/100 nm/600 nm Al/Ni/Au metals were deposited as contacts to n-GaN and pads.[41] Fig. 10(a) shows a scanning electron microscope (SEM) image of the 5×5 μm^2 µLED. Fig. 10(b) is the microscope image of the 5×5 μm^2 µLED at a current density (J) of 3 A/cm^2 under room-temperature. The "hexagonal" like pattern is attributed to the scatting effect of the red emission through the PSS.

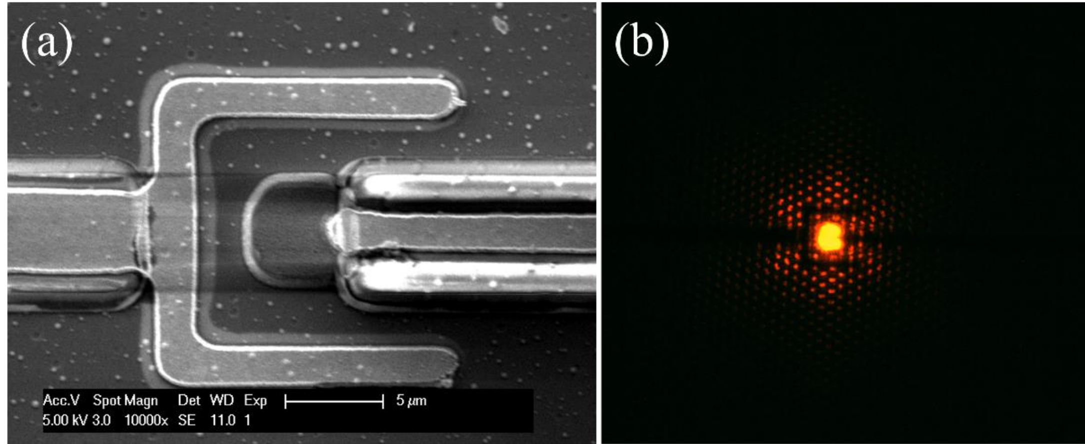

FIG. 10(a) SEM image of the InGaN 5×5 μm^2 μLED and (b) EL image of 5×5 μm^2 red μLED by microscope, showing uniform red emission and light scatting pattern. The device in 1(a) and 1(b) is aligned in a same direction.

The emission spectrum of the InGaN μLEDs at 3 A/cm^2 is shown in Fig. 11(a). It has a single emission peak at 607 nm with a narrow full-width half maximum (FWHM) of 44 nm, suggesting a high crystal quality of the InGaN red QWs.[17~18] Fig. 11(b) shows the EL peak wavelength and FWHM versus *J*. The EL peak wavelength exhibits a large blue-shift from 617 nm to 570 nm as the *J* increases from 0.5 A/cm^2 to 70 A/cm^2, which is caused by the large piezoelectric field in the *c*-plane polar InGaN red QWs with a very high indium composition. The FWHM slightly reduces from 45.4 nm to 43.4 nm with increasing *J* from 0.5 A/cm^2 to 4 A/cm^2, and then it increases linearly to 51 nm as *J* reaches 70 A/cm^2. The slope of the FWHM versus *J* is 0.12 nm/(A/cm^2). The initial reduction of FWHM at low *J* is related to coulomb screening of QCSE and the increase of FWHM at high *J* is caused by the carriers filling high-energetic localized centers.[24]

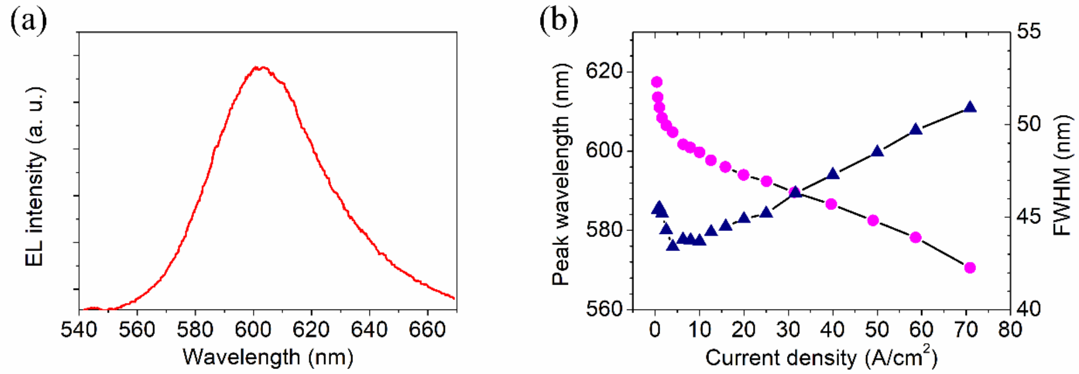

FIG. 11. (a) EL spectrum at 3 A/cm^2; (b) EL peak wavelength and FWHM at various current densities.

Fig. 12(a) shows the current density-voltage (*J*-*V*) curve of the InGaN red µLEDs. At 20 A/cm^2, the forward voltage is 3.3 V. The turn on voltage at 1 A/cm^2 is ~2.4 V. The inset shows the reverse current. The reverse current is as low as ~10^{-9} A at -5 V, indicating an excellent suppression of leakage paths in the sidewalls area. In *pn* diodes, the injection current *I* can be expressed by $I = I_0 \exp{(qV/nKT)}$, where *n* is the ideality factor, *q* is the elementary charge, and *T* is the absolute temperature.[35] Therefore, *n* can be extracted by $n = \left(\frac{q}{KT}\right)\left(\frac{dlnI}{dv}\right)^{-1}$. The *n* is as high as ~8 at 3 A/cm^2, indicating a trap-assisted transport and/or tunneling.[35] The most possible cause is the high defect density in the InGaN red multiple quantum wells (MQWs) due to a low growth temperature and a large lattice mismatch. Fig. 12(b) presents the output power and luminous flux at different *J*, which were collected by an integrating sphere. Both output power and luminous flux increase with *J*. At 20 A/cm^2, the output power and luminous flux is 0.27 µW and 1.27×10^{-4} lm, respectively. The corresponding output power density and luminous flux density is 10.6 mW/mm^2 and 5.1 lm/mm^2, respectively. Moreover, the EQE versus *J* is shown in Fig. 12(b). The EQE increases with *J*, reaches a peak at 2.6% with an onset *J* of 20 A/cm^2 and then starts to decrease. Such efficiency droop is typically observed

in *c*-plane polar InGaN green LEDs.[21, 43] It is worth noting that both peak EQE (2.6%) and output power density (10.6 mW/mm^2) in our 5×5 μm^2 InGaN red μLEDs are much higher than the values reported about InGaN red μLEDs.[17~19]

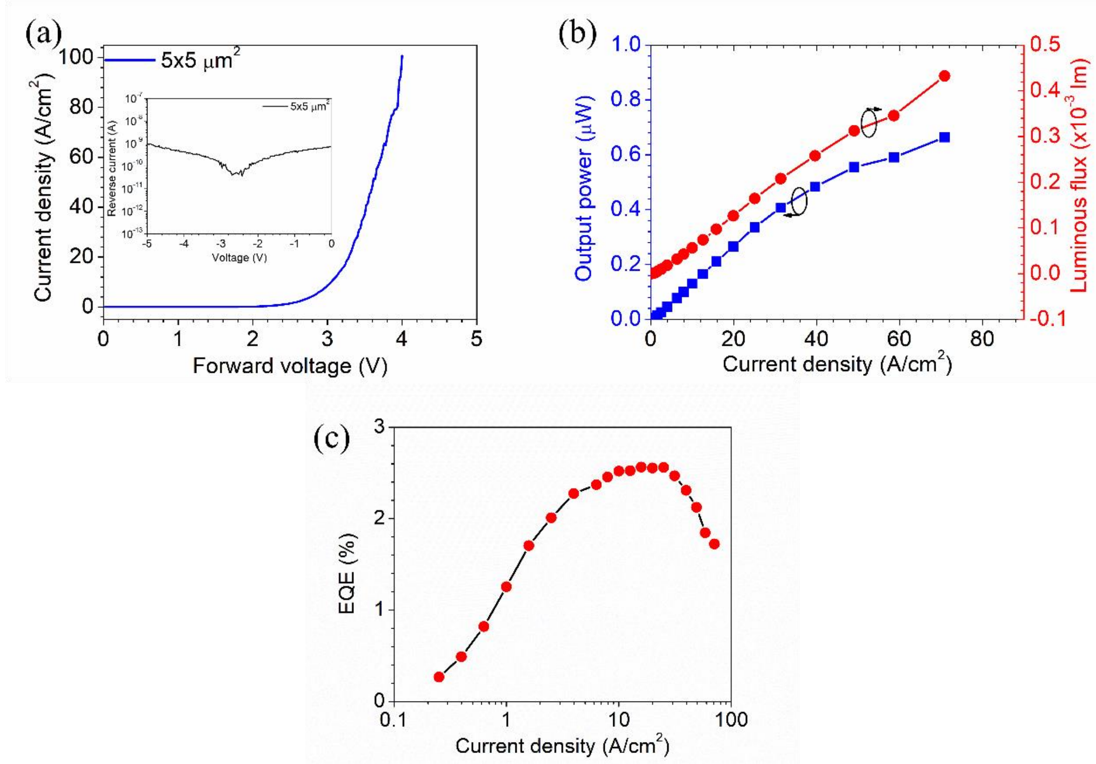

FIG. 12(a) Current density-forward voltage of InGaN 5×5 μm^2 μLEDs; (b) Output power and luminous flux versus current densities; (c) EQE at various current densities.

Furthermore, we compare the EQE versus J of InGaN red μLEDs with a size of 5×5 μm^2 and 100×100 μm^2, as shown in Fig. 13. The 100×100 μm^2 red μLEDs were fabricated on the same epitaxy wafer with a same process. The peak EQE of 100×100 μm^2 μLEDs is 3.2%, which is higher than the value of 5×5 μm^2 devices (2.6%). The EQE droop ratio is defined by $(EQE_{peak}-EQE)/EQE_{peak}$. At 70 A/cm^2, the EQE droop ratio is 0.8 and 0.67 for the 100×100 μm^2 and 5×5 μm^2 red μLEDs, respectively. In conventional *ABC* model, EQE can be expressed by $EQE=LEE*BN^2/(AN+BN^2+CN^3)$, where LEE, A, B, C, and N represents light extraction efficiency, SRH nonradiative recombination, radiative recombination, Auger

recombination coefficients and carrier density.[26] For the 5×5 μm^2 μLEDs, the impact of nonradiative recombination induced by the sidewall damage (A') cannot be neglectable since the ratio of sidewall area to mesa area is 20 times higher than that of the 100×100 μm^2 μLEDs,[45] although the InGaN red μLEDs could exhibit a size-independent EQE scaled down to 20×20 μm^2.[31] The total SRH nonradiative recombination equals to (A+A'), resulting in a reduction of the peak EQE and a severe efficiency droop.[45] Noted that the light extraction simulation by Light Tool (no shown here) reveals that the LEE in 5×5 μm^2 μLEDs is slightly higher than the 100×100 μm^2 μLEDs due to an improved light scatting from the sidewalls.[26, 46] Both improved LEE and uniform current spreading in the 5×5 μm^2 InGaN μLEDs should be beneficial for a higher EQE. In fact, the 5×5 μm^2 InGaN red μLEDs show a lower EQE and severe efficiency droop, suggesting the impact of nonradiative recombination from the sidewall damages. Generally, the size-effect in the 5×5 μm^2 InGaN red μLEDs is not significant compared to the dramatical reduction of EQE in AlInGaP μLEDs. We believe taht the EQE can be furtherly improved by reducing the defects and enhancing the current injection efficiency.[8, 31,41]

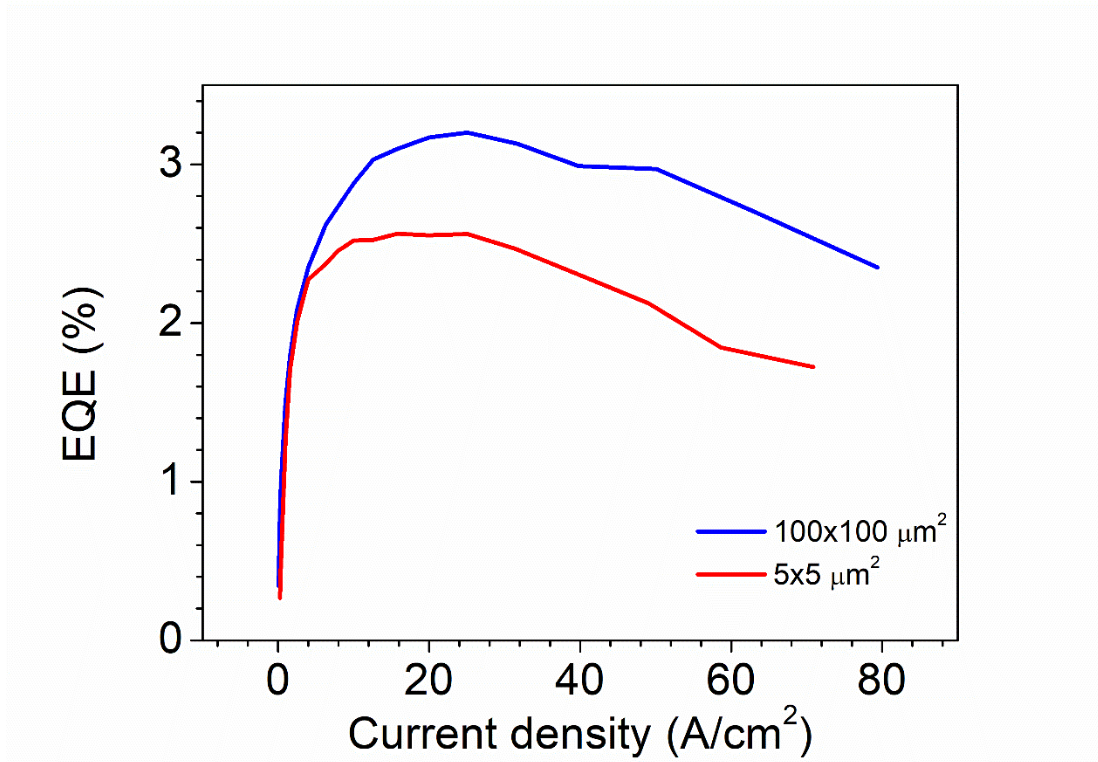

FIG. 13. Comparison of EQE versus current densities for 100×100 μm^2 and 5×5 μm^2 InGaN red μLEDs.

In summary, we demonstrate efficient ultra-small 5×5 μm^2 InGaN red μLEDs with a peak EQE of 2.6%. At 3 A/cm^2, the single peak wavelength is 607 nm and the FWHM is 44 nm. The μLEDs show a high output power density of 10.6 mW/mm^2 and luminous flux density of 5.1 lm/mm^2. These results pave the way for the implementation of AR and VR displays using ultra-small InGaN red μLEDs.

4.4 Red InGaN micro-light-emitting diodes (>620 nm) with a peak external quantum efficiency of 4.5% using an epitaxial tunnel junction contact

In this study, we demonstrate efficient InGaN true red μLEDs with a peak emission wavelength over 620 nm and a peak EQE of 4.5% at ~1 A/cm^2, by utilizing MOCVD grown TJs. Details of the growth, fabrication and optical/electrical properties of the devices are discussed.

The InGaN red LEDs epitaxial wafer was grown on a conventional *c*-plane patterned sapphire substrate by atmospheric-pressure MOCVD. Trimethylgallium, triethylgallium, trimethylaluminium, trimethylindium, bis-cyclopentadienyl magnesium, ammonia and disilane were used as precursors and dopants. Details of the epitaxial structure and μLEDs fabrication can be seen in Fig. 14(a). The red LEDs epitaxial stacks consisted of 3 μm unintentionally doped GaN, 3 μm Si-doped n-GaN, 30 pairs $In_{0.04}Ga_{0.96}N$/GaN superlattices, 6 pairs of InGaN/AlGaN/GaN multiple quantum wells (MQWs), 20 nm p-AlGaN electron blocking layer, 100 nm Mg-doped p-GaN and 20 nm Mg heavily doped p-GaN.[12, 13] The TJs are consisted by 2 nm $In_{0.14}Ga_{0.86}N$, 20 nm n^+GaN (Si concentration>1.5×10^{19} cm^{-3}), 380 nm n-GaN (Si concentration: 7×10^{18} cm^{-3}) and 20 nm n^+GaN (Si concentration: 3×10^{18} cm^{-3}). SAG technology was employed for the TJs overgrowth. 2.5 μm diameter SiO_2 apertures (200 nm thick) were formed on top of the LEDs. The LEDs were treated with aqua regia at 80 °C for 30 mins before the TJs overgrowth.[8, 9, 26] 60×60 μm^2 μLEDs were fabricated. n-GaN mesa was exposed by reactive-ion etching. The μLEDs were treated by 5 mins H_3PO_4 and 5 mins BHF and then activated by rapid thermal annealing at 700 °C for 30 mins in N_2 ambient. An omnidirectional reflector (ODR) by SiO_2 and Ta_2O_5 stacks was deposited. 30 nm SiO_2 was deposited by atomic layer deposition (ALD) for sidewall passivation. Finally, 600-nm/100-

nm/600-nm Al/Ni/Au metals were evaporated. Fig. 14(b) is a scanning electron microscope (SEM) image of the 60×60 μm^2 μLED.

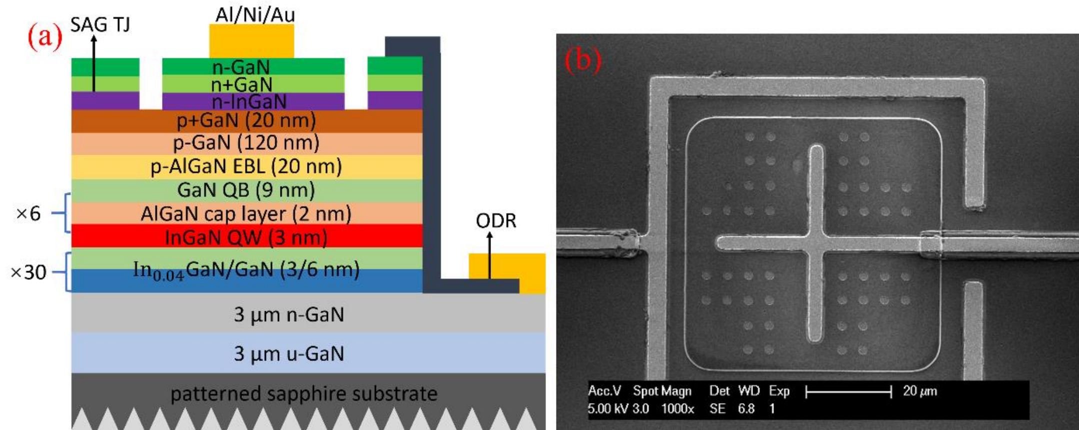

FIG. 14(a) Schematic epitaxial stacks and devices structure of InGaN red μLEDs; (b) SEM image of the 60×60 μm^2 InGaN red μLEDs.

The inset of Fig. 15(a) shows the optical microscopy image of the electroluminescence (EL). The uniform red emission indicates that the buried p-GaN is fully activated with MOCVD grown TJs. In SAG TJ μLEDs, the H atoms in the p-GaN can be driven out through both sidewalls and SAG apertures.[8] Fig. 15(a) shows the EL spectrum of the μLEDs at a low current density of 1 A/cm^2. The single emission peak is centered at 623 nm and the full-width half maximum (FWHM) is 47 nm, suggesting a high crystal quality of the InGaN red QWs. Fig. 2(b) describes the EL peak wavelength of the InGaN red μLEDs and FHWM at different current densities from 0.03 A/cm^2 to 100 A/cm^2. The corresponding wavelength blue-shift is 59 nm, which is caused by the large piezoelectric field in the (0001) polar InGaN red MQWs. Similar large wavelength blue-shift in (0001) InGaN red LEDs was reported in Ref. 25 and Ref. 27. The FWHM reduces at a low current density region (<1 A/cm^2) and then increases at a high current density, which is related to the screen of the piezoelectric field and carriers band filling effect. Considering that μLEDs in self emissive micro-displays are usually operated at

20 A/cm^2,[28] a longer emission wavelength with minimal wavelength shift can be easily obtained in InGaN red μLEDs.

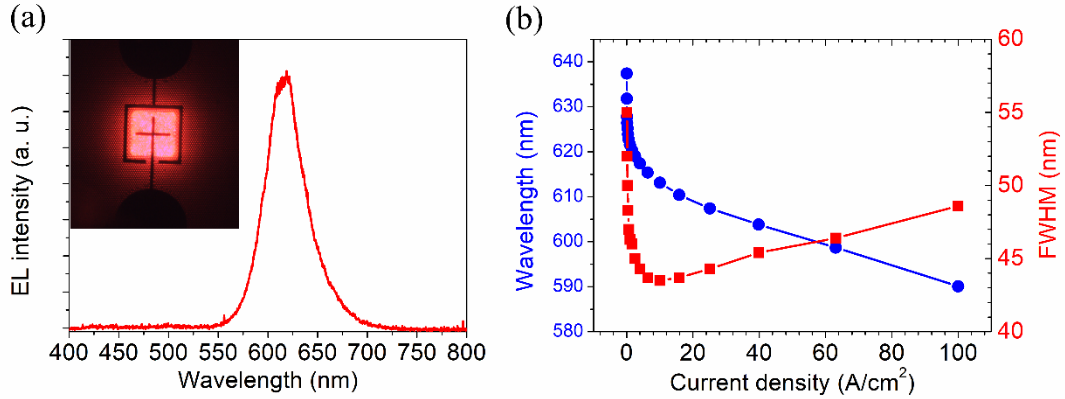

FIG.15(a) EL spectrum at 1 A/cm^2. The inset shows the μLEDs EL image under microscope; (b) Peak wavelength and FWHM versus injection current density.

Fig. 16(a) shows the current density-forward voltage (*J*-*V*) curve. At 20 A/cm^2, the forward voltage (*V*) is 4.5 V and the turn on voltage is 3.2 V. This observed voltage is about 0.7 V higher than InGaN red μLEDs using indium-tin-oxide (ITO) as an ohmic contact.[12] The ideality factor *n* can be extracted from the *J*-*V* curve. In *pn* diode, the current density *J* can be expressed by $J = J_0 \exp{(eV/nKT)}$ based on drift-diffusion model, where *n* is the ideality factor, *e* is the elementary charge, and *T* is the absolute temperature. Thus, the ideality factor can be calculated by $n = \left(\frac{q}{KT}\right)\left(\frac{dlnI}{dV}\right)^{-1}$.[13, 29] The ideality factor *n* in our InGaN red TJ μLEDs is 4.5 at 20 A/cm^2 while the ideality factor of the optimized LEDs should be between 1.0 to 2.0.[30, 31] Electrical efficiency (*EE*) can be considered in InGaN red TJs μLEDs, which is defined as the ratio of the photon energy to the potential energy of injected electrons. It can be obtained by $EE = qV_{photon}/qV = 1240/(\lambda * V)$, where λ is the emission wavelength.[12] The *EE* versus current density on the logarithmic scale is shown Fig. 16(b). The *EE* shows a high peak

of 0.8 at a very low current density and reduces with increasing current density. In optimized LEDs/μLEDs, the *EE* should approach to 1.0 at a low current density.[31] Combing the high ideality factor and the low *EE*, the InGaN red TJ μLEDs suffer from an imperfect injection efficiency. Since InGaN red LEDs require a low growth temperature and exhibit a large lattice mismatch between InGaN and underlying GaN substrate, high dislocations densities and other crystalline defects would be presented in the active region. These defects could result in trap assisted transport into the active region by reducing injection efficiency.[32] Non-idealized electron and hole transport at TJs heterointerfaces could be another cause for the low *EE*, since the *V* in our InGaN red TJ μLEDs is still 0.7 V higher than that of InGaN red μLEDs with ITO contact.[12] Further optimization of TJs doping in p^+GaN and n^+GaN could reduce the voltage penalty and increase the *EE*.

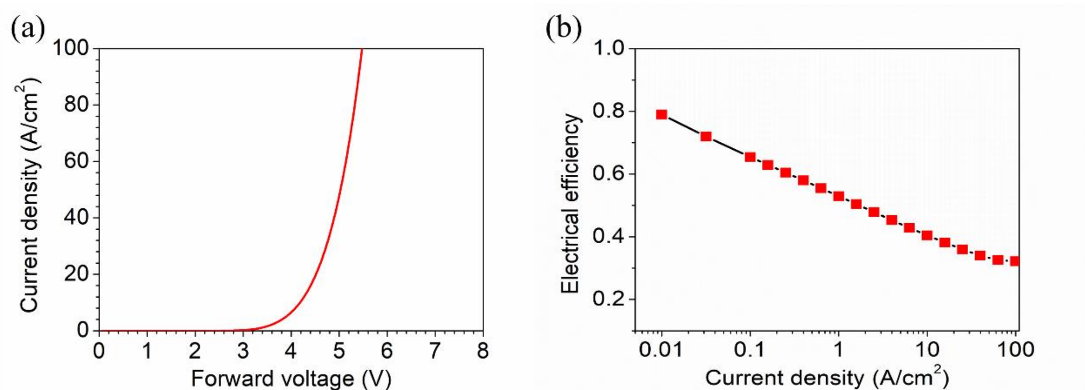

FIG. 16(a) Current density-forward voltage curve of InGaN red μLEDs with epitaxial TJ; (b) Electrical efficiency versus current density on log scale.

Fig. 17(a) shows the output power and output power density versus current density. At 20 A/cm^2, the output power and output power density are 67 μW and 18.6 mW/mm^2, respectively. The luminous flux measured in an integrating sphere increases linearly with current density, as presented in Fig. 17(b). At 20 A/cm^2, the luminous flux is 0.025 lm. For a

proper comparison, the output power density is used to evaluate μLEDs brightness since there are various sizes of μLEDs reported in the literatures. As shown in Fig. 4(c), we compare the output power density at 1 A/cm^2 of the InGaN red μLEDs in this work with the recent reports about both InGaN red μLEDs and AlInGaP red μLEDs.[12, 14, 18, 21, 22, 24, 33, 34] The emission wavelength and the μLEDs sizes are labeled. In Ref. 21, the on-wafer output power density is estimated to be 0.035 mW/mm^2 at 1 A/cm^2 for ~660 nm 10×10 μm^2 InGaN red μLEDs.[21] In our InGaN red TJs μLEDs, the output power density reaches 0.7 mW/mm^2 at 1 A/cm^2, which is much higher than the previous AlInGaP red μLEDs and InGaN red μLEDs at the same current density. These results suggest excellent optical and electrical properties of our InGaN red μLEDs with epitaxial TJs contact.

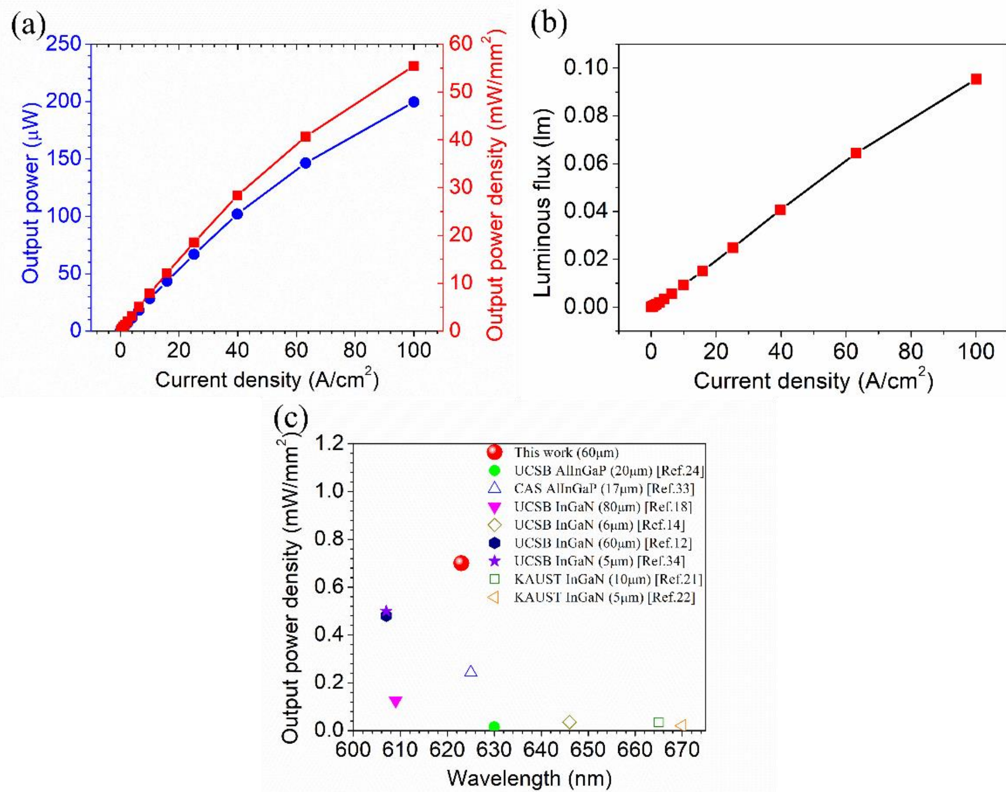

FIG. 17(a) Output power (blue line) and output power density (red line) at different current density; (b) Luminous flux versus current density; (c) Output power density (1 A/cm^2) comparison

with other reports about InGaN red µLEDs and AlInGaP red µLEDs. The solid dots are values measured in the integrating sphere and the hollow dots are on-wafer testing values.

Moreover, Fig. 18 shows the EQE versus current density at room temperature. The inset is the enlarged EQE curve at a low current density until 10 A/cm^2. The peak EQE reaches as high as 4.5% at a low current density of ~1 A/cm^2. The peak EQE is one order higher compared to the EQE reported in the literatures about InGaN red µLEDs by other groups (less than 1%).[14, 18, 21, 22] It has been observed that the InGaN red TJ µLEDs show a higher peak EQE compared to the InGaN red ITO µLEDs with a peak EQE of 3.2% reported recently by our group.[12] Similar significant improvement in the peak EQE of TJ µLEDs was observed by Wong *et al,*[11] which is attributed to the better current spreading, less optical loss and higher light extraction by the SAG apertures.[8, 26] The EQE reduces from 4.5% to 2% at a high current density of 100 A/cm^2, which is potentially related to a high Auger nonradiative recombination, carrier leakage from the InGaN MQWs or reduced *EE* at a high current density. Noted that the EQE droop is accompanied with a strong blue-shift in peak wavelength. Also, the wall-plug efficiency (WPE) versus current density in our InGaN TJ red µLEDs is shown in Fig. 18(b). The peak WPE is 2.5% at ~1 A/cm^2 and it reduces dramatically with increasing current density. Further studies need to be carried out to investigate the efficiency droop behavior in InGaN red LEDs.

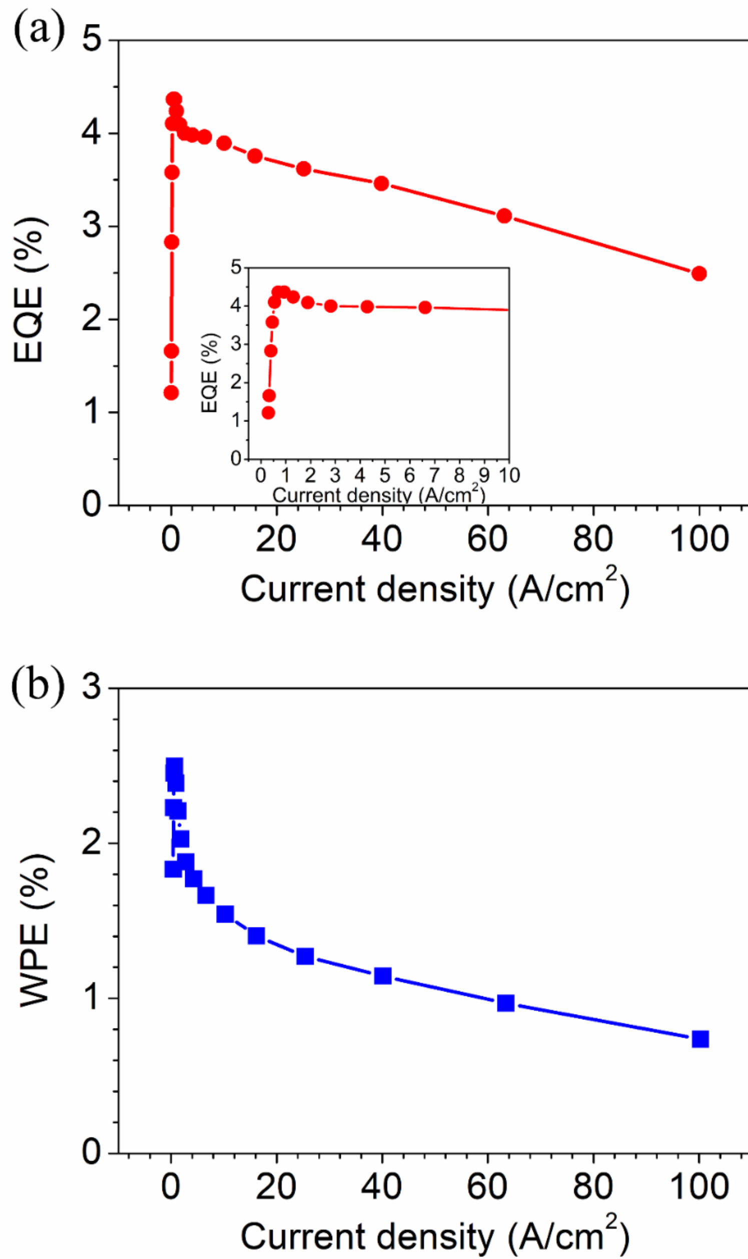

FIG. 18(a) EQE and (b) WPE versus current density of the InGaN red TJ µLEDs measuring in an integrating sphere. The inset in 18(a) shows the enlarged EQE curve at a low current density.

In conclusion, we present 623 nm 60×60 μm^2 InGaN red μLEDs with a high peak EQE of 4.5% at 1A/cm^2 using MOCVD grown TJs. The InGaN red TJ μLEDs show a much higher output power density of 0.7 mW/mm^2 at 1 A/cm^2 compared to the previous AlInGaP red μLEDs and InGaN red μLEDs. These results suggest promising full colors micro-display based on InGaN blue/green/red μLEDs.

References:

1. J. Day, J. Li, D. Y. C. Lie, C. Bradford, J. Y. Lin, and H. X. Jiang, Appl. Phys. Lett. 99, 031116 (2011).
2. J. J. Wierer Jr, N. Tansu, Laser Photonics Rev. 13, 1900141(2019).
3. M. S. Wong, D. Hwang, A. I. Alhassan, C. Lee, R. Ley, S. Nakamura, and S. P. DenBaars, Opt. Express 26, 21324 (2018).
4. H. Li, M. S. Wong, M. Khoury, B. Bonef, H. Zhang, Y. Chow, P. Li, J. Kearns, A. A. Taylor, P. De Mierry, Z. Hassan, S. Nakamura, and S. P. DenBaars, Opt. Express 27, 24154 (2019).
5. P. Li, H. Zhang, H. Li, M. Iza, Y. Yao, M. S. Wong, N. Palmquist, J. S. Speck, S. Nakamura, and S. P. DenBaars, Opt. Express 28, 18707 (2020).
6. P. Li, H. Zhang, H. Li, Y. Zhang, Y. Yao, N. Palmquist, M. Iza, J. S. Speck, S. Nakamura, S. P. DenBaars, Semicond. Sci. Technol. 35, 125023 (2020).
7. M.S. Wong, J.A. Kearns, C. Lee, J.M. Smith, C. Lynsky, G. Lheureux, H. Choi, J. Kim, C. Kim, S. Nakamura, J.S. Speck, and S. P. DenBaars, Opt. Express 28, 5787 (2020).
8. J.T. Oh, S.Y. Lee, Y.T. Moon, J.H. Moon, S. Park, K.Y. Hong, K.Y. Song, C. Oh, J.I. Shim, H.H. Jeong, J.O. Song, H. Amano, T.-Y. Seong, Opt. Express 26, 11194 (2018).
9. M. R. Krames, M. Ochiai-Holcomb, G. E. Höfler, C. Carter-Coman, E. I. Chen, I. H. Tan, P. Grillot, N. F. Gardner, H. C. Chui, J. W. Huang, S. A. Stockman, F. A. Kish, M. G. Craford, T. S. Tan, C. P. Kocot, M. Hueschen, J. Posselt, B. Loh, G. Sasser, and D. Collins, Appl. Phys. Lett. 75, 2365 (1999).
10. M. Boroditsky, I. Gontijo, M. Jackson, R. Vrijen, E. Yablonovitch, T. Krauss, C. C.

Cheng, A. Scherer, R. Bhat, and M. Krames, J. Appl. Phys. 87, 3497 (2000).

11. K. A. Bulashevich and S. Y. Karpov, Phys. Status Solidi RRL 10, 480 (2016).
12. T. Mukai, M. Yamada, and S. Nakamura, Jpn. J. Appl. Phys. 38, 3976 (1999).
13. S. F. Chichibu, A. C. Abare, M. S. Minsky, S. Keller, S. B. Fleischer, J. E. Bowers, E. Hu, U. K. Mishra, L. A. Coldren, and S. P. DenBaars, Appl. Phys. Lett. 73, 2006 (1998).
14. J.-I. Hwang, R. Hashimoto, S. Saito, and S. Nunoue, Appl. Phys. Express 7, 071003 (2014).
15. S. Zhang, J. Zhang, J. Gao, X. Wang, C. Zheng, M. Zhang, X. Wu, L. Xu, J. Ding, Z. Quan, and F. Jiang, Photon. Research 8, 1671 (2020).
16. D. Iida, Z. Zhuang, P. Kirilenko, M. Velazquez-Rizo, M. A. Najmi, and K. Ohkawa, Appl. Phys. Lett. 116, 162101 (2020).
17. D. Iida, Z. Zhuang, P. Kirilenko, M. Velazquez-Rizo, M. A. Najmi, and K. Ohkawa, Appl. Phys. Express 13, 031001 (2020).
18. S. S Pasayat, C. Gupta, M. S Wong, R. Ley, M. J Gordon, S. P DenBaars, S. Nakamura, S. Keller, U. K Mishra, Appl. Phys. Express 14, 011004 (2021).
19. A. Dussaigne, F. Barbier, B. Damilano, S. Chenot, A. Grenier, A. M. Papon, B. Samuel, B. Ben Bakir, D. Vaufrey, J. C. Pillet, A. Gasse, O. Ledoux, M. Rozhavskaya, and D. Sotta, J. Appl. Phys. 128, 135704 (2020).
20. Z. Zhuang, D. Iida, K. Ohkawa, Appl. Phys. Lett. 116, 173501 (2020).
21. A.I. Alhassan, R.M. Farrell, B. Saifaddin, A. Mughal, F. Wu, S. Nakamura, S.P. DenBaars, and J.S. Speck, Opt. Express 24, 17868 (2016).
22. A.I. Alhassan, N.G. Young, R.M. Farrell, C. Pynn, F. Wu, A.Y. Alyamani, S. Nakamura, S.P. DenBaars, and J.S. Speck, Opt. Express 26, 5591 (2018).
23. H. Li, P. Li, J. Kang, Z. Li, Y. Zhang, M. Liang, Z. Li, J. Li, X. Yi, G. Wang, Appl. Phys. Express 6, 092101 (2013).
24. Y. J. Lee, C. H. Chiu, C. C. Ke, P. C. Lin, T. C. Lu, H. C. Kuo, and S. C. Wang, IEEE J. Sel. Top. Quantum Electron. 15, 1137(2009).
25. M.S. Wong, C. Lee, D.J. Myers, D. Hwang, J.A. Kearns, T. Li, J.S. Speck, S. Nakamura, and S.P. DenBaars, Appl. Phys. Express 12, 097004 (2019).
26. R. T. Ley, J. M. Smith, M.S. Wong, T. Margalith, S. Nakamura, S. P. DenBaars, and

M. J. Gordon, Appl. Phys. Lett. 116, 251104 (2020).

27. C.-H. Oh, J.-I.Shim, and D.-S. Shin, J. J. Appl. Phys. 58, SCCC08 (2019).
28. F. M. Steranka, J. Bhat, D. Collins, L. Cook, M. G. Craford, R. Fletcher, N. Gardner, P. Grillot, W. Goetz, M. Keuper, et al., Physica Status Solidi (a). 194, 380 (2002).
29. J. Cho, E. F. Schubert, and J. K. Kim, Laser Photon. Rev. 7, 408 (2013).
30. Z. Zhuang, D. Iida, M. Velazquez-Rizo, K. Ohkawa, IEEE Electron. Dev. Lett. 17, 1029 (2021).
31. P. Li, H. Li, H. Zhang, C. Lynsky, M. Iza, J. S. Speck, S. Nakamura, and S. P. DenBaars, Appl. Phys. Lett. 119, 081102 (2021).
32. P.G. Eliseev, P. Perlin, J. Lee, M. Osiński, Appl. Phys. Lett. 71, 569 (1997).
33. H. K. Lee, D. H. Lee, Y. M. Song, Y. T. Lee, and J. S. Yu, Solid-State Electron. 56, 79 (2011).
34. A. David, C. A. Hurni, N. G. Young, and M. D. Craven, Appl. Phys. Lett. 109, 083501 (2016).
35. D. Zhu, J. Xu, A. N. Noemaun, J. K. Kim, E. Fred Schubert, M. H. Crawford, and D. D. Koleske, Appl. Phys. Lett. 94, 081113 (2009).
36. J. M. Shah, Y.-L. Li, Th. Gessmann, and E. F. Schubert, J. Appl. Phys. 94, 2627 (2003).
37. A. David, N. G. Young, C. Lund, and M. D. Craven, Appl. Phys. Lett. 115, 223502 (2019).
38. C. De Santi, M. Meneghini, M. La Grassa, B. Galler, R. Zeisel, M. Goano, S. Dominici, M. Mandurrino, F. Bertazzi, D. Robidas, G. Meneghesso, and E. Zanoni, J. Appl. Phys. 119, 094501 (2016).
39. M. Auf der Maur, B. Galler, I. Pietzonka, M. Strassburg, H. Lugauer, and A. Di Carlo, Appl. Phys. Lett. 105, 133504 (2014).
40. A. David, N. G. Young, C. A. Hurni, M. D. Craven, Phys. Rev. Appl. 11, 031001 (2019)
41. M.S. Wong, J.A. Kearns, C. Lee, J.M. Smith, C. Lynsky, G. Lheureux, H. Choi, J. Kim, C. Kim, S. Nakamura, J.S. Speck, and S. P. DenBaars, Opt. Express 28, 5787 (2020).
42. Y. Zhao, J. Liang, Q. Zeng, Y. Li, P. Li, K. Fan, W. Sun, J. Lv, Y. Qin, Q. Wang, J. Tao, and W. Wang, Opt. Express 29, 20217 (2021)

43. H. Li, P. Li, J. Kang, Z. Li, Y. Zhang, Z. Li, J. Li, X. Yi, J. Li, G. Wang, Appl. Phys. Express 6, 052102 (2014).
44. Z. Bi, T. Lu, J. Colvin, E. Sjögren, N. Vainorius, A. Gustafsson, J. Johansson, R. Timm, F. Lenrick, R. Wallenberg, B. Monemar, and L. Samuelson, ACS Appl. Mater. Interfaces, 12, 1784 (2020).
45. J. Yin, E. Fathi, H. Z. Siboni, C. Xu, and D. Ban, Appl. Phys. Lett. 118, 021105 (2021).
46. J. M. Smith, R. T. Ley, M. S. Wong, Y. Baek, J. Kang, C. H. Kim, M. J. Gordon, S. Nakamura, J. S. Speck, and S. P. DenBaars, Appl. Phys. Lett. 116, 071102 (2020).

5. Demonstration of Yellow (568 nm) Stimulated Emission from Optically Pumped InGaN/GaN Multi-Quantum Wells

Quantum well (QW) laser diodes (LDs) can be fabricated with a broad range of wavelengths, seamlessly spanning UV to mid-infrared depending on the choice of semiconductor material and structural design.[1, 2] Specifically, GaAs-technology enables the commercialization of LDs with wavelengths covering 630 nm to 1350 nm,[3, 4] whereas longer infrared wavelengths can also be accessed by InP and GaSb based structures.[5-7] GaN-based visible LDs from blue to green (400-530 nm) are already commercially available,[1, 8-12] yet reports about yellow semiconductor edge-emitting LDs are rare.[13] Nearly all yellow laser technology has been based on frequency conversion,[14] gas and ion lasers,[15] and dye lasers,[16] all of which are bulky, costly, and tremendously inefficient. Despite the scarcity of available yellow laser sources on the market, there is a fast-growing need for applications in advanced fields of biology and astrophysics.[17] Coherent and powerful yellow emission is an important component for use as a laser guiding star for astronomical observations.[18] With a direct-generation coherent yellow beam, quantum systems using heterogeneous integration of III-V LDs on silicon photonic platforms can be used to study photon entanglement,[19] which has not yet been realized due to the size constraints of current nonlinear yellow lasers.

Realizing high efficiency long-wavelength emission from InGaN QWs is still challenging, which can be obtained by increasing the indium composition in the InGaN QWs.[20-24] Additional indium in the InGaN lattice, however, requires a lower growth temperature and thus degrades epitaxial quality and dramatically decreases the internal quantum efficiency (IQE).[20] The large lattice mismatch between InGaN QWs and GaN also results in a large piezoelectric field and a low IQE due to the poor electron and hole wavefunctions overlap, e.g. quantum-confined Stark effect (QCSE).[20, 21] The dispersion of GaN, InGaN and AlGaN materials has made it more challenging to achieve proper waveguiding and confinement of

the photons, which is crucial for stimulated emission. Previous reports have shown the thickness of AlGaN cladding for adequate mode confinement in InGaN yellow LDs is beyond the critical thickness, and novel structures have been proposed to mitigate this issue.[25] For electrically pumped long-wavelength laser diodes, these challenges lead to a significant increase of threshold and prevent the lasing. In the optical pumping regime, however, issues such as carrier leakage and heat dissipation can be largely neglected and the optical gain from the material can be better exploited at a higher level.[26] However, there have not yet been reports about optically pumped lasing from edge emitting InGaN/GaN QWs.

In this study, we report a 568 nm yellow lasing from high crystal quality InGaN QWs grown on a bulk GaN substrate. Details of the materials growth, device fabrication, optically pumping experiment and lasing characterization are presented.

The structure was grown on the *c*-plane bulk GaN substrate using atmospheric pressure metal organic chemical vapor deposition (MOCVD). Trimethylgallium (TMGa), triethylgallium (TEGa), trimethylaluminum (TMAl), trimethylindium (TMIn), bicyclopentadienyl (Cp_2Mg), disilane (Si_2H_6), and ammonia (NH_3) sources were used as precursors and dopants. The epitaxial structure consists of a 3 µm unintentionally doped (UID) GaN, a 1.5µm n-doped $Al_{0.06}Ga_{0.94}N$ as bottom cladding layer grown at 960°C, a 20 period $In_{0.12}Ga_{0.88}N$/GaN (1.5 nm/3 nm) superlattice (SL) as bottom waveguiding layer grown at 920°C, a 6 period $In_{0.3}Ga_{0.7}N$ yellow QWs/AlGaN cap layers/GaN barriers (2 nm/2 nm/9 nm). The growth temperature of yellow QWs is 760°C. A 5 period $In_{0.12}Ga_{0.88}N$/GaN (1.5 nm /3 nm) superlattice as part of the top waveguiding layer grown at 920°C, and a 10 nm UID GaN as the cap layer. Our group has previously reported green and amber/red LEDs or micro-LEDs using similar active region growth conditions with a high external quantum efficiency.[22, 23]

Due to the nature of optical pumping, scattering loss and back-reflection could be a major source of photon loss during the pumping process, and the smoothness of the epitaxial surface is therefore crucial. Atomic force microscope (AFM) scanning exhibits a smoothness of the epitaxial layer with a roughness of 0.3 nm on a 5×5 μm^2 area as shown in Fig. 1(a). Cathodoluminescence (CL) was used to measure the Threading dislocation (TD) density of the InGaN/GaN MQWs as shown in Fig. 1(b). The TD density was estimated to be ~$5\times10^7/cm^2$ by numerically counting the number of the black spots over a certain area, indicating a high crystal quality of InGaN/GaN MQWs. There still a lot of TDs generated during the epitaxy growth (bulk GaN has a TD of ~10^6 cm^{-2}) due to a low growth temperature and lattice mismatch in the InGaN red MQWs.

Due to the thickness limit of the high Al-content AlGaN layer that can be coherently grown on the GaN before relaxation occurs, it is not uncommon that in green or longer wavelength GaN LDs the optical mode is unsymmetrically skewed towards the substrate.[26] Such asymmetrical mode profile results in additional internal loss and lower modal gain due to weaker confinement. This issue would be exacerbated in the yellow (>560 nm) range due to the high dispersion of InGaN, which requires the top waveguiding layer to have near 10% Indium composition and a thickness of more than 30 nm. To achieve better confinement, one can either increase the thickness of the cladding layer and replace it with a lower refractive index material or increase the refractive index of the waveguiding layer. In our experiment, a quarter-wave dielectric layer of TiO_2 on the top of the epitaxial growth was employed for symmetrical mode shaping. Compared with traditional epitaxial InGaN waveguiding and AlGaN cladding, the use of high refractive index of TiO_2 (near 2.6 at 580 nm)[27] on the top of active regions greatly improves the confinement in the vertical direction by attracting the

mode upward, although such structure will not be valid for electrical injection of LDs. To further examine the validity of such a structure, mode simulation was conducted using the FIMMWAVE software (Fig. 2). In the structure using TiO_2 and Ta_2O_5, the center of the mode overlaps more with the active region.[28] It is worth noting that TiO_2 is also absorptive at the pumping wavelength (355 nm), yet when compared to high In-content InGaN, the absorption coefficient of TiO_2 is still lower. As seen from Table I, compared with a traditional structure with AlGaN cladding and high In-content InGaN waveguiding, the combined use of Ta_2O_5 and TiO_2 layers can enhance the confinement factor by nearly 25% while keeping the internal loss and single pass absorption of the pumping source still at the same level.

After the MOCVD growth, 38 nm Ta_2O_5 and 51 nm TiO_2 was deposited as cladding and waveguiding layers on the sample by using Ion Beam Deposition (IBD). The optical thickness of the Ta_2O_5 was also chosen as a quarter of the pumping wavelength to reduce the back reflection of the pumping beam while the TiO_2 thickness was determined to optimize the confinement factor and internal optical loss. Ridge patterns with different widths (20-50 μm) were formed by low power reactive ion etching to improve the sidewall profile and reduce potential scattering loss. After fabrication, the sample was polished to 75 μm and cleaved into bars of different lengths ranging from 1 to 2 mm along the *m*-direction, as shown in Fig. 3. The cleaved *m*-plane facet shows a smooth surface that can be directly used for laser mirror without any optimization. The cleaved samples were then bonded onto a copper heat sink for testing.

The pumping source utilizes an EKSPLA PL2251 Series Nd:YAG pump laser with 1064 nm as fundamental wavelength. The beam is first sent through a second harmonic crystal combining two photons of the fundamental source to produce a 532 nm laser beam. Then this

beam passes through a third harmonic crystal combining a 1064 nm and 532 nm pulse to produce the desired 355nm light output. The final pulse width is 30 ps firing at 10 Hz. Two 355 nm dichroic mirrors are used to filter out any residual light at the pumping wavelength. Finally, the beam passes through a cylindrical lens, focusing the spot into a narrow line of approximately 100 µm width (Fig. 4). Before each measurement, a power meter is also used to monitor the actual energy per pulse. A spectrometer (OceanOptics 2000) and a multi-mode fiber was placed near the facet and aligned in parrel with the ridges for spectrum and power collection.

Lasing action requires spontaneously emitted photons to be exponentially amplified by stimulated emission as they travel through the waveguide in the active medium, leading to a linear increase of the number of total photons. The generated photons are all coherent in space and frequency, and consequently, at the lasing threshold, an intense beam with spectral narrowing is expected from the facet of the device. The photon emission spectrum at room-temperature with different pumping power densities is shown in Fig.5 (a). The peak emission wavelength was 568 nm with the spectral linewidth reducing from over 50 nm to less than 2 nm at the measured pump-power of 1.5 MW/cm^2. The amplified spontaneous emission occurs at the peak of the broad spontaneous emission spectrum. The optical output power as a function of pumping power density (L-I curve) is also shown in Fig. 5(b), which exhibits a distinct "kink" of slope near P_{th} of 1.25 MW/cm^2. Above threshold, the power of stimulated emission increases linearly with the pumping power density and gradually saturates at higher pumping level. Even though in practice electrically injected LDs have broader applications and impacts, an optically pumped device is undoubtedly a good indicator that the material

quality is competent for future development and can be well regarded as a precursor to electrically injected LDs.

To obtain a positive optical gain, Bernard-Duraffourg inversion condition must be satisfied. It is not only useful but also important to understand how the actual carrier density is correlated with the increasing pumping power density, as it will serve as a guidance for future design of electrically injected laser diodes. It has been observed that at the lasing threshold, the power density is 1.5 MW/cm^2. During one-pass of transmission, the generation rate can be given as:

$$G = \frac{P*\alpha_1*(1-e^{\alpha_2 L})}{h\omega Nt} \quad (1)$$

Where α_1 is the percentage of the pump beam absorbed in the active region, α_2 is the absorption coefficient of TiO_2 at the emission wavelength, P is the pumping pulse peak power, t is the QW thickness and *N* is the total number of the QWs, ω is the emission wavelength. Considering that the incident 355 nm light has the photon energy very close to the band gap of GaN, the generation rate during the pulse in the six QWs (2 nm each) is 6×10^{29} cm^{-3} s^{-1}. Knowing the generation rate, the carrier density can be determined from the carrier lifetime and more specifically, the relation between the generation rate and carrier density (n) under a steady pumping can be given as:

$$n = G\,\tau\,(1 - e^{-T/\tau}) \quad (2)$$

where τ is the carrier lifetime and T is the pulse width. Note that this correlation is only valid when the carrier lifetimes are longer than the pulse width. Under low level photoluminescence measurements, the carrier lifetime is often assumed be a few hundred ps, which is much longer as the pumping pulse used in this experiment. Carrier lifetimes, however, can also be significantly affected by the high-level pumping environment and

apparently the pumping densities used here are orders of magnitude higher than in the previous photoluminescence measurements. Such effect could lead to a pronounced gain saturation and that might account for output power saturation in Fig. 5(b). Unfortunately, there is yet no good quantitative consensus on the carrier lifetime dependence on the pumping level in InGaN QWs. The carrier lifetime in the InGaN red MQWs is assumed to be higher than 2 ns[29, 30, 31] and then we can estimate the threshold carrier density in the QWs is over 3.9×10^{19} cm^{-2} per QW. This value is close to the previously reported transparency carrier densities in InGaN blue and green lasers as well as the condition to reach Mott transition of the excitons into electron-hole plasma.[28] It is thus likely that similar QW structure can be electrically injected to the lasing level if the injection efficiency is high and carrier leakage is circumvented.

To further confirm the lasing, the polarization of the emission was investigated and measured. Based on the simulation, the fundamental mode is always transverse electric (TE) polarized due to its apparent lower optical loss, whose direction is pinned along the direction of the stripe (*m*-plane). The degree of polarization is given as $(I_{max} - I_{min})/(I_{max} + I_{min})$, where I_{max} is the maximum and I_{min} the minimum optical intensity, and can be measured by adding a polarizer to the collection beam path and varying the polarizer angle. The transverse electric (TE) and transverse magnetic (TM) emission spectra from the cleaved laser bar operating above threshold are shown in Figure 6. We observe that the stimulated emission is strongly TE polarized with the degree of polarization (P), over 90%.[12] It is also noted that the TE mode emission shows multiple peaks in the spectrum, which was also reported in GaN UV optically pumped multi-mode lasing and explained by the strain in the InGaN layer.[32]

In conclusion, we have successfully demonstrated yellow stimulated emission from an optically pumped InGaN edge-emitting laser structure at room temperature. This result

demonstrates high crystal quality yellow InGaN/GaN MQWs and shows great promise towards the realization of electrically injected yellow InGaN laser diodes.

DATA AVAILABILITY

The data that support the findings of this study are available within the article.

Funding:

This work is funded by the Solid State Lighting and Energy Electronics Center, UCSB (100010947) U.S. Department of Energy (DE-AR0000671) and Defense Advanced Research Projects Agency (HR001120C0135) subcontract with Nexus Photonics.

References:

1. K. Iida, T. Kawashima, A. Miyazaki, H. Kasugai, S. Mishima, A. Honshio, Y. Miyake, M. Iwaya, S. Kamiyama, H. Amano, Jpn. J. Appl. Phys. 43 L499(2004).
2. J. I. Malin, J. R. Meyer, C. L. Felix, J. R. Lindle, L. Goldberg, C. A. Hoffman, and F. J. Bartoli, C. ‐ H. Lin, P. C. Chang, S. J. Murry, R. Q. Yang, and S. ‐ S. Pei, Appl. Phys. Lett. 68, 2976 (1996).
3. T. Kitatani, K. Nakahara, M. Kondow, K. Uomi and T. Tanaka. Jpn. J. Appl. Phys. 39, L86 (2000).
4. H. Hamada, R. Hiroyama, S. Honda, M. Shono, K. Yodoshi, T. Yamaguchi, IEEE J. Quantum Electron. 29, 1844 (1993).
5. O. Delorme, L. Cerutti, E. Luna, G. Narcy, A. Trampert, E. Tournié, and J.-B. Rodriguez, Appl. Phys. Lett. 110, 222106 (2017).
6. T. Hosoda, G. Kipshidze, G. Tsvid, L. Shterengas, G. Belenky, IEEE Photon. Technol. Lett. 22, 718(2010).
7. R. Schwertberger; D. Gold; J.P. Reithmaier; A. Forchel, IEEE Photon. Technol. Lett. 14, 735 (2002).
8. A. Tyagi, Y.-D. Lin, D. A. Cohen, M. Saito, K. Fujito, J. S. Speck, S. P. DenBaars and S. Nakamura, Appl. Phys. Express 1, 091103(2008).
9. M. T. Hardy, C. O. Holder, D. F. Feezell, S. Nakamura, J. S. Speck, D. A. Cohen, and

S. P. DenBaars, Appl. Phys. Lett. 103, 081103 (2013).

10. H. Zhang, H. Li, P. Li, J. Song, J.S. Speck, S. Nakamura S. P. DenBaars, ACS Photon. 7, 1662 (2020).
11. H. Li, P. Li, H. Zhang, J. Song, S. Nakamura S. P. DenBaars, ACS Appl. Electronic Materials 2, 1874 (2020).
12. H. Zhang, D.A. Cohen, P. Chan, M.S. Wong, S. Mehari, S. Nakamura S. P. DenBaars, Optics Lett. 44 3106 (2019).
13. Y. Mei, G. Weng, B. Zhang, J. Liu, W. Hofmann, L. Ying, J. Zhang, Z. Li, H. Yang, H. Kuo, Light Sci. Appl. 6, 16199 (2017).
14. A. Sahm, N. Werner, J. Hofmann, R. Bege, K. Paschke, IEEE Photon. Technol. Lett. 30, 1878 (2018).
15. Little, Christopher E. Metal vapour lasers: Physics, Engineering and Applications. 1999.
16. C. V. Shank and A. Dienes, A. M. Trozzolo, J. A. Myer, Appl. Phys. Lett. 16, 405 (1970).
17. K. Inagaki, K. Ohkoshi, S. Ohde, G. A. Deshpande, N. Ebihara, A. Murakami, Jpn. J. Ophthalmology 59, 21 (2015).
18. X. Huo, Y. Qi, Y. Zhang, B. Chen, Z. Bai, J. Ding, Y, Wang, Z. Lu, Optics and Lasers in Engineering 134, 106207 (2020).
19. T. Gasenzer, D.C. Roberts, K. Burnett, Phys. Rev. A 65, 021605 (2002).
20. S. Nakamura, M. Senoh1, N. Iwasa, S. Nagahama, T. Yamada, and T. Mukai, Jpn. J. Appl. Phys. 34, L1332 (1995).
21. J.-I. Hwang, R. Hashimoto, S. Saito and S. Nunoue, Appl. Phys. Express 7, 071003(2014).
22. A.I. Alhassan, R.M. Farrell, B. Saifaddin, A., Mughal, F. Wu, S.P. DenBaars, S. Nakamura, and J.S. Speck, Optics Express, 24, 17868 (2016).
23. P. Li, H. Li, H. Zhang, C. Lynsky, M. Iza, J. S. Speck, S. Nakamura, and S. P. DenBaars, Appl. Phys. Lett. 119, 081102 (2021).
24. P. Li, A. David, H. Li, H. Zhang, C. Lynsky, Y. Yang, M. Iza, J. S. Speck, S. Nakamura, and S. P. DenBaars, Appl. Phys. Lett. 119, 231101 (2021).
25. R. Anderson, D. Cohen, H. Zhang, E. Trageser, N. Palmquist, S. Nakamura, and S. P.

DenBaars, Optics Express 30, 2759 (2022).
26. S. Lutgen, A. Avramescu, T.Lermer, D. Queren, J. Müller, G. Bruederl, U. Strauss, Physica Status Solidi (a) 207, 1318(2010).
27. L. Toikkanen, A. Härkönen, J. Lyytikäinen, T. Leinonen, A. Laakso, A. Tukiainen, J. Viheriälä, M. Bister, and M. Guina, IEEE Photon. Technol. Lett. 26, 384 (2013).
28. G. Rossbach, J. Levrat, G. Jacopin, M. Shahmohammadi, J.-F. Carlin, J.-D. Ganière, R. Butté, B. Deveaud, and N. Grandjean, Phys. Rev. B 90, 201308(2014).
29. D.D. Koleske, A.J. Fischer, B.N. Bryant, P.G. Kotula, J.J. Wierer, J. Cryst. Growth, 415, 57(2015).
30. S. Ahmed Al Muyeed, W. Sun, M. R. Peart, R. M. Lentz, X. Wei, D. Borovac, R. Song, N. Tansu, and J.J. Wierer, J. Appl. Phys. 126, 213106 (2019).
31. A. David and M. J. Grundmann, Appl. Phys. Lett. 96, 103504 (2010).
32. M. Shan, Y. Zhang, T. B. Tran, J. Jiang, H. Long, Z. Zheng, A. Wang, W. Guo, J. Ye, C. Chen, J. Dai, and X. Li, ACS Photon. 6, 2387 (2019).

Appendix

Lateral µLED of different sizes - Process Flow

Process			Notes (for *c*-plane GaN)
Remove Indium	Acid Bench	3:1 HCl:HN03 Aqua Regia, 3 x 10min, mix new batch each iteration, wait 5min for boiling, 120oC on hotplate (color will change to orange-brown)	
ITO Deposition	Solvent Bench	3 min Ace, 2 min Iso, 1 min DI, N2 dry (sonicate on high)	
	Acid Bench	40s dilute HCl (1:1 HCl:water)	
	E-Beam #2	Load samples and silicon monitor onto clean carrier wafer. Heat to 680ºC (actual temperature is 290ºC). Deposit at 0.5• Å/s for ~110 nm.	For blue, deposit 110 nm. For green, deposit 220 nm.
	Ellipsometer	Check silicon monitor for thickness	
ITO Etch and Mesa 1 Etch Litho	Solvent bench	3 min Ace, 2 min Iso, 1 min DI, N2 dry (sonicate on high)	Mask 1: p-contact and Mesa 1 Mask dimensions: x: 5.25mm, y: 5.25mm If necessary, use SPR220-7.0, 3.5 krpm, 10 krpm/s, 45 sec Softbake at 115C for 2 min Expose for 1.35s, focus offset = -1 WAIT 40 MINUTES for sample to outgas Post-exposure bake at 50C for 1 min, 115 C for 90s Develop in 726MIF for 1'45" to 2" 2 min DI rinse flowing, N2 dry
	PR Bench	Dehydration bake, 2min 110C, let cool 1min	
		Spin SPR220-3.0, 3000 rpm, 10 krpm/s, 30 sec	
		Clean backside with EBR 100	
		Softbake, 110C 90 seconds	
	Stepper #2 (GCA Autostep 200)	Load mask #1 - "Lateral uLED Size Comparison - common contacts v5"	
		Load sample onto 2" 500 µm chuck with 130 µm shim	
		Run "EX ULEDV3" Pass: MESA1	
		Expose for 0.6s, Focus offset =0	
		Post-exposure bake at 110ºC for 60s	

	Develop Bench	Develop in 726MIF for 60 seconds	
		2min DI rinse flowing, N2 dry	
	Microscope	Inspect, develop more if necessary	
	UV Ozone	20min (~6A/min)	
ITO Etch	RIE#2	Vent, use an Iso soaked wipe to clean chamber walls, top plate and platen	No sample in the chamber (blue plasma)
		Pump down the chamber (DO NOT load samples)	M: Methane, H: Hydrogen, A: Argon (pink plasma)
		O2 clean - 30 min: 20 sccm O2, 125 mT, 500 V	Check water level (T=50-60º); Increase mannual pressure to 1.18 Fore line off (down) THEN turn rough on (do not have both on together ever); wait below 80 mtorr; rough off, foreline on, HVAC on. Turn on IG1 and wait until <3E-5
		MHA coat - 20 min: 4/20/10 sccm M/H/A, 75 mT, 500 V	
		Vent, load samples	
		MHA etch - 5 min: 4/20/10 sccm M/H/A, 75 mT, 350 V	The following is for etching 110 nm of ITO. MHA etch = 8 min (17 nm/min, 20% overetch), ~136 nm: 4/20/10 sccm M/H/A, 75 mT, 350V Sample in chamber, (~17.2 nm/min)
		O2 descum - 50sec, 20 sccm, 125 mTorr, 170 V	
		MHA etch - 3 min: 4/20/10 sccm M/H/A, 75 mT, 350 V	
		O2 in situ descum - 10 min: 20 sccm O2, 125 mT, 300 V	
	Dektak/Ellips.	Check silicon monitor to make sure ITO is completely etched	
Mesa 1 Etch	RIE#5	Load bare RIE wafer for chamber prep: yonkee01	O2 clean, BCl3 coat, SiCl4 prep
		Load samples on RIE wafer (no oil) for etch: yonkee02	SiCl4 etch, Etch rate = 30 nm/min (very repeatable)
		Dip samples in water immediately after etch	
		Soak sample in DI for 2min, N2 dry	
	FL µscope	Check that the emission in the field is a different color than emission in mesas (to ensure AR is etched)	
	Solvent Bench	Strip PR in NMP, 80C, 10+min, ultrasonicate before submerging sample	
		2min Iso, 3x 30s DI Dump&Rinse, N2 dry	
	HF Bench	*BHF dip for 1'?*	to remove GaN redep; both heated substrate and RT+anneal ebeam ITO are very resistant to BHF

	Dektak/SEM	Measure step height 1-2 points per sample	
ODR Litho	Solvent Bench	3min Ace, 3min Iso, 3x 30s DI Dump&Rinse, N2 dry	Do not pattern silicon monitor; maybe use the n-contact PR For positive resist: Spin LOL2000, 2krpm, 10krpm/s, 30s (~250 nm thick). Clean backside of sample with EBR100. Bake on hotplate at 210 C for 5 min, let cool for 2 min Spin 955CM-1.8, 3krpm, 10krpm/s, 30s (~1.8 μm thick) Clean backside of sample with EBR100 Edge Bead removal Softbake, 95C 90s, Expose 0.75s, -1 offset, Hardbake 110C 90s Develop in 726MIF 75s (~15 nm/s undercut after 45 s), water flush
	PR Bench	Dehydration Bake, 2min 110C, let cool 1min	
		Spin nLOF2020, 3krpm, 10krpm/s, 30s	
		Clean backside of sample with EBR100	
		Softbake, 110C 90s	
	Stepper #2 (GCA Autostep 200)	Load mask #2 - "Lateral uLED Size Comparison - common contacts v5"	
		Load sample onto 2" 500 μm chuck with 130 μm shim	
		Run "EX ULEDV3"	
		Pass: nLOF	
		Expose 0.5s, -6 offset	
	PR Bench	**Hardbake 110C 90s**	
	Develop Bench	Develop in 300MIF 60s, water flush	
	Microscope	Inspect (verify 0.3-0.5 μm undercut on LOL2000), develop more if necessary	
	UV Ozone	20min (~6A/min) (on VCSELs **and Si monitor**)	
	Dektak	Optional Inspection	
ODR Dep	IBD	Vent MiniLoader (loadlock)	Before depositing the dielectric stack on your sample, do a calibration run with a piece of silicon. You may either run "12_AM_Cal_3_layer" and do ellipsometry using Asad's model or run 3 individual recipes depositing Si, Ta, and Al separately on 3 pieces of silicon 12-Nakamura, password = nitrides
		Open door. Load sample and stage.	
		Pump down. Wait for a few minutes to get below 5E-6	
		Open "12_BY_7_layer" recipe	
		Process	
	PR Bench	Strip PR in NMP, 80C, 10+min, ultrasonicate before submerging sample then spray with pipette	
		2min Iso, 3x 30s DI Dump&Rinse, N2 dry	
Sidewall passivation	Solvent Bench	3min Ace, 3min Iso, 3x 30s DI Dump&Rinse, N2 dry	
	ALD	DEPOSIT 50nm SiO2	
Common contacts Litho	Solvent Bench	3min Ace, 3min Iso, 3x 30s DI Dump&Rinse, N2 dry	
	PR Bench	Dehydration Bake, 2min 110C, let cool 1min	

		Spin nLOF2020, 3krpm, 10krpm/s, 30s	
		Clean backside of sample with EBR100	
		Softbake, 110C 90s	
	Stepper #2 (GCA Autostep 200)	Load mask #3 - "Lateral uLED Size Comparison - common contacts v5"	
		Load sample onto 2" 500 µm chuck with 130 µm shim	
		Run "EX ULEDV3"	
		Pass: nLOF	
		Expose 0.5s, -6 offset	
	PR Bench	**Hardbake 110C 90s**	
	Develop Bench	Develop in 300MIF 60s, water flush	
	Microscope	Inspect, develop more if necessary	
	UV Ozone	20min (~6A/min)	
	Dektak	Optional Inspection	
n-contact Deposition	Acid bench	**40s concentrated HCl**	
	E-beam 4	Deposit 700 nm Al / 100 nm Ni / 700 nm Au	
n-contact Liftoff	Solvent Bench	Liftoff in 1165, 80C, 10+min, spray with pipette, use heated bath, **no ultrasonication**	**DO NOT ULTRASONICATE ON HIGH AFTER METAL DEPOSITION** If sonication is used, use the low setting with the minimum intensity and frequency
		2min Iso, 2min DI rinse flowing, N2 dry	
	Microscope	Inspect, liftoff more if necessary	
	Dektak	Optional Inspection	